System integration of a high pressure alkaline electrolyser

Master Thesis

by

B.A.T.M. Boons

to obtain the degree of Master of Science
at the Delft University of Technology,
to be defended publicly on Friday February 4, 2022 at 9:00 AM.

Student number:	4451023	
Project duration:	January 8 2021 – February 4, 2022	
Daily supervisor:	Ir. J. van Kranendonk,	Zero Emission Fuels B.V.
Thesis committee:	Prof. dr. ir. W. de Jong,	TU Delft, chair
	Prof. dr. ir. E. Goetheer,	TU Delft
	Prof. dr. ir. B.J. Boersma,	TU Delft
	Dr. ir. J.W. Haverkort,	TU Delft
	Dr. R. Delfos,	TU Delft

This thesis is confidential and cannot be made public until February 4, 2024.

TU Delft

Acknowledgements

This thesis marks the end of my years as a student here at TU Delft and I am happy to conclude the impressing ride it has been with the work I present. Prior to diving into the wonders of engineering and electrolysis, I would to thank all people which supported me during this project and all people around me that have brought me in this privileged position.

First and foremost, this research could not be done without the people of ZEF, who gave me the chance to take up this challenge and guided me in the process which has not been without struggles and setbacks. The first to thank is definitely Jan, who was not only a wizard on electronics, engineering and science, but also an inspiring figure who never lost pace and enthusiasm. It was very, very nice to work with you and I could not imagine beforehand that I would have learned this much in a single project. I would like to thank professor Wiebren de Jong for taking time to read my work and to provide me with valuable feedback as my supervisor during the project. Together with him, I would like to thank the other committee members for taking time to read my work and participating in my graduation committee.

I would like to thank Ulrich, Hessel and Mrigank in their continuous endeavours to take ZEF to the next level. You gave me the chance to work on this awesome project, in a close team in which we all get along which was the perfect environment to do this research, thanks a lot! And the latest ZEF-core team member deserves a special thank you: Paul. Paul joined the AEC team when I was more or less halfway my thesis project and the difference was immediately notable. Thanks for your valuable input, opinions and clever fixes once the system was down again, besides managing the AEC team with good spirit and humour.

Besides the ZEF-core team, I owe many thanks to colleagues at ZEF and as both the term 'Integration' and the project duration suggest: a lot of people to thank. My 'ZEF-parents': Bart Mulder and Tom Kleist, they raised me with kindness in the ZEF-family. They showed me the system, stack assembly and system operation. Discussing results of their experiments with the three of us was where I really got a feeling for the system. I see my work as the sequel to theirs: I referred to Bart Mulders and Tom Kleists work over 35 times and over 15 times respectively, which illustrates their importance to my research.
The system and therefore this thesis could not have been made without the continuous and valuable effort of many ZEF-interns. I want to specifically thank Shahrukh, Khaled, Sander, Sam, Samarth, King Kunal, Alex and Hans. All of them have had their specific projects and contributions and the finally acquired system is the result of the effort of these people in specific. Thank you a lot, I am blessed to have had you on my side.

Evidently, I would not have been able to persevere through my studies as pleasant as I did without my family and friends. First, I would like to thank my family members who are still physically present: mam, Liesbeth, Lidwien, Teresa, Charlotte and Luuk, I would not have been in this privileged position without you and I feel blessed to be born and raised in our family; thanks to Otte for making the cover page. To my friends, teammates, (former) roommates and my study mates: thanks a lot, I can look back on very pleasant years and that is because of you!

Now all the people that were essential to arrive at this grande finale have been thanked, it is time to dig into the actual project. Or as Moses once said: "Let's split some water."

B.A.T.M. Boons
Delft, January 2022

Abstract

To anticipate for future demand of sustainable liquid fuels, Zero Emission Fuels B.V. develops a solar powered micro plant which produces methanol from water and carbon dioxide captured from outside air. An intermediate step in this process is the electrolysis of water to create hydrogen which reacts with CO_2 to methanol. This study encompasses an integration of the pressurised alkaline electrolysis system, in which problems observed in previous generations of the electrolyser have been solved and functionalities have been added. In addition to that, electrolyte samples are taken after different periods of operation to investigate electrolyte deterioration over time.

A new Balance of Plant (BoP) has been designed, realised and tested. Eight new features to the system can be distinguished, two of which are included to add functionality: the degasser to decontaminate the CO_2-rich feed water and the pressure booster to replenish the consumed water at system pressure. The other features are integrated to enlarge the operational envelope, the determination of which was central to the experiments conducted in this research. Experiments are conducted to find and characterise the four limitations to the operational envelope: the relative valve opening duty (RVOD), flow stagnation, temperature control and crossover.

The RVOD experiments showed deviations from the modelled valve opening cycles, attributed to additional pressure drops, valve opening interference and smaller discharge volumes. Subsequently a corrected model is presented to improve valve cycle time predictions.

Flow stagnation was investigated at various current densities, pressures and temperatures using camera images and a characteristic temperature response to establish flow stagnation. The results showed a minimum volume flow rate decrease in comparison to the previous system, expressed in parameter X which decreased from 3.4 to $0.74\,\mathrm{A\,K\,bar^{-1}\,cm^{-2}}$. The minimum volume flow rate decrease is attributed to the larger number of cells and the increase of the height difference between the stack and buffer tanks.

In the temperature control experiments, steady state temperatures were monitored at different current densities, with and without cross-flow fan operation. This resulted in a temperature control map, in which the reachable temperatures for different current density are depicted. Furthermore, electrolyte mass flows are determined and pressure dependency of temperature control was investigated at low current densities, concluding that steady state temperatures are independent from pressures in the $10\,\mathrm{bar}$ to $50\,\mathrm{bar}$ regime.

Hydrogen crossover was tested by taking gas samples at different operating conditions and subsequent gas composition analysis in a gas chromatograph; oxygen crossover was determined by an oxygen sensor implemented downstream the hydrogen exhaust. All steady state crossovers values were found to be below the safety limits, concluding that crossover is not limiting in the acquired system on all possible operating points. Overnight diffusion crossover experiments showed that maintaining the system under pressure overnight, keeps crossover values below the safety limit.

In addition to the operational envelope, complementary general characteristics such as power consumption and efficiency are presented and compared to industry and literature. On top of that, unexpected findings, design deficits and other relevant phenomena are described to complete the perspective on system performance and behaviour of the electrolysis system.

Due to the electrolyte mist purged into the degasser and pressure booster, the electrolyte deterioration experiments are deemed inconclusive. Moreover, a demister is found to be an essential system feature to include in the next generation electrolyser, because both degasser and pressure booster were damaged by the electrolyte spill.

Contents

List of Figures

List of Tables

Nomenclature

AEC	Alkaline Electrolysis Cell
AWE	Alkaline Water Electrolysis
BoD	Basis of Design
BoP	Balance of Plant
CD	Current Density
CT	Capillary Tube
F	Faraday Constant
GC	Gas Chromatograph
GUI	Graphical User Interface
HER	Hydrogen Evolution Reaction
HHV	Higher Heating Value
ICP	Inductively Coupled Plasma
IPCC	Intergovernmental Panel on Climate Change
KOH	Potassium Hydroxide
LEL	Lower Explosion Limit
LHV	Lower Heating Value
LMTD	Log Mean Temperature Difference
LS	Level Sensor
LT	Life-Time
NBO	Normal-Based Operation
OER	Oxygen Evolution Reaction
OPEX	Operating Expenditures
PB	Pressure Booster
PCB	Printed Circuit Board
PET	Pressure Equalisation Tube
PFD	Process Flow Diagram
P&ID	Piping & Instrumentation Diagram
PGM	Platinum Group Metal
PID	Proportional Integral Derivative
PR	Production Rate
RMSE	Root Mean Square Error
RVOD	Relative Valve Opening Duty
STP	Standard Temperature and Pressure
UEL	Upper Explosion Limit
ZEF	Zero Emission Fuels B.V.

1 Introduction

1.1. Energy transition

During and after the 18th and 19th century, the industrial revolution brought great wealth and prosperity to modern civilisations. But the heritage is clear: modern societies are highly dependent on fossil fuels, which are deeply entrenched in current energy systems across the world [81]. As can be seen in Figure 1.1, the global energy consumption in 2019 consisted of 84.3% fossil fuels. Making the worlds energy supply susceptible to extinction and subjecting humanity to the consequences of global warming due to green house gas emissions. Global warming effects are already being observed, for example larger fluctuations in regional and seasonal weather or a higher frequency of extreme floods or extreme drought [64]. Combined with an ever increasing global energy demand [17], the urgency of a profound and fundamental energy transition is underlined even more. The United Nations' Intergovernmental Panel on Climate Change (IPCC) has identified the next 12 years as the critical period to begin to halve and subsequently reach zero carbon pollution to stay within $1.5\,^{\circ}\mathrm{C}$ warming and avoid unacceptable severe expense and loss of health and life [64].

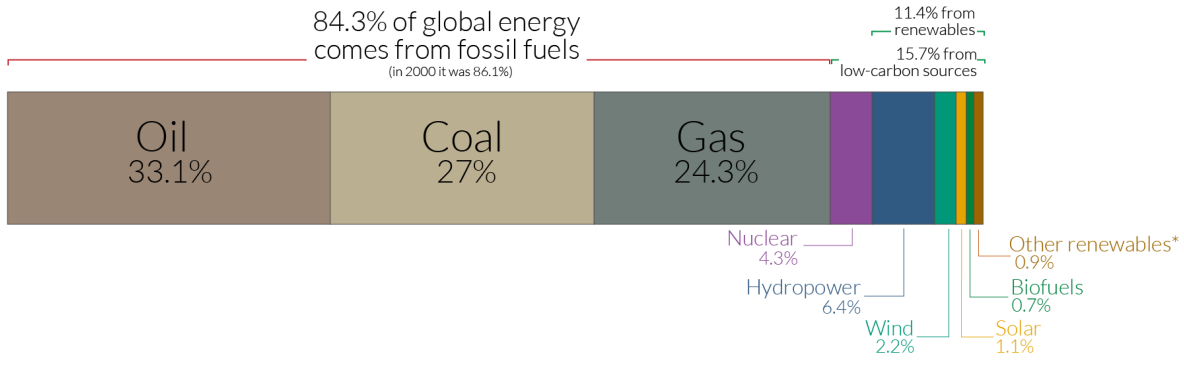

*'Other renewables' includes geothermal, biomass, wave and tidal. It does not include traditional biomass which can be a key energy source in lower income settings.

Figure 1.1: Global primary energy consumption by source in 2019 [63]

1.1.1. Hydrogen as future energy carrier

A fundamental property of renewable energy sources as wind mills and solar panels is their intermittent power output. Therefore, large scale implementation of intermittent renewable energy sources requires additional storage of (electrical) energy to accommodate varying energy demand in time [67]. To facilitate the energy storage, different proposed solutions are currently investigated. For example, hydrogen is considered a future energy carrier because oxidation of hydrogen removes CO_2 emissions from the equation and producing water as (the main) exhaust product. For that reason, hydrogen shows great potential as a non-polluting energy carrier.
Pareek et al. describe another important aspect of hydrogen as a crucial link in the energy transition

being the large variety of possible hydrogen production technologies: ”it is clearly seen from the figure that hydrogen can be utilized with respect to near term and long term goals not only from hydro/wind/solar/geothermal sources but also from biomass/concentrated solar power/microorganism/semiconductors” [58]. Making the large scale implementation of hydrogen into the energy distribution system less dependent on individual technologies and therefore lowering the risk of investments [87].
However, large scale implementation of hydrogen infrastructure in combination with renewable energy sources remains challenging, as hydrogen has impractical physical properties: it is the lightest element and is rather hard to liquefy (it has a critical temperature of $-240\,^{\circ}\mathrm{C}$). In addition to that, it has a relatively low volumetric energy density compared to conventional fossil fuels (*e.g.* liquid hydrogen has ≈ 3.5 times less energy per volume than gasoline). An important matter towards an actual sustainable energy system is besides the green house gas emission-free consumption of the fuel, but also its sustainable production. Hydrogen is already being produced as a raw material for synthesis of other chemicals rather than as a fuel and its production makes use of fossil fuels for the most part (natural gas reforming and oil based production of hydrogen take up to over two thirds of the global hydrogen production) [87, 58, 1]. As is exemplified in Figure 1.2, hydrogen production based on fossil fuels is significantly cheaper than based on renewable energy. Concluding that a sustainable implementation of hydrogen as a large scale future energy carrier remains a large challenge to this day.

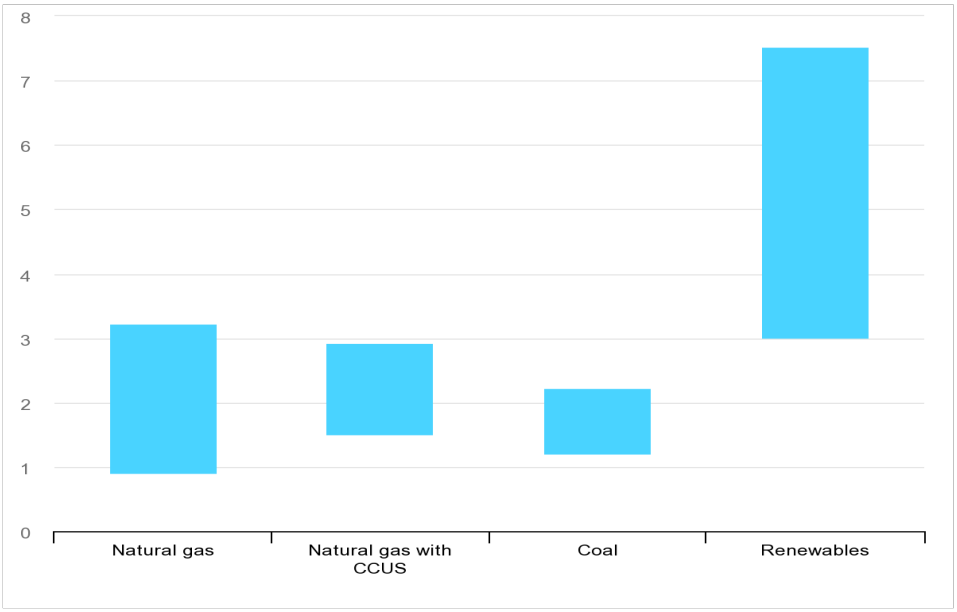

Figure 1.2: Hydrogen production costs by production source in $\$/\mathrm{kg}$ produced hydrogen, 2018 [31]. Image taken from technical report by the International Energy Agency,.
CCUS: Carbon Capture, Utilisation and Storage

1.1.2. Electrolysis as possible outcome

A possibility to produce hydrogen is through water electrolysis, which makes use of electricity to split pure water into its constituents: hydrogen and oxygen. The first official record of hydrogen production through electrolysis dates back to 1789, when Jan Rudolph Deiman and Adriaan Paets van Troostwijk used a ’Leyden jar’ to produce a small amount of hydrogen and oxygen (their original setup can still be seen at the place where they once did their famous experiment: Teylers Museum in Haarlem, the Netherlands) [72, 77]. Their experiment was followed up by the first electrolysis by a voltaic pile in 1800 by Nicholson and Carlisle, within weeks after Alessandro Volta had discovered the voltaic pile [57]. Although the history of electrolysis and related hydrogen technologies is rich and developed continuously throughout the 19th and 20th century, water electrolysis does not contribute significantly of today’s hydrogen production. The International Energy Agency reports in 2019: ”While less than 0.1% of global dedicated hydrogen production today comes from water electrolysis, with declining costs for renewable electricity, in particular from solar PV and wind, there is growing interest in electrolytic

hydrogen" [32]. Electrolysis could be a crucial link in the future energy infrastructure bridging between intermittent (electrical) renewable energy sources and a new non-polluting energy carrier in the form of hydrogen. Therefore development towards fully functioning, efficient electrolysis systems is highly relevant. This thesis is devoted to just that: to make a small step of improvement towards a complete electrolysis prototype system, which might turn out to become an important technology in a sustainable energy supply.

1.1.3. Zero Emission Fuels B.V.

Zero Emission Fuels B.V. (ZEF) is a start-up founded by three people: Jan van Kranendonk, Ulrich Starke and Hessel Jongebreur and their mission is to develop a stand-alone micro-plant that produces methanol with solar radiation as energy source. Since 2017, the team is based in TU Delft's 3Me faculty where it has access to a variety of lab facilities and frequently interacts with university experts. The team is complemented with a group of around fifteen students. Generally the students are from a different study backgrounds and/or institutions and are doing an internship or writing a thesis at ZEF.
The end product of ZEF's micro-plant is liquid methanol rather than hydrogen itself, because of the aforementioned impracticalities. Liquid fuels potentially combine a large volumetric energy density with current storage and distribution infrastructure compatibility [98]. Konig et al. report in 2015: "Another emerging area of interest is the use of renewable energy to produce liquid electro-fuels (E-fuels) that are compatible with the existing infrastructure, current storage approaches, and low-cost tanks to be used in applications that require high-density fuels, such as the aviation or marine sectors" [40]. ZEF anticipates this need of liquid fuels by appending the electrolysis system with both a methanol synthesis reactor and a direct air capture unit. A generalised version of the flowchart of ZEF's micro-plant can be seen in Figure 1.3. In the flowchart different building blocks can be distinguished, they correspond to function-specific subsystems. The subsystem structure is identical to the internal subdivision of ZEF's people into its teams:

- **Direct Air Capture (DAC)**, the subsystem responsible for the capture of CO_2 and water out of the atmosphere. It also contains a gas-liquid separator, such that two distinct product stream leave this subsystem.
- **Fluid Machinery (FM)**, which increases CO_2 pressure from atmospheric to $50\,\mathrm{bar}$.
- **Alkaline Electrolysis Cell (AEC)**, responsible for splitting the water into its constituents: hydrogen and oxygen. As the integration of this subsystem is the core of this thesis, a detailed system description can be found in section C.1.
- **Methanol Synthesis reactor (MS)**, the subsystem facilitating the reaction of CO_2 and hydrogen to methanol and water
- **Distillation column (DS)**, the subsystem responsible for the separation of methanol and water. The end product, pure methanol, is acquired and the water is circulated to the AEC.

The solar panel is powering all different subsystems; the only important component left in Figure 1.3 is depicted in green. Power supply is indicated with green arrows and actual fluid flow is indicated with black arrows. ZEF's current AEC setup is developed to a large extent and currently gas crossover and flow characteristics are being investigated in a functional prototype. The next step: system integration to obtain a fully functioning, stand-alone electrolysis system. ZEF's interest in a obtaining a fully functioning AEC system is evident, as it is one of the crucial building blocks of their micro-plant.
In the upcoming sections the research scope and questions clarify what integration of the AEC exactly encompasses and from what perspectives the system is assessed, but first the current status of ZEF's system is described and consultation of previous works bring the most prevalent problems forward.

1.1.4. ZEF's state of the art AEC system

An important first step in this study is to capture the relevant problems and recommendations based on the works made by ZEF predecessors. By consultation of their work, an accurate and up to date description of the current systems and its shortcomings is acquired. In this subsection, a conceptual introduction to the problems at hand is made, see Table 1.1. Both a detailed system description and problem descriptions can be found throughout chapter 2 and chapter 3.

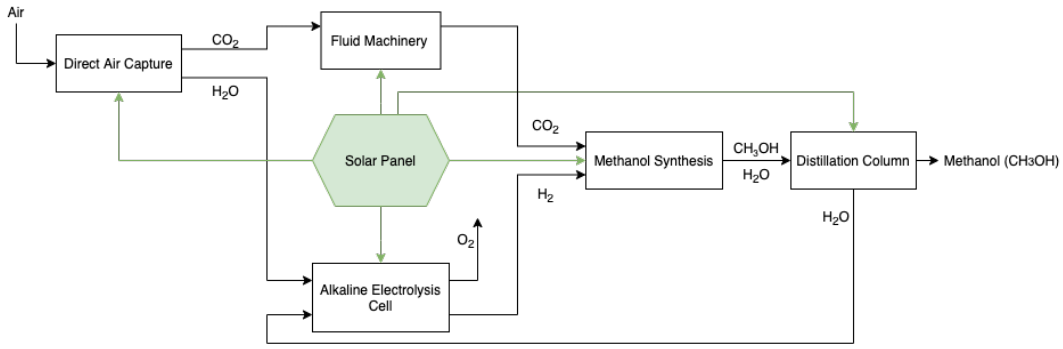

Figure 1.3: Flowchart of ZEF's micro-plant

Number	Problem	Category	Reference
1	DAC water supply not integrated	Dynamic Operation	
2	Absence of temperature control	Dynamic Operation & Safety	[39, 53]
3	Large pressure differences	Dynamic Operation & Lifetime	[18]
4	High crossovers	Safety	[53]
5	Unknown KOH degradation over time	Lifetime	

Table 1.1: First introduction to the problems at hand in ZEF's state of the art electrolysis system

Important to note is that the problems at hand are categorised in three different topics: Dynamic Operation, Safety and Lifetime. Although this subdivision is maintained throughout the rest of this thesis, problems possibly cover multiple dimensions; *e.g.* from the work of Mulder[53] it follows that in the current system crossovers are typically higher than industry standards (see section 2.4 for more details). This both affects the safety of the system and subsequently affects the dynamic operations (as operation is guided by safety limits).

1.2. Research Scope

System integration of ZEF's electrolysis system encompasses a variety of aspects. The ultimate goal of this thesis is to yield a fully functional and safely operating prototype of the AEC branch. Starting with contaminated (CO_2-rich) water from the DAC system up to the outlet, through which (high purity) hydrogen is fed into the methanol synthesis reactor at $50\,\mathrm{bar}$.
This thesis is devoted to description of and to deal with the role of interactions between subsystems with respect to dynamic operation, safety and life-time. The latter three describe the dimensions on which the final setup is assessed.

Within the consulted internship reports and master theses, various recommendations come forward to solve the problems presented in Table 1.1.
To start off with the problem indicated by number 1: the first step towards an integrated system is enabling the DAC-unit to supply contaminated water at atmospheric pressure. A degasser with a pressure booster is the proposed solution; the degasser decontaminates the CO_2-rich water and the pressure booster secures a water supply at stack pressure.
Consequently, the electrolyte degradation over time might form an issue regarding the life-time of the system, this problem is indicated by number 5. Therefore, the proposed approach is to evaluate the electrolyte solution on a large time scale (*e.g.* 10 days). Evidently, this is far from an accurate life-time estimation, but it is considered the first step towards understanding of the system's behaviour and performance over time.
Problem number 2, the absence of temperature control is currently limiting the maximum current density at which the system is operating [53]. The solution is to actively cool the electrolyte instead of passively only as is in the current system. Additionally, temperature control might open up new test possibilities as temperature is no longer a dependent variable but controllable to a certain extent.
The work of Daniil [18] pointed out that the current gas purging is rather violent, causing large pressure differences across the separator, indicated by problem number 3. Large pressure differences across the separator makes the level control unstable in particular situations [18] and impairs the mechanical integrity and the lifetime of the membrane. Possibly, pressure differences cause problem number 4 as is described in section 2.4. The proposed solution to both problems consists of capillary tubes and large diameter downcomers, such that gas purging occurs smoothly and oscillating fluid is kept to a minimum. As these parts are highly intertwined with size and placement of the buffer tanks and valve opening times, the latter two are reconsidered and redesigned. Both the open ends and the proposed solutions are extended throughout the rest of this thesis
The proposed solutions to the mentioned problems are summed up in Table 1.2. It gives the reader an idea to what the rather general objective of 'integration' boils down to. The solutions are only mentioned in a conceptual way, detailed design and analysis follow throughout the rest of this thesis. On

Number	Proposed Solution	Reference
1	Degasser & Pressure booster	[43, 20]
2	Active cooling	[39, 53]
3	Capillary tubes, large diameter downcomers, buffer tanks	[18, 53]
4	Capillary tubes, large diameter downcomers, buffer tanks and midplate-stack design	[18, 53]
5	KOH Quality testing	

Table 1.2: Proposed solutions to the problems stated in Table 1.1

the one hand, Important to note is that some solutions are proposed by former thesis students at ZEF and therefore give an accurate idea of what is needed to take the AEC system to the next development stage. On the other hand, the proposed solutions are based on those works, but do not guarantee a satisfactory functioning system once implemented. The proposed solutions are further analysed, elaborated, adjusted, designed and tested throughout this thesis.

1.2.1. Modus Operandi

Integration of different subsystems within the AEC system is expected to be an iterative process in which the current operative system is first analysed and problems are described (categorised to Dynamic Operation, Safety and/or Life-Time). Thereafter, the design is altered in correspondence with

the solution to the described problems and subsequently the proposed solution is implemented and tested. The last step is to assess the obtained system on the aforementioned three pillars: dynamic operation, safety and lifetime. The last step connects back to the first step and accordingly the process is repeated until on all three dimensions a satisfactory level of performance is reached. Assessment of a satisfactory level of performance is central to the experiments in this thesis, in which the limitations to safe operation are identified. The modus operandi is summarised below:

1. Analysis of the current AEC system, description of challenges/problems towards integration
2. Design of the new, complete AEC system
3. Implementation and testing of the new AEC system
4. Assessment of the new system on three dimensions: dynamic operation, safety and lifetime

All safe operating conditions of the finally obtained system are condensed into a complete operational envelope. The operational envelope depicts all identified safe operating points expressed in operating conditions: pressure, current density, temperature. The operational envelope is therefore an essential descriptive system characteristic, as it directly prescribes the limitations of usage of the electrolysis system.

1.3. Research Questions

The thesis addresses obstacles related towards an integrated AEC system. The final deliverable consists of the integrated system itself and its accompanying operational envelope. Additionally, electrolyte degradation over time is tested and degasser performance is evaluated.
In the process towards solving the open ends towards integration (see Table 1.1 or section C.2 for more details) and obtaining a fully functional system, the following research questions are answered:

”How does the safe operational envelope look in terms of pressure and current density of the AEC system with the proposed conceptual solutions implemented?”

Subdivision of this generic question into three aspects of the proposed solutions brings the following sub questions forward:

1. To what extent is the stack temperature controllable?
2. What is the effect of purging through capillary tubes?
3. What is the effect of long, large diameter downcomers on crossover and flow stagnation?
4. What is the effect of the midplate-stack design on crossover?

Additionally, a second research question covers the ambition to describe the electrolyte quality over time:

”What is the effect of degassing CO_2-rich feedwater on the quality of the KOH electrolyte?”

With these two main research questions and accompanying sub questions, the overall approach of this study is covered. Throughout the rest of the thesis, detailed designs and tests guide the process towards the final deliverables: a new, fully functional and integrated AEC system and its operational envelope. In addition to that, electrolyte degradation over time is tested.

2

Theoretical Background

In this chapter, phenomenological and theoretical aspects of alkaline water electrolysis are presented and discussed. Literature is consulted to present the reader a clear overview of relevant elements to consider designing a new electrolysis system. It serves as a theoretical framework through which system behaviour can be explained or at least be related to.
Starting on a fundamental level of electrolysis, essential aspects such as energetics and efficiency determination are discussed. Secondly, Related to the energetic and efficiency consideration is the system representation in an electrical analogue, through which the internal resistances of the system can be evaluated clearly. After the rather holistic approach, a detailed analysis on a molecular scale is presented in section 2.3, resulting in correlations which explain system behaviour on a large scale.

2.1. First principles of alkaline electrolysis

To start the theoretical background, the reaction in which pure water is split into its constituents (H_2 & O_2) is explained first. Once the fundamental aspects of electrolysis are explained in a nutshell, the process is evaluated from an energetic point of view. Different efficiency definitions are introduced at the end of this section, hopefully leaving the reader with a general overview of relevant aspects of electrolysis.

2.1.1. The reaction equations

Chemical reactions are often described by reaction equations, which bundle the entire conversion into one or multiple equations. Water electrolysis can be described by a single decomposition step, see Equation 2.1. However this representation is very simplified and the first distinction to make is between acidic and alkaline electrolysis. Acidic electrolysis makes use of protons as transporting particles and alkaline electrolysis makes use of OH^- (hydroxide) ions [70]. The two different methods are compared in section 2.2. In this section only alkaline electrolysis is considered, as this is the type of electrolysis applied in ZEF's electrolysis system.

$$2H_2O_{(aq)} \longrightarrow 2H_{2(g)} + O_{2(g)} \quad \textit{Water Electrolysis Reaction} \tag{2.1}$$

Alkaline electrolysis can be decomposed into three steps. First, at the negative cathode both hydrogen gas and consequently hydroxide ions (OH^-) are produced; the reaction equation of the *Hydrogen Evolution Reaction* (HER) is given in Equation 2.2. Subsequently, the negatively charged hydroxide ions travel through the separator diaphragm towards the positive anode at the oxygen side (driven by an electrostatic force). At the positive anode surface, four hydroxide ions react, forming two water molecules and one oxygen molecule. The reaction equation of the *Oxygen Evolution Reaction* (OER) is given in Equation 2.3.

$$2H_2O_{(aq)} + 2e^- \longrightarrow H_{2(g)} + 2OH^-_{(aq)} \quad \textit{Cathode Reaction, } H_2 \textit{ production} \tag{2.2}$$

$$4OH^-_{(aq)} \longrightarrow 2H_2O_{(aq)} + O_{2(g)} + 4e^- \quad \textit{Anode Reaction, } O_2 \textit{ production} \tag{2.3}$$

The two equations are still a simplified version of underlying complex reaction kinetics, further details and explanation are presented in section 2.3.

2.1.2. Energy

The energy required for water electrolysis can be determined through thermodynamics. A clear way of reporting reaction energies are through the change in Gibbs free energy and the reaction enthalpy. The minimum amount of electrical energy required is the change in Gibbs free energy, denoted as ΔG [62]. Additionally, a certain amount of thermal energy is required, as a consequence of an increasing entropy throughout the reaction (2 mole of liquid water is used and 3 mole of gas is formed).The thermal term can be denoted as $T\Delta S$, with temperature T and entropy change ΔS. Adding the Gibbs free energy to the thermal term delivers the reaction enthalpy, denoted as ΔH. This gives the total energy that is consumed in the reaction, either electrically or thermally and corresponds to the enthalpy of formation of one mole of water. The two terms are related through Equation 2.4:

$$\Delta H = \Delta G + T\Delta S \quad \text{Reaction Enthalpy, } [\mathrm{kJ\,mol^{-1}}] \tag{2.4}$$

As mentioned, the energy is supplied in the form of electricity. A convenient step is to express the required energies as voltages, because voltages are directly measured in the system and therefore assessment of system performance can easily be done. In the next subsection efficiencies are introduced and presented as a voltage fraction. In Equation 2.5 this conversion can be seen, F denotes Faraday's constant ($96\,485\,\mathrm{C\,mol^{-1}}$) and 2 is the number of electrons exchanged. The change in Gibbs free energy ΔG is $237\,\mathrm{kJ\,mol^{-1}}$ at standard temperature and pressure (STP). A positive change in Gibbs free energy indicates a non-spontaneous process [30], so the U_{Rev} is $-1.23\,\mathrm{V}$ [13, 99]. This voltage is known as equilibrium voltage, reversible cell voltage, or open circuit potential.

$$U_{Rev} = -\frac{\Delta G}{2 \cdot F} \quad \text{Equilibrium cell voltage, [V]} \tag{2.5}$$

U_{Rev} is the minimum voltage at which the electrolysis reaction occurs. If the additionally required heat is supplied electrically, the required voltage increases. This voltage is known as the thermoneutral voltage and is based on the reaction enthalpy ΔH as can be seen in Equation 2.6.

$$U_{Th} = -\frac{\Delta H}{2 \cdot F} \quad \text{Thermoneutral voltage, [V]} \tag{2.6}$$

At STP, the enthalpy of formation ΔH is $286\,\mathrm{kJ\,mol^{-1}}$ resulting in a thermoneutral potential of $-1.48\,\mathrm{V}$[13]. At this specific voltage, the required electrical energy and additional heat is supplied precisely.

These two voltages often play a role in the determination of process efficiency, however an important notion is in place. Both the equilibrium cell voltage and the thermoneutral voltage are dependent on the state of the fluid. As can be seen in Figure 2.1, both voltages vary with temperature. The equilibrium cell voltage is more dependent on temperature in comparison to the thermoneutral voltage. The thermal contribution $T\Delta S$ in Equation 2.4 increases with temperature, combined with a decreasing ΔG, leaving the ΔH, and therefore the thermoneutral voltage less dependent on temperature [45].

Influence of pressure

Lamy et al. [45] present an elaborate consideration on thermodynamics in electrolysis and different assumptions lead to different equations describing the influence of pressure on equilibrium voltage. The thermoneutral voltage, based on the enthalpy of reaction, is expected to be approximately constant with varying pressure: "The enthalpy change (ΔH) is constant because the effect of pressure on the free-energy and the entropy changes cancel out each other" [45]. The Gibbs free energy change however, varies with pressure. A simplified version of the Nernst equation, assuming an ideal gas, sheds light on the effect of pressure on the equilibrium voltage, see Equation 2.7 [45].

$$U_{Rev}(T,p) = \frac{\Delta G^0(T)}{2F} + \frac{RT}{2F} \ln \frac{(p_{H_2})(p_{O_2})^{\frac{1}{2}}}{p_{H_2O}} \quad \text{Simplified Nernst equation} \tag{2.7}$$

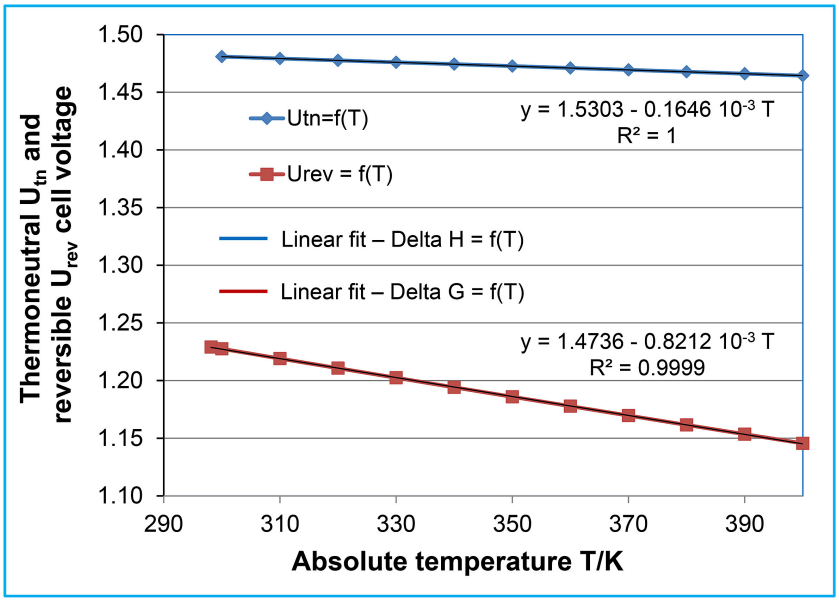

Figure 2.1: Equilibrium & Thermoneutral voltages for different voltages
Image taken from the work of Lamy et al. [45]

Where p_{H_2}, p_{O_2}, and p_{H_2O} denote the partial pressures of hydrogen, oxygen, and water respectively. R denotes the universal gas constant ($R = 8.314\,\mathrm{J\,mol^{-1}\,K^{-1}}$) and $\Delta G^0(T)$ denotes the change in Gibbs free energy at a certain temperature at standard pressure (basically corresponding to the ΔG in Equation 2.4). So generally, an increase in pressure leads to an increase of equilibrium voltage (if pressure throughout the cell is assumed to be constant)

To conclude this subsection, a brief overview of the three different voltage regimes are summed up below. U is referring to the actual applied voltage:

1. $U < U_{Rev}$, the minimum required electrical energy is not supplied. Consequently the reaction does not take place.

2. $U_{Rev} < U < U_{Th}$, the minimum electrical energy is supplied, therefore the reaction takes place. However the required heat is not supplied electrically and consequently subtracted externally.

3. $U > U_{Th}$ Both the required electrical energy and additional heat is supplied by the power source. The voltage surplus causes heat generation.

2.1.3. Efficiency

Another important process parameter is efficiency, the consideration on energy being made. Often, efficiency is one of the key aspects in evaluating overall system performance [38], therefore precise definitions of efficiency forms a vital aspect in performance assessment and report of an electrolysis system. Lamy et al., state that efficiency is defined as the required energy under reversible conditions divided over the real situation, where irreversibilities occur [45]. An electrolysis system, like other systems, has irreversibilities and other losses. The losses result in a higher applied voltage than from a theoretical point of view is strictly necessary and the applied voltage can therefore be used to infer system efficiency. Details on different origins of losses can be found in section 2.3. In this section, focus is on different definitions of efficiency and their physical background.
In literature, particular efficiency definitions are used to compare systems. The Faradaic efficiency is based solely on the electrical energy demand. As can be seen in Equation 2.8, the change in Gibbs free energy is used as the energy demand under reversible conditions [13, 62, 45]. The two expressions on the right are obtained through converting the change in Gibbs free energy (also called 'free energy change' [62]) to cell voltages.

$$\eta_{Faradaic} = \frac{\Delta G}{\Delta G + Losses} = \frac{U_{Rev}}{U} = \frac{1.23\,\mathrm{V}}{U} \tag{2.8}$$

An important aspect of the Faradaic efficiency is that it does not take into account the thermal energy required for the reaction. An alternative approach to define efficiency can be found in Equation 2.9. This definition takes the total required energy (electrical and thermal) into account. If the heat required is supplied through an overvoltage, the expression in the middle and on the right can be used to infer the systems thermal efficiency [13, 62, 45]. Note that if the heat is supplied externally and the system operates at a voltage between $1.23\,\mathrm{V}$ and $1.48\,\mathrm{V}$, the thermal efficiency based on voltage exceeds 100%. This is a consequence of a violation of the assumption on which the thermal efficiency is based: the total energy demand is supplied electrically and both losses and heat requirements are reflected in the applied voltage U.

$$\eta_{Thermal} = \frac{\Delta H}{\Delta H + Losses} = \frac{U_{Th}}{U} = \frac{1.48\,\mathrm{V}}{U} \tag{2.9}$$

In addition to the rather theoretical efficiencies presented so far, industry often determines efficiency in a more general way [45]. Although authors tend to capture the entire system in one efficiency coefficient for comparison to other systems, Lamy et al. report that 'industry efficiencies' are ambiguous too. For example, different temperature and pressure conditions lead to different calculated energy contents of the products or LHV (Lower Heating Value) is used while others use the HHV (Higher Heating Value)[45]. In industry, efficiency is not always directly expressed as a percentage, but sometimes the specific energy consumption is used, expressed in $\mathrm{kW\,h\,kg^{-1}}$ or $\mathrm{kWh/Nm^3}$ for example[45]. A specific example of a commonly used efficiency used in industry can be seen in Equation 2.10. In this expression the HHV of hydrogen combustion in oxygen (so it is the opposite of the enthalpy of formation of water $285.8\,\mathrm{kJ\,mol^{-1}}$) times the molar production rate ($\dot{n}_{H_2}$ in $\mathrm{mol\,s^{-1}}$) represent the energy content of the product gas produced every second. The denominator represent the combination of three powers: electric, thermal, and auxiliary equipment and together form the input power.

$$\eta_{Industry} = \frac{HHV \cdot \dot{n}_{H_2}}{P_{electrical} + P_{thermal} + P_{auxiliary}} \tag{2.10}$$

Concluding that from every efficiency perspective presented, two different characteristics determine the systems efficiency. Firstly, thermodynamic aspects such as temperature and pressure which alter the reaction kinetics. Secondly, internal losses, energy that is dissipated and effectively not contributing the electrolysis reaction, ohmic heating for example. Throughout the rest of this thesis, different efficiency definitions are used and relate to the aforementioned efficiencies.

In the next section, all fundamental components in an alkaline electrolyser and their respective backgrounds in scientific literature are presented. After all essential components are introduced, electrical resistances in the system are explained, giving the reader a more detailed picture of what are the most relevant parameters in electrolysis.

2.2. Fundamental components

Now with the first principles of electrolysis and the overall process being introduced, focusing on the fundamental necessities for electrolysis, certain components in electrolysis come forward, which are schematically depicted in Figure 2.2. Literature consultation provides the scientific context of the fundamental components implemented in ZEF's electrolysis system. Auxiliary equipment is described in chapter 3, completing the current state of ZEF's electrolysis system.

2.2.1. Electrolyte

The liquid electrolyte facilitates anion transfer and consequently requires a high ionic conductance. In order to enhance the conductivity of the solution, electrolytes which generally consist of ions with high mobility are applied in the electrolyser [99]. Potassium hydroxide is most commonly used in water

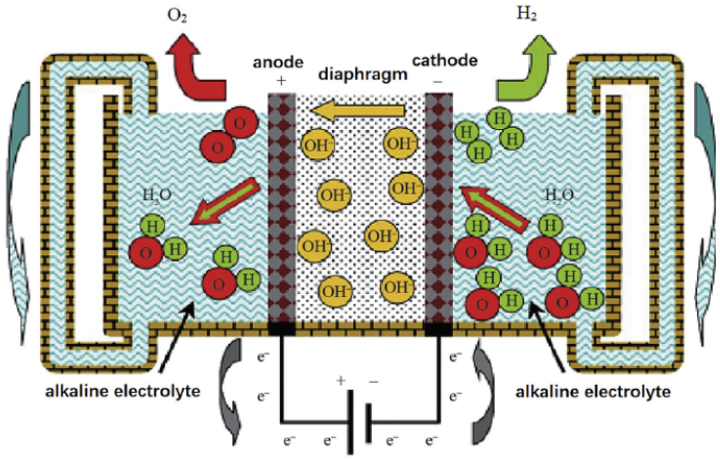

Figure 2.2: Schematic overview of alkaline water electrolysis[97]

electrolysis, avoiding the huge corrosion loss caused by acid electrolytes and the use of precious metals such as platinum group metals (PGM's) [47]. ZEF's electrolyte solution consists of water with $30\,\mathrm{wt\%}$ potassium hydroxide (KOH), $25\,\mathrm{wt\%}$ to $30\,\mathrm{wt\%}$ is considered an optimum value in industry (typically at temperatures in the range of $50\,^{\circ}\mathrm{C}$ to $80\,^{\circ}\mathrm{C}$) [99, 24, 14]. In recent work by Ju et al. in 2018 [38], also a $30\,\mathrm{wt\%}$ is used. Throughout the rest of this thesis, the electrolyte composition at the start of operation is assumed.

2.2.2. Separator Diaphragm

The separator functions as a semi-permeable barrier, it separates the oxygen and hydrogen sides such that no explosive gas-mixtures form and high purity hydrogen is guaranteed. On the other hand, the separator ought to enable charge-carrying hydroxide ions to travel from the cathode to the anode side. This property can be achieved through various routes and thus different production methods are developed so far, which are roughly divided into three different categories: diaphragms, anion exchange membranes (AEMs) and ion-solvating membranes, as illustrated in Figure 2.3 [41]

The most recent development in separation technology in electrolysis technology is the ion-solvating

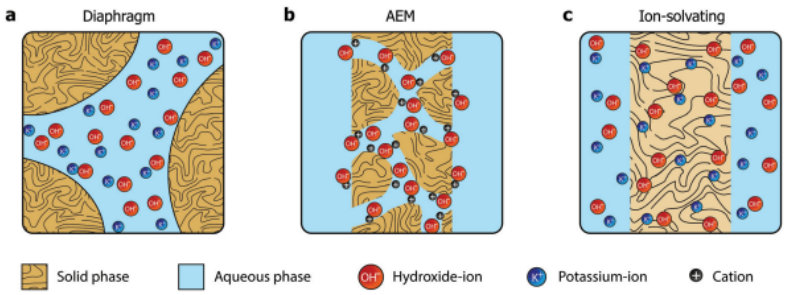

Figure 2.3: Three membrane types currently investigated for alkaline electrochemical applications: a) porous diaphragm, b) anion exchange membrane c) ion-solvating membrane.
Original image can be found in the work of Kraglund et al. [41]

membrane. Kraglund et al. describe the working mechanism of this novel type as follows: "Ion-solvating membranes are polymeric membranes, which when imbibed with KOH swell and form a homogeneous ternary electrolyte system of polymer/water/KOH. Ion-solvating membranes utilize the uptake and presence of an aqueous alkaline electrolyte to achieve ionic conductivity, and are not necessarily intrinsic hydroxide conductors, but unlike diaphragms they are dense (non-porous) and can be prepared as thin as other polymeric membranes" [41]. This is illustrated in the right-most image in Figure 2.3.

Alam et al. performed a numerical analysis to compare an m-PBI membrane (polybenzimidazole, an example of an ion-solvating membrane) and the conventional Zirfon diaphragm. The novel membrane technology showed potential: "Superior cell performance was achieved with the m-PBI membrane and

detailed overpotential analysis clearly indicated that the ohmic overpotential was significantly reduced by using them-PBI membrane" [4]. This finding is in accordance with the work of Kraglund et al. in 2019, which is displayed in Figure 2.4. The authors suggest the combined effect of the smaller thickness and

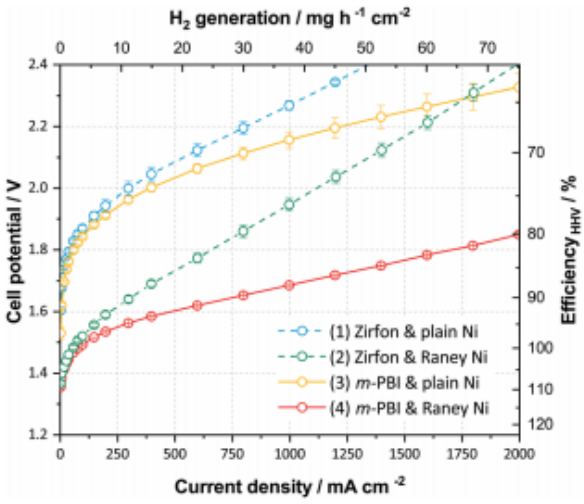

Figure 2.4: Comparison between Zirfon and an ion-solvating m-PBI membrane with a $25\,\mathrm{wt\%}\ KOH$ solution at $80\,^{\circ}\mathrm{C}$,[41]

its higher ionic conductivity caused the observed increase in cell performance using m-PBI membranes compared to usage of Zirfon membranes. Hydrogen and oxygen impurities (due to crossover) were deemed sufficiently low [4]. Further investigation and subsequent optimisation of this technique might lead to ion-solvating membranes outperforming porous diaphragms [14] (*e.g.* due to lack of PGMs such as iridium [41]). Yet, exploration and long term testing of degradation modes of ion-solvating membranes such as m-PBI is required to provide sufficient scientific base for a cell design in which long term stability is acquired [42].

Anion exchange membranes (AEMs) are considered a promising alternative to the conventional porous diaphragms as it has potential to be much thinner [13]. AEM electrolysis cells involve a separator membrane that facilitates the hydroxide ion transfer via couplings with positively charged groups (in literature labelled "Cationic side groups" [41]). Membrane hydration is essential to proper functioning of an AEM, as it provides the mobility of the anions in the electrolyte solution [88].
Research on AEMs is rapidly evolving in recent years and with it the membranes' properties. Hickner et al. report that large steps have bee taken towards a more complete understanding of the involved phenomena and lifetime issues have been improved drastically in recent years [41]. But the most prevalent challenge that still remains is it's chemical and mechanical stability. Zhegur et al. present a detailed analysis of chemical degradation of an AEM in terms of its most important properties: ion exchange capacity, water uptake and conductivity [101]. The experiments showed a significant degradation of the ion exchange capacity over time (the order of magnitude of days). In conclusion, AEM electrolysis are not commercially available yet and to obtain a long lifetime application, further investigations are considered necessary [14, 101, 29, 88].

Porous diaphragms are commonly used in alkaline electrolysis today [14]. Before the 1970's asbestos was commonly used as porous diaphragm in electrochemical processes, because it has low ohmic losses [99]. However, asbestos lacked proper corrosion resistance at elevated temperature in alkaline media. Moreover, its carcinogenic property was discovered and asbestos was gradually replaced by other diaphragms [99]. In particular, the aforementioned Zirfon diaphragm is currently widely used and often used as reference to newly developed separators in literature. The Zirfon Perl UTP 500 is a commercially available product and used in ZEF's electrolysis system. Although the Zirfon Perl UTP 500 is already applied in industry, new and more advanced pre-commercial versions are currently being developed [14], for example Zirfon Eco and Zirfon thin. The technical specifications of the used diaphragm are reported in Table 2.1.

Parameter	Value	Standard Deviation	Unit	Reference
Thickness	500	50	µm	Technical Data Sheet Zirfon [2]
Poresize	150	15	µm	Brauns et al. [14]
Poristy	55	10	%	Technical Data Sheet Zirfon [2]
Density	2.02	0.2	$\mathrm{g\,cm^{-3}}$	Technical Data Sheet Zirfon [2]
Maximum Temperature	110		°C	Technical Data Sheet Zirfon [2]

Table 2.1: Zirfon Perl UTP 500

2.2.3. Electrodes

The electrodes are directly involved in the electrochemical conversion reactions (HER and OER) and require specific properties. Evidently, a maximal catalytic activity is desired for both the HER and OER whilst resisting a very corrosive environment [16]. A clear advantage of alkaline electrolysis over acidic electrolysis, sucha s Proton Exchange Membrane (PEM) electrolysis, comes forward in the catalyst on the electrode surface. In contrast to electrolysis in an acidic environment, precious metals are generally not required and therefore alkaline electrolysis has a commercial edge. Ju et al. state: ” Alkaline water electrolysis is a proven and cost-effective technique, which has been commercialized at large scale” [38].

Nickel is a popular electrode material due to its high activity and availability as well as low cost [36, 38]. However, Ju et al. report that a true comparison of different electrodes is somewhat contestable: ”In general, reported activities in the literature are often difficult to compare as they are tremendously affected by the challenging surface area estimation of electrocatalysts” [38]. Concluding that both the material selection itself and its morphology ought to be considered when describing and evaluating electrodes. Despite pure nickel is reported as a stable catalyst for both HER and OER, its performance is often found to be rather poor [68]. Raney nickel is nickel which has been treated in a particular way, which has been developed through extensive research over the years. Raney nickel is conventionally made by dissolving nickel in molten aluminium, followed by the addition of zinc or chromium whilst quenching [21]. The dissolved components leave the nickel with a large internal surface area, which is in turn resulting in a large number of possible reaction sites. Raney nickel is widely used in alkaline water electrolysis systems today, as it is considered a cost-effective, well-performing electrode material [79]. Although investigated in particular for the HER [82], Raney nickel is known to perform well at the anodic OER too [11].

ZEF’s electrodes in the zero-gap design are coated with Raney nickel, produced by Permascand. In

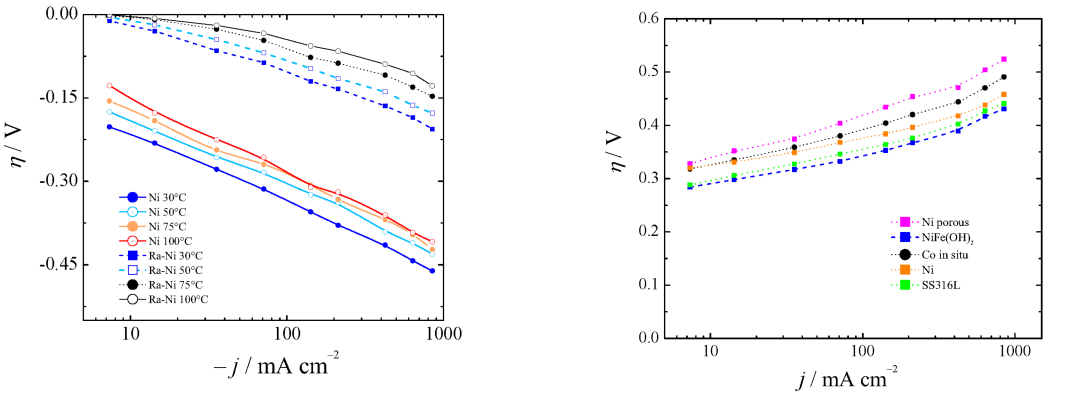

(a) Polarisation curve for different electrode materials for HER, (aged) nickel versus Raney nickel

(b) Polarisation curve for different electrode materials for OER

Figure 2.5: Comparison of different electrode materials for HER (a) and OER (a), overpotential plotted against current density Original graph can be found in the work of Colli et al.[16]

ZEF’s non-zero gap design however, the electrodes and bipolar plates are integrated into a single $3\,\mathrm{mm}$ thick nickel plate (and current collectors are unnecessary). An important notion is in place: the nickel plates are not treated nor coated with Raney nickel and simply consist of 98% nickel. Performance and suitability in ZEF’s electrolysis system have yet to be proven. An intensive study has been done by

Colli et al. on different electrode materials, including pure nickel and Raney nickel. The work revealed similar differences between nickel and Raney nickel as the aforementioned work by Schalenbach et al. [68]. The influence of pretreatment of the nickel was emphasised in the work of Colli et al. : "It was noteworthy that Ni required an aging/activation process of some $12\,\mathrm{h}$ in concentrated KOH (6 M) before performing at its best." This pretreatment is referred to aging. As can be seen in Figure 2.5a, Raney nickel outperforms the pure (aged) nickel for HER. However, Figure 2.5b shows an opposite effect for the OER, where the overpotential for the porous nickel (such as Raney Nickel) is actually larger than for pure nickel.

2.3. Reaction Kinetics

With general system characteristics and the fundamental components being introduced, the next step is to dive into detail: reaction kinetics. In the upcoming section, relevant phenomena are discussed to come to a detailed understanding of influences on the applied potential. A thorough understanding of potential constituents is considered essential as it explains system behaviour and it could guide future system development. In the upcoming sections, the potential constituents are described and explained.

Overpotentials

Different elements of the system each introduce their unique resistances. Different underlying phenomena result in different overpotential characteristics. First, different contributions to the total applied potential are introduced, leading to the actual total cell voltage. Thereafter, each relevant contribution to the total voltage is further detailed.

The total cell voltage and its constituents can be seen in Equation 2.11. In which U_{Rev} denotes the reversible cell voltage, $\eta_{cathode}$ and η_{anode} denote the overpotentials at the cathode and anode respectively. The last term $I \cdot R_{cell}$ denotes the Ohmic cell resistance. The equation is obtained from the work of Phillips et al. [59], but similar equations can be found in many different studies [94, 99, 13]

$$U_{Cell} = U_{Rev} + \eta_{cathode} + \eta_{anode} + I \cdot R_{cell} \quad \text{Total cell potential} \tag{2.11}$$

Before discussion the different parts of Equation 2.11, an a priori comparison of what terms dominate others in terms of magnitude can be seen in Figure 2.6. An immediate notion can be made: some contributions do not vary with current density (*e.g.* the equilibrium voltage) while other significantly vary with current density (*e.g.* ohmic losses) [59]. The equilibrium voltage U_{Rev} is defined in subsection 2.1.2 and therefore not explained in the upcoming subsections.

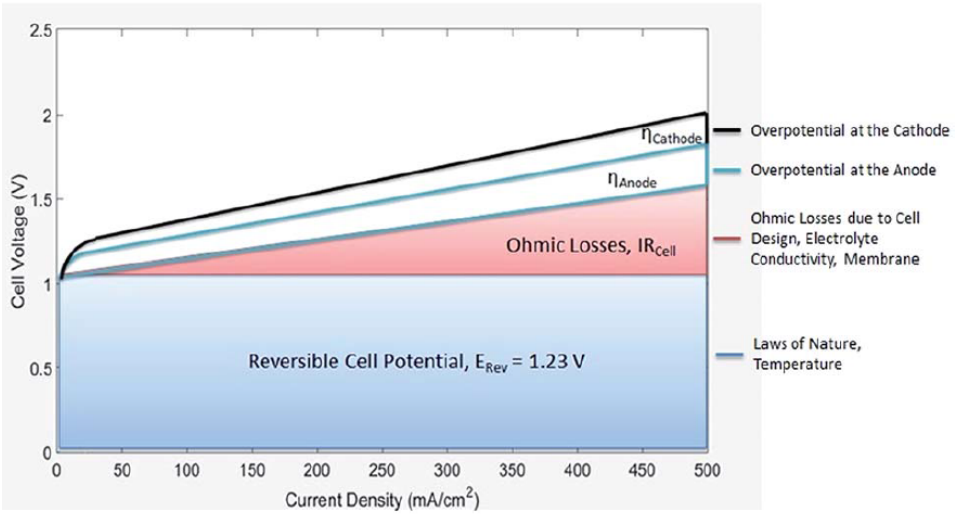

Figure 2.6: Different contributions to the total cell potential at different current densities
Image taken from the work of Phillips et al. [59]

2.3.1. Electrode kinetics

The first kinetics to consider are the reaction kinetics at the electrodes, for this is where the decomposition reaction itself takes place. Zeng et al. [99] clearly state what the ultimate goal of electrode kinetics is: "The study of electrode kinetics seeks to establish the macroscopic relationship between the current density and the surface overpotential." As the current density is actually a measure of the production rate, such a relationship is important as it maps overpotentials (an input parameter) to production rates (an output parameter) at the electrodes. This particular type of overpotentials is often referred to as *activation potentials*. In Equation 2.11 activation potentials are denoted by $\eta_{cathode}$ and η_{anode}, referring to the activation overpotentials at the cathode and anode side respectively.
In many studies, the equations describing the relationship between overpotential and current density at the electrocatalytic surface are the Butler-Volmer and/or Tafel equations [99, 76, 27].

Butler-Volmer equation

A well-known method to relate the current density (and thus the reaction rate indirectly) to the applied voltage is through the Butler-Volmer equation.
A detailed derivation of the Butler-Volmer equation can be found in the work of Bard and Faulkner (chapter 3) [9]. In their derivation, important assumptions have been made: a so-called 'one-step, one-electron process' approach is used, meaning that in their derivation, one electron is involved in the rate determining reaction step. Another important assumption is that the reaction rate constant can be determined by use of the Arrhenius equation which can be seen in Equation 2.12 [99].

$$k = De^{-\frac{E_a}{RT}} \quad \text{Arrhenius equation} \tag{2.12}$$

In which D denotes the frequency factor describing the molecular collision frequency [1]. R the universal gas constant and T the temperature. The most important quantity for the rest of this analysis is the *activation energy* denoted by E_a, because the activation energy is influenced by the applied potential [76, 99], this can be seen graphically in Figure 2.7.
Figure 2.7 shows the standard free energy (G) as function of a so-called *reaction coordinate*, which

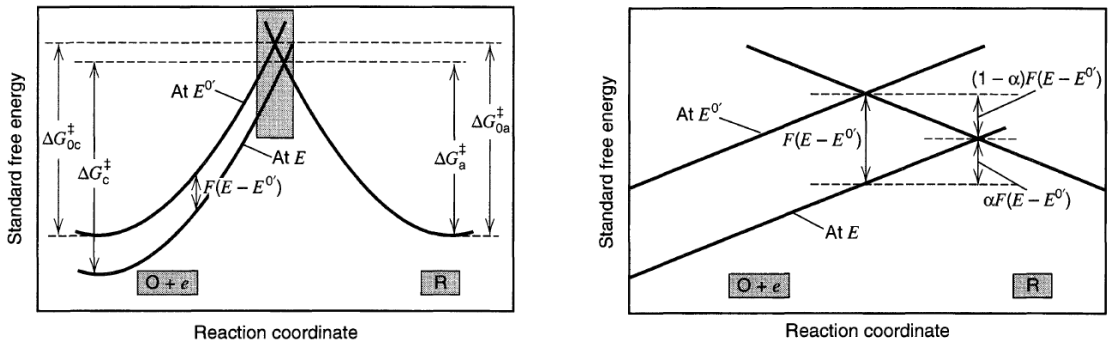

(a) Activation energies as function of the reaction coordinate

(b) Close up of the shaded area in the image on the left

Figure 2.7: The influence of a potential change on the activation energy in an electrochemical reaction
Original graphs can be found in the work of Bard and Faulkner [9]

expresses progress of the reaction[2]. If the activation energy is provided, intersection of the cathodic and anodic free energy lines is reached and reaction occurs. The required activation energies are indicated in Figure 2.7a (ΔG_c denoting the cathodic and ΔG_a the anodic activation energy) and the influence of a potential change can be inferred graphically.
Zooming in on the intersections in Figure 2.7b and following the derivation of Bard and Faulkner, two additional parameters are introduced: F and α.

[1] Although the frequency of collisions and therefore the frequency factor is temperature dependent, the temperature dependence is significantly less in comparison to to the $e^{-\frac{E_a}{RT}}$ term [9]

[2] Bark and Faulkner [9] about the use of reaction coordinates: "In general, the reaction coordinate expresses progress along a favoured path on the multidimensional surface describing potential energy as a function of all independent position coordinates in the system."

F is a proportionality constant which maps potential change to change in standard free energy of a specific eletrocatalytic surface. α is a *transfer coefficient*, which is a measure of symmetry between the anodic and cathodic free energy change due to the potential change and varies between 0 and 1 [9, 99]. In Figure 2.7b, α can be interpreted graphically as an outcome of the particular slopes of the anodic and cathodic free energy lines. Introducing three more calibration constants ($C_O(0,t)$, $C_R(0,t)$ and k^0) which are dependent on the reference point [3], finally ending up with the Butler-Volmer equation:

$$cfi = FAk^0 \cdot [\, C_O(0,t)e^{-\alpha f(U-U^0)} - C_R(0,t)e^{(1-\alpha)f(U-U^0)}] \quad \text{Butler-Volmer equation} \tag{2.13}$$

With $f = \frac{F}{RT}$ and $(U - U^0)$ being the potential change relative to the equilibrium potential. Both the assumptions and the equation being introduced, the next step is to make a simplification of the Butler-Volmer equation which can be utilised to compare electrodes in a relatively simple fashion using two parameters and the well known Tafel plots. To do so, an initial simplification is made: assuming no mass transfer limitations (*e.g.* if current density is considerably low) the Butler-Volmer equation as presented in Equation 2.13 can be simplified to what is historically known as the Butler-Volmer equation:

$$i = i_0 \cdot [\, e^{-\alpha f\eta} - e(1-\alpha)f\eta] \quad \text{Simplified Butler-Volmer equation} \tag{2.14}$$

The aforementioned term $U - U_0$ is replaced by η, which is known as the *overpotential*. i_0 denotes the *exchange current*, which is equivalent to the aforementioned k^0, describing the reaction rate at equilibrium conditions[4], thus at $\eta = 0$.

Tafel Equation & Plot

Starting from Equation 2.14 and having introduced the concepts of exchange current i_0 and overpotential η, one small addition can be made to derive another well-known formula: the Tafel equation. By carefully examining the two exponential terms in Equation 2.14 it can be observed that at either large positive or at large negative overpotentials, one of the two terms dominates the other[5] [76].
At large negative overpotential for example: $e^{-\alpha\eta} >> e^{(1-\alpha)\eta}$. So if a large negative overpotential is assumed and the remaining term is solved for the overpotential, the Tafel equation emerges:

$$\eta = a + b \cdot \ln i \quad \text{Tafel equation} \tag{2.15}$$

With $a = \frac{RT}{\alpha F}\ln i_0$ and $b = -\frac{RT}{\alpha F}$. The two parameters characterise the electrocatalytic performance of the electrode surface for a specific reaction and are therefore often used to (quickly) compare different electrodes [94, 99, 76]. b is known as the Tafel slope and determines the additional required overpotential if current density is increased by a certain amount. a depends directly on the exchange current density and defines the starting point of what is called a Tafel plot. A general example of a Tafel plot is depicted in Figure 2.8. Note that the current density is plotted on a logarithmic scale at the y-axis and the linear equation of Equation 2.15 indeed holds for large overpotentials. The two different branches indicate the anodic on the left and the cathodic reaction on the right.

Tafel plots and accompanying Tafel equations are often made experimentally and used to compare different electrodes [94, 76]. Figure 2.4 and 2.5 describe performance of different electrode materials and separators respectively, but are in fact experimental variants of the just theoretically derived methods.

Applying the conventional Butler-Volmer and/or Tafel equations can not be done without caution. Shinagawa et al.[76] state: ”Although the Tafel analysis is useful in elucidating the rate-determining steps,

[3] The reference point is often chosen to be at equilibrium conditions [76, 9]. In this particular case, this can be confirmed by comparing the activation energy on the cathode (ΔG_{0c}) and anode side (ΔG_{0a}) in Figure 2.7a at equilibrium potential indicated by E_0. The two activation energies are indeed equal. For example, k^0 indicates the reaction rate constant at equilibrium conditions. Although no net current can be measured, reactions take place back and forth

[4] Note that i_0 is expressed as a current, but as has been stated: at equilibrium conditions, there is no *net* current. i_0 only describes the magnitude of the cathodic and anodic reaction, which are both equal in magnitude

[5] Zengt et al. [99] specify a large overpotential as $118\,\mathrm{mV}$ at $25\,^{\circ}\mathrm{C}$

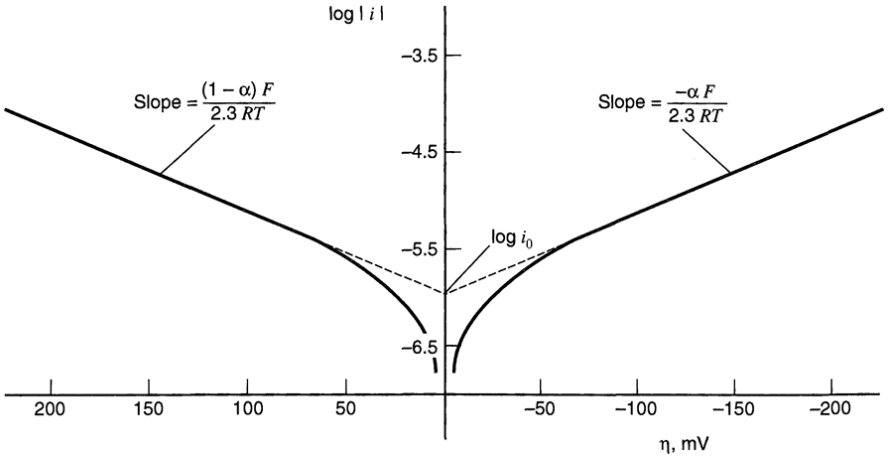

Figure 2.8: A general example of a Tafel plot, overpotential η plotted against the logarithm of the current density i Original graph can be found in the work of Bard and Faulkner [9]

too simplified discussion, such as determination of the kinetics based only on the Butler-Volmer assumption, fails to accurately describe the surface electrocatalysis." The authors emphasise the Buttler-Volmer equation apply strictly to electron transfer kinetics and to cases where the reaction rate is determined by electron transfer, which holds in specific cases only.

Rate determining step
As the aforementioned analysis is based on assuming a specific rate determining step. This suggests that the reactions actually consist of a sequence of multiple steps instead of in one single step. Literature indeed suggests that the reactions as presented in Equation 2.2 and Equation 2.3 do not tell the complete story of how hydrogen and oxygen are formed in alkaline electrolysis.
Additional clarification on the different reaction steps and on what a rate determining step encompasses is given in the upcoming paragraph.
The HER (Hydrogen Evolution Reaction) is taken as an example to show that a more complex sequence of reactions underlies the simpler aforementioned equations. In reality, three different steps can be distinguished:

$$H_2O + e^- + M \rightleftharpoons MH + OH^- \qquad \text{Volmer Step} \qquad (2.16)$$

$$2MH+ \rightleftharpoons 2M + H_2 \qquad \text{Tafel Step} \qquad (2.17)$$

$$MH + H_2O + e^- \rightleftharpoons M + H_2 + OH^- \qquad \text{Heyrovsky Step} \qquad (2.18)$$

M denotes the electrocatalyst on the electrode surface involved in the reaction. First of all, the three equations underline the importance of the electrode surface and material, as the parameter M has a prominent role in all three steps.
The point of providing the three steps is to show that the HER is actually a sequential process. The slowest of the three is characterised by the term *rate determining step*, as it sets the reaction rate for the overall HER.

Bard and Faulkner [9] state: "a widely held concept in electrochemistry is that truly elementary electron-transfer reactions always involve the exchange of one electron, so that an overall process involving a change of n electrons must involve n distinct electron transfer steps." This is highly relevant for the presented derivation of the Butler-Volmer and Tafel equations, as the aforementioned widely held concept confirms the 'one-step, one-electron' assumption. Nevertheless, another important assumption is done in the Butler-Volmer derivation: the rate-determining step is an electron-transfer process. Evidently, each step has its own reaction rate, all differently dependent on bubble coverage of the electrode, ionic activity and reaction specific kinetic rate constants [76]. Because of the different dependencies, the

rate-determining step is situation specific and one general approach (*e.g.* through Butler-Volmer) is not applicable in all cases.
The OER (Oxygen Evolution Reaction) can be subdivided into five different steps, but the previous reasoning holds. Different underlying reaction steps implicate not one generally applicable method to describe current density as function of overpotential.

2.3.2. Electrolyte kinetics

The electrolyte, as mentioned before, is an aqueous solution of 30 wt% potassium hydroxide (KOH). Considering losses and the accompanying overpotentials, three relevant aspects are discussed.

Electrolyte conductivity

Considering the electrolyte as a component in the electrical circuit, it does not have an infinite conductivity and therefore introduces a new resistance in the system. The overpotential as a consequence of the electrolyte resistivity, or often referred to as Ohmic losses, is stated by Philips et al. [59] as follows:

$$IR_{electrolyte} = \frac{i \cdot l}{\kappa} \tag{2.19}$$

With κ being the conductivity in Siemens per centimetre and dependent on electrolyte concentration and temperature. A typical value for κ at 30 wt% KOH at $80\,^{\circ}\mathrm{C}$ is $138\,\mathrm{S\,cm^{-1}}$ [28, 27]. i is the current density ($\mathrm{A\,cm^{-2}}$). l is the spacing between the diaphragm and electrode (mm), of which the order of magnitude highly depends on cell configuration (for a zero-gap design: $< 0.5\,\mathrm{mm}$[59]). The latter motivated electrochemist to develop a *zero-gap design* in which the overpotential due to electrolyte resistivity is minimised by minimising l[59].

Electrode bubble coverage

An important source of overpotential is due to the coverage of the electrode by evolving gas bubbles. The evolving gas bubbles prevent the liquid from making contact with the active catalyst on the electrodes, effectively reducing the active reaction surface and therefore increasing the applied current density [91]. The measured current density, ofted referred to as 'nominal' or 'superficial', can be used to express the actual applied current density as follows:

$$j = \frac{i}{1-\theta} \tag{2.20}$$

In which i denotes the nominal current density, j the actual current density and θ the fraction of the electrode surface covered by bubbles. The distinction between the two current densities increases with bubble coverage as is clearly depicted in Figure 2.9a.
Vogt et al.[91] state three parameters which influence the bubble coverage of an electrode:

- The rate of gas evolution at the electrode
- The average residence time of bubbles at the electrode surface
- The average bubble volume at departure from the electrode surface

The three different phenomena are interrelated and depending on the current density, temperature, pressure and materials, different phenomena are dominant. Many (semi-) experimental correlation functions and their respective applicable coverage regimes can be found in references [59, 54, 91, 92]. Experimental investigations and curve fits of such functions are shown in Figure 2.9b.

Bubble dispersion

Besides bubble coverage of the electrode surface, bubble dispersion affects the reaction kinetics as well. The term bubble dispersion refers to detached bubbles that simply 'occupy' electrolyte volume, effectively reducing the electrolyte volume through which the ion transfer takes place. This is illustrated generally (*i.e.* cell configuration is not relevant in this example) in Figure 2.10. The volume that is occupied by gas relative to the liquid medium is often described as the *void fraction*. The average void fraction is highly dependent on pressure (high pressure induce small bubbles), cell geometry, current

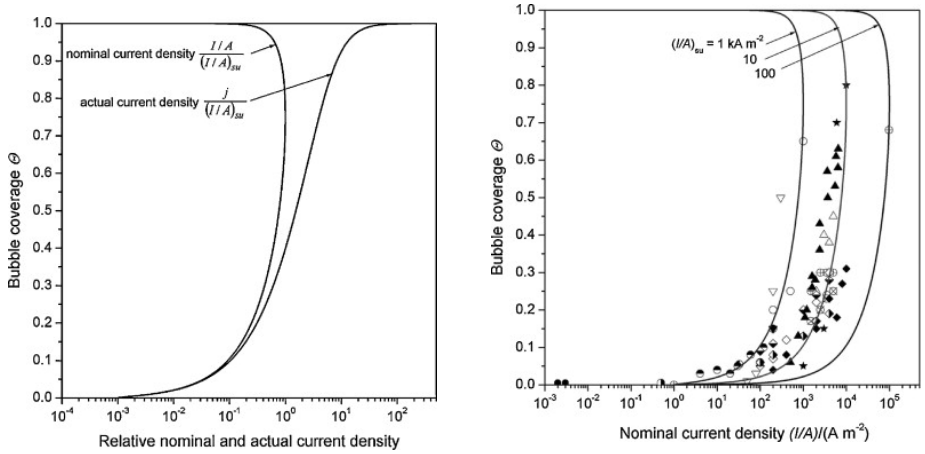

(a) Nominal and actual current density plotted against bubble coverage

(b) Nominal current density plotted against bubble coverage, experimental results complemented with a curve fit

Figure 2.9: Bubble coverage influencing nominal current density (right) and divergence between nominal and actual current density (left)
Original graphs can be found in the work of Vogt [91]

density, fluid properties and other properties. The figure shows that the local void fraction may vary within the cell.

The void fraction directly corresponds to the electrolyte resistance, described by the Bruggeman equation for spherical bubbles [94, 27]:

$$\frac{R_e}{R_{e0}} = (1-\epsilon)^{-\frac{3}{2}} \tag{2.21}$$

In which ϵ directly relates to void fraction θ: $\epsilon = \frac{2}{3}\theta$ [35]. Nagai et al. showed that especially at high current densities and small electrode spacing, the void fraction becomes large and causes a significant increase in cell resistance [54]. Since the void fraction directly corresponds to the gas production which in turn corresponds to the current density, the overpotential induced by the void fraction increases with increasing current density.

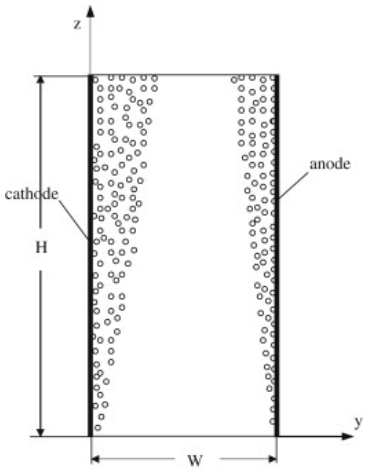

Figure 2.10: Detached bubbles form a layer occupying a certain volume, expressed as the void fraction
Image take from the work of Aldas et al. [5]

2.3.3. Diaphragm kinetics

According to Phillips et al.[60], the diaphragm causes a constant overvoltage, simply because its area and thickness are constant throughout the process. However, in the work of Jang et al. [35], a temper-

ature dependent resistance of a Zirfon diaphragm[6] is presented, assuming 30 wt% KOH solution:

$$R_{sep} = \frac{0.06 + 80e^{-T/50}}{10000 S_m} \tag{2.22}$$

In which T denotes temperature (in Kelvin) and S_m denotes the membrane surface area (cm^2). An experimental route was chosen by Vermeiren et al. [90]: the authors concluded that a 6 M KOH solution (which approximately corresponds to a 30 wt% KOH solution) at $30\,^{\circ}\mathrm{C}$ has an ionic resistivity of $0.2\,\Omega\,\mathrm{cm}^{-2}$. They simply measured the electrical cell resistance with and without presence of a separator. Detailed architecture of the membrane is less relevant to discuss from an electrical resistance perspective. In the section about crossover, a more detailed analysis of the membrane is included

2.4. Crossover

An important phenomenon in alkaline electrolysis is the contamination of the product gasses. Ideally, hydrogen and oxygen are acquired with 100% purity, but in reality some contamination of oxygen on the hydrogen side and vice versa is observed [37]. This phenomenon is known as *gas crossover*. Gas crossover, or shortly crossover, is affected by a variety of facets. Both operating parameters, such as temperature and pressure, and cell geometry, electrolyte concentration and auxiliary (BoP) equipment affect purity of the final acquired gasses [13]. Currently, mathematical descriptions of gas purities in water electrolysis have an empirical basis because of the many influencing parameters [26, 25]. From a safety perspective, determining purity (and therefore gas crossover) is paramount. A too high content of oxygen in the hydrogen tank (or vice versa) possibly forms an explosive mixture. The explosion limits describe the maximum allowed crossover and are expressed as percentages of hydrogen. Therefore, the Lower Explosion Limit LEL denotes the minimum percentage of hydrogen in an oxygen rich environment [7] and with that the maximum allowed hydrogen content in the oxygen tank. The Upper Explosion Limit (UEL) denotes a maximum hydrogen content to have an explosive mixture. Therefore, the UEL denotes to maximum allowable percentage of oxygen in the hydrogen tank. Explosion limits are sometimes expressed as volume percentages, but more often as a molar percentage. An important notion is that the explosion limits are highly dependent on temperature and pressure, as is depicted in Figure 2.11.

The most important LEL and UEL, regarding ZEF's system, are depicted in Figure 2.2. In the thesis

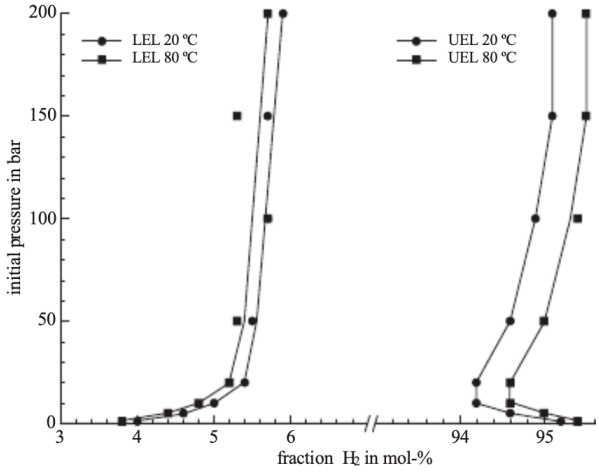

Figure 2.11: Pressure and temperature dependency of the LEL and UEL
Image take from the work of Janssen et al.[37]

Temperature [°C]	20	20	80	80
Pressure [bar]	1	50	1	50
LEL [mol-% H_2]	4.0	5.5	3.8	5.3
UEL [mol-% H_2]	95.2	94.6	95.4	95.0

Table 2.2: Particular explosion limits (LEL & UEL) at different temperatures and pressures [73].

study of Mulder, a ZEF coworker, these values were used to assess the systems safety. Both in the work of Mulder, in scientific literature and in industry, a typical safety measure is to operate the system

[6] ZEF uses a Zirfon UTP 500 diaphragm, detailed consideration of different separators can be found in chapter 3
[7] Schröder et al.[73] state that the LEL for hydrogen air mixtures are nearly identical to hydrogen oxygen mixtures, because in both cases an oxygen surplus is present

only below 50% of the LEL/UEL [13, 86]. For example, at $1\,\mathrm{bar}$ and $20\,^{\circ}\mathrm{C}$ the lower explosion limit is 4.0 mol-%, so whenever the gas measurement on the oxygen side reaches 2.0 mol-% hydrogen, the system is switched off (and possibly other safety measures come in to effect). In case of the upper explosion limit at $1\,\mathrm{bar}$ and $20\,^{\circ}\mathrm{C}$, the 50% safety measure boils down to switching of the electrolyser whenever the oxygen content is reaching 2.4 % on the hydrogen side.

Despite the dependency on a large variety of system aspects, particular crossover mechanisms can be distinguished and are explained in more detail. Insight into crossover mechanisms could facilitate guidance in improving the system with respect to crossovers. According to Trinke et al. [86] two main crossover categories can be distinguished: mass diffusion & mass convection through the separator, besides the crossover through the pressure equalising tube.

2.4.1. Mass Diffusion

If the electrolyser is in operation, different gasses start to develop on anode and cathode side. Besides in gas bubbles, oxygen and hydrogen molecules are dissolved into the liquid electrolyte too. Consequently, a concentration difference develops across the separator which in turn induces diffusive crossover. Diffusive mass transport is best described by the famous Fick's law [70, 86], of which a simplified version (assumption: steady state) can be seen in Equation 2.23. Following the analysis of Trinke et al., an important additional assumption (based on the work of Haug et al. [26]) is that no diffusion occurs through the solid phase of the separator. Additionally, gas bubbles are typically too large to fit through the pores and therefore only dissolved particles diffuse through the membrane.

$$N_{H_2}^{diff} = D_{H_2}^{eff} \frac{\Delta c_{H_2}}{\delta_{sep}} \tag{2.23}$$

In which $D_{H_2}^{eff}$ denotes the effective diffusion coefficient, δ_{sep} the membrane thickness and Δc_{H_2} denotes the hydrogen concentration difference between the two sides of the separator (for which often the concentration at the cathode side taken, as the hydrogen concentration on the anode side is considered negligible [86, 70]). The effective diffusion coefficient is a function of porosity η, tortuosity τ and a more general diffusion coefficient D_{H_2} which is a diffusion coefficient of hydrogen through the electrolyte media in absence of a separator. The effective diffusion coefficient can be found using Equation 2.24

$$D_{H_2}^{eff} = D_{H_2} \frac{\eta}{\tau} \tag{2.24}$$

In ZEF's electrolysis system, a Zirfon (Perl UTP 500) membrane is used, which has a $500\,\mu\mathrm{m}$ thickness and a porosity of approximately 50% [25, 2]. Given these parameters, an experimental study (in which for a given porosity of 50% a ratio between the effective and the second, more general type of diffusion coefficient is found ($D_{H_2}^{eff}/D_{H_2}$=0.159)) by Schalenbach et al. [69] is used to derive the tortuosity of 3.14. Given a certain super saturation or hydrogen concentration a the cathode side, the diffusive crossover can be estimated. Oxygen diffusing to the cathode side is governed by Fick's law as well, but different diffusion parameters are used.

2.4.2. Mass Convection

Mass convection is the second important characteristic crossover mechanism. In diffusive mass transfer, the driving force for hydrogen to move to the anode side or oxygen to move to the oxygen side, is a concentration difference. The convective part of the crossovers originate differently. Generally, two different mass convection mechanisms are distinguished: a pressure difference across the separator and electro-osmotic drag

Pressure Difference

A pressure difference between the anode and cathode side could induce liquid electrolyte to flow from the high pressure to the low pressure side through the separator. This induces a particular crossover, simply because of the dissolved species in that liquid electrolyte.
The famous Law of Darcy can be used to estimate the volume flow through the separator[86]:

$$Q = \Delta p \cdot K_{sep} \cdot \frac{A}{\mu \delta_{sep}} \tag{2.25}$$

In which A denotes the separators cross-sectional area, μ the dynamic viscosity, δ_{sep} the separator thickness and Δp the pressure difference across the separator. K_{sep} is the permeability of the separator and is a function of the diameter of the pores, the porosity and the tortuosity (follwing the Hagen-Poiseuille or Kozeny-Carman relations [86, 69].

Electro-Osmotic Drag
An additional type of mass convection crossover originates from the hydroxide ions moving through the separator and dragging liquid solvent with them. Again dissolved species in the solvent introduce an extra crossover term. The contribution of electro-osmotic drag to the total crossover is not explicitly determined in literature [86, 34, 27]. The magnitude and impact of electro-osmotic drag is highly situation specific and can differ locally [34]. Trink et al. [86] report their estimations of electro-osmotic drag to be negligible in comparison to other crossover mechanisms. However, the authors state that it might have significant impact at high current densities and high system pressures.

Electrolyte Mixing
In many studies, the electrolyte coming from the hydrogen and oxygen flash tanks are mixed into a single electrolyte recirculated back to the stack [38, 37, 26, 25]. Trinke et al. report that it is responsible for around 90% of the crossovers. Haug et al. [26] reports that mixing the electrolyte streams is the largest contribution to crossover: several different system configurations are tested on their product gas purity and the authors show that crossover can be decreased by a factor of 9 when separating the two electrolyte flows (depending on current density), this can be seen in Figure 2.12a. The explanation for this strong influence is simply due to the fact that electrolyte flows have a large amount of dissolved species in it. If the electrolyte flows are mixed, a lot of dissolved hydrogen ends up at the oxygen side after recirculation and vice versa.
Figure 2.12b shows that the current density has no significant impact on the molar crossover flux,

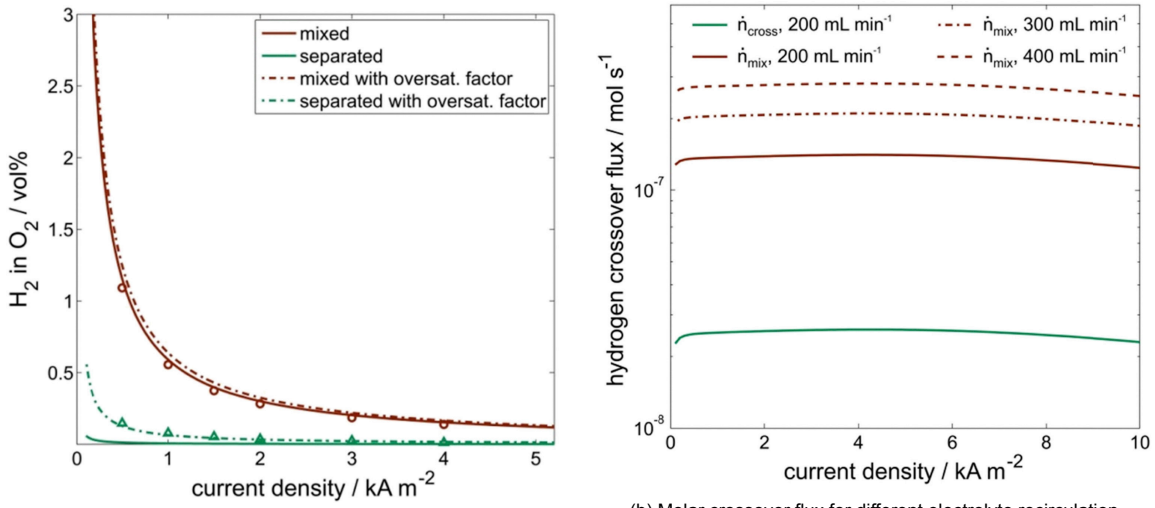

(a) The influence of the current density and the influence of electrolyte recirculation configurations (mixed or separated electrolyte streams)

(b) Molar crossover flux for different electrolyte recirculation configurations (mixed or separated electrolyte streams) and for different electrolyte circulation rates

Figure 2.12: Hydrogen contamination on the oxygen side as a function of current density, as vol-% (left) and as molar flow (right)
Graphs are taken from the work of Haug et al. [26]

indicated by the nearly flat curves. Furthermore, the graphs show a clear preference for separate electrolyte recirculation as both the absolute molar crossover and therefore also the relative crossover decrease dramatically when switching to separated electrolyte recirculation.

2.4.3. Influential Parameters

Having introduced different crossover phenomena, an important addition is to infer the influence of different parameters on crossover. As described above, both crossovers due to diffusion and convection

consist of dissolved species travelling to the opposite side of the separator. Consequently, the level of dissolved species determines the crossover flux. In the upcoming paragraphs, influences of different operating parameters on the level of dissolved species are explained.

Current Density
Current density is directly related to the production volume and is often used in expressing different electrolyser characteristics. According to Figure 2.12b, the current density does not impact the molar flow to the opposite side of the separator. Therefore it does not influence the crossovers in absolute sense, but does however impact the relative crossovers. As the molar flow remains constant for every current density, the total volume of product gas increases with current density and therefore the constant amount of molar crossover is a smaller percentage of the product gas at high current densities [26]. This phenomenon generally dominates over the influence of other parameters [14].

Pressure
The influence of system pressure can be understood by considering Henry's law Equation 2.26. With Henry's Law, the hydrogen concentration can be calculated as a function of: $p_{H_2}^{cat}$, hydrogen's partial pressure in the cathode compartment and S_{H_2}, the solubility of hydrogen.

$$c_{H_2} = S_{H_2} \cdot p_{H_2}^{cat} \tag{2.26}$$

This indicates that increasing system pressure, increases the amount of dissolved hydrogen and therefore an increase in hydrogen crossover is expected [13].

Temperature
The influence of temperature on crossover is a rather interesting phenomenon, as two competing effects take place. First of all, an increase in temperature decreases the electrolyte's solubility and therefore crossover would be likely to decrease likewise. But at the same time, an increase in temperature is associated with an increase in diffusion coefficient which enhances crossover [38] [8]. The experiments that lead to the graph in Figure 2.13 indicate that the decreasing solubility due to a temperature increase outweighs the increase of the diffusion coefficient in the case of a mixed electrolyte cycle. Furthermore, the differences seems to vanish at high current densities[25]. In Figure 2.14, a mixed electrolyte cycle is compared to separated electrolyte cycles, in which crossover is generally significantly lower. Figure 2.14 suggests that considering separated cycles the balance between the two competing effects tips over and diffusion appears to be dominant in a separated cycle and therefore crossover increases with increasing temperatures. Whereas the dissolution of gas outweighs the increase of diffusion at higher temperatures in case of a mixed electrolyte cycle [25]. Given this distinction, a crossover-temperature characteristic can be used to determine to what extent the obtained system can be considered to have separated electrolyte cycles or a mixed electrolyte cycle.

Electrolyte Concentration
The electrolyte concentration primarily affects the concentration of dissolved species. Electrolyte solubility is directly dependent on electrolyte KOH-concentration: the higher the electrolyte concentration, the lower the solubility. In the work of Haug et al.[25], the decrease of solubility is explained by the 'salting out effect'. Secondly, it affects the diffusion coefficient as well, Tham et al.[83] did an elaborate experimental study on diffusion coefficients in 1970. The conclusion can be reported simply: the higher the electrolyte concentration, the lower the diffusion coefficient. In conclusion, both effects tend to decrease transfer of species to the other side of the separator. This conclusion is confirmed by the experimental data presented in Figure 2.15. Similar to the influence of temperature on crossovers, the effects dwindles at relatively large current densities.

Supersaturation
Supersaturation happens if the concentration of a dissolved species exceeds its saturation concentration, at a given temperature, pressure and electrolyte concentration. Trinke et al.[86] report that it is

[8] According to Schalenbach et al.[69], the diffusion coefficient is found to fit an Arrhenius equation, see Equation 2.12, in which a temperature increase indeed results in a higher reaction rate constant, or in this particular case, a higher diffusion coefficient.

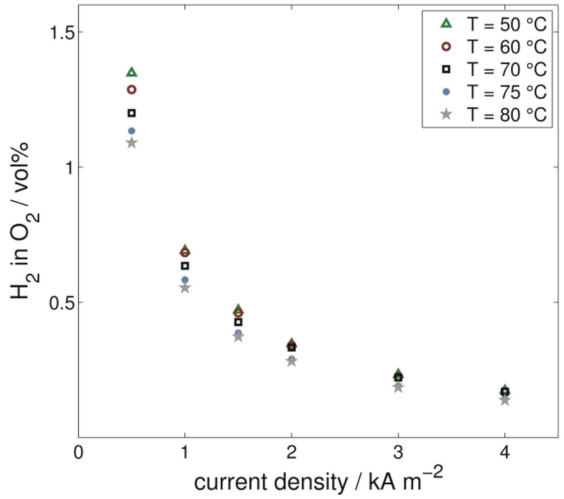

Figure 2.13: Influence of operating temperature on H_2-crossover at different current densities, mixed electrolyte cycle
Image taken from the work of Haug et al. [25]

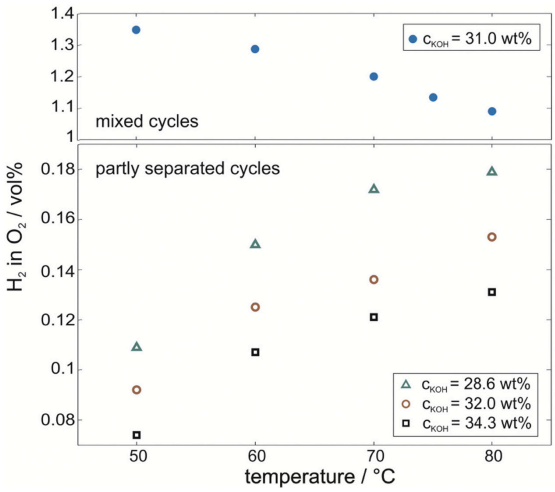

Figure 2.14: Influence of operating temperature on H_2-crossover at different current densities, fundamental difference between mixed and separated cycles
Image taken from the work of Haug et al. [25]

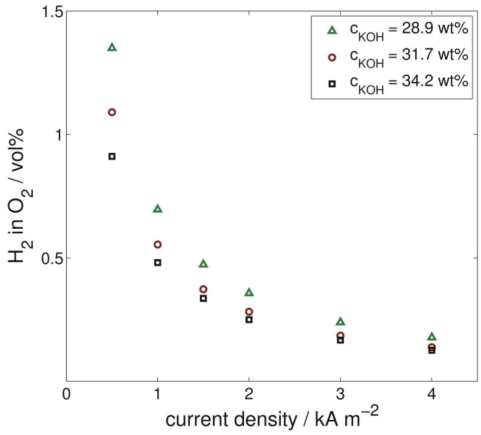

Figure 2.15: Influence of electrolyte concentration on H_2-crossover at different current densities.
Image taken from the work of Haug et al. [25]

generally assumed that gas bubbles are formed from dissolved species and that electrolysis products are formed primarily in dissolved form. Nucleation sites, in the form of surface irregularities (depending on material and surface roughness), are necessary to form bubbles. For the nucleation sites to become active a sufficient deviation from equilibrium concentration is required [91]. So the electrolyte needs to be supersaturated (locally) prior to nucleation of bubbles. The supersaturation has been found experimentally [50].
Evidently, the degree of supersaturation is in itself situation dependent, due to different operating conditions and different materials and surface roughness. But the degree of supersaturation is highly influencing crossover [25, 91], as the reasoning given at the beginning of this subsection holds: the higher the concentration of a species, the higher the crossover is expected to be.

Parameter	Effect	Reason
Pressure	Increase	Higher concentration gradient
Temperature	Decrease	Reduced solubility dominates over increased diffusivity
Current Density	Decrease	Constant absolute crossover portion, reduced relatively
Electrolyte Concentration	Decrease	Reduced solubility & diffusivity
Supersaturation	Increase	Higher concentration gradient

Table 2.3: A brief summary of the effects of different influential parameters on crossover. In the column labelled 'Effect', the expected effect on crossover is listed if an increase of the corresponding parameter is considered.

2.5. Alkaline Electrolyser Control Systems

Water electrolysis inherently involves evolving gasses that could form an explosive mixture. The two gases evolve at different rates and gas mixture should be prevented at all times. Therefore a robust and reliable control system is essential to safe operation. In general, explicitly described control mechanisms of electrolysis systems are not found in scientific literature [18].
According to Kreuter et al. [44], the first large scale electrolysis system operating at elevated pressure was developed by engineer Ewald Zdansky and patented by the Swiss Company Lonza SA in the 1940's. A detailed system description, including the control system, can be found in reference [48] [9]. As can be seen in Figure 2.16, various auxiliary equipment is necessary to operate a (pressurised) electrolysis system. The resemblance to ZEF's system comes forward in chapter 3, where ZEF's system is explained in detail.

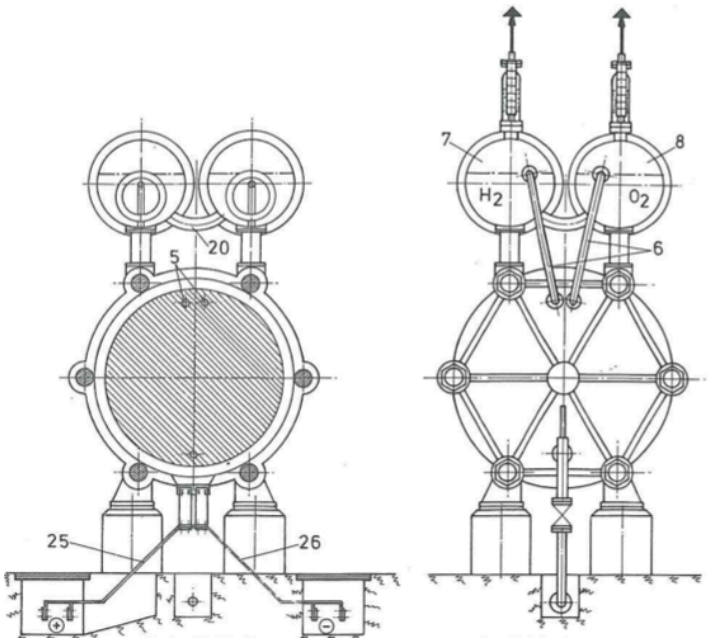

Figure 2.16: A cross-sectional overview of the first reported pressurised alkaline electrolysis system Developed by Zdansky et al. for the Swiss company Lonza in 1940's [48]

Although the working principles and even the physical appearance of the Lonza system and ZEF's system show resemblance to a large extent, some important distinctions are noteworthy. The most important difference between the two is the pressure equalisation tube, indicated by number 20 in Figure 2.16. This tube is directly linked to the two flash tanks below the liquid gas interface and primarily facilitates equalisation between the two liquid levels, corresponding to pressure equalisation in the oxygen and hydrogen flash tanks. But, it probably facilitates large crossovers too and therefore ZEF's system has a different pressure equalisation configuration as is explained in the next chapter.

[9] The rights of the high pressure electrolyser was sold to a German Company by the name of LURGI, which published the technical description (which is referred to) of the high pressure electrolyser

The second important distinction lays in the electrolyte mixing; the degassed electrolyte recirculating from the flash tanks back to the stack is pumped and mixed to one single electrolyte feed to the stack. Again this might be a source of crossover and ZEF's electrolyte circulation is subdivided into a hydrogen and oxygen side.

Ju et al. [38] present a system in which liquid level equalisation is obtained via mass controllers at the oxygen and hydrogen outlets of the flash tanks, whereas ZEF's system makes use of level sensor control. In this system, level sensors are used as an emergency tool: if the liquid level rises up to 70% of the flash tank, the power supply is switched off to prevent flash tank overflow resulting in exposure to corrosive fluids [38].
In the work of Janssen et al. [37], pressure and level sensors are used to control liquid levels in the two cell compartments. Exceeding the design pressure causes the oxygen control valve to open. Secondly, the pressure and level difference this valve opening induces, triggers the hydrogen control valve to open, such that liquid levels are equalised.

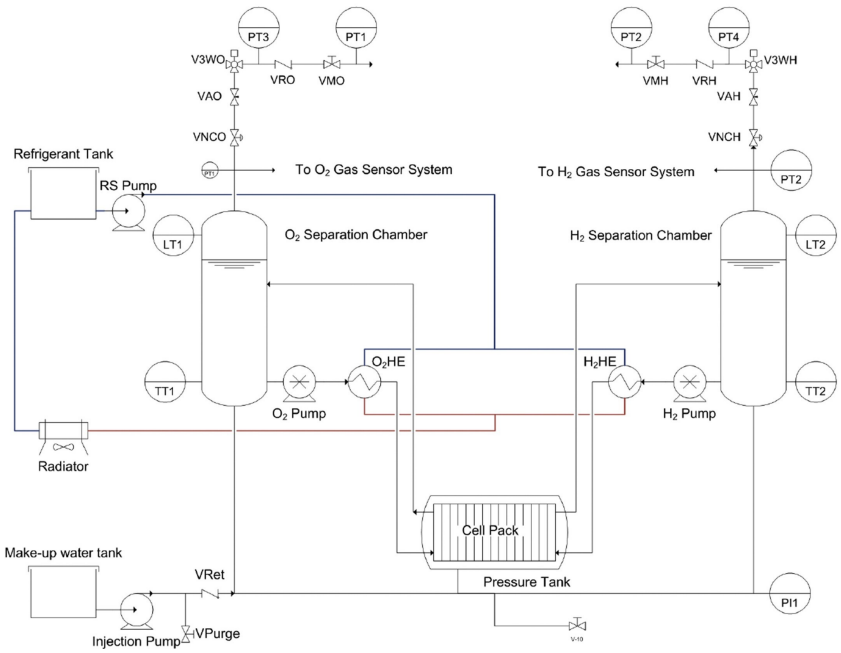

Figure 2.17: Piping and instrumentation diagram of the system on which the model of David et al. is based. Original image can be found in the work of David et al. [19]

In a recent work by David et al. [19] a (experimentally validated) model to predict gas and liquid flows, pressure build-up, and crossovers is presented in a self-pressurising alkaline electrolyser. Influence of sudden valve opening is investigated in the study on crossovers, local pressures, and pressure gradients across the membrane[10]. The system evaluated int he the work of David et al. does have separate electrolyte circulation systems and a strategic pressure equalisation configuration, both similar to ZEF's system. The P&ID of the modelled system can be seen in Figure 2.17. Flash tank pressures and liquid levels are controlled by motorised valves that release production gasses. Although the resulting behaviour (in terms of liquid levels, pressures and pressure differences) is very much similar to the model inspired by ZEF's system, the control scheme/algorithm is not explained in detail. Concluding that the place of ZEF's control algorithm (which is detailed in chapter 3) in the world of alkaline electrolysis is not explicitly determined, although a lot of similarities can be seen between ZEF's electrolysis system and others found in literature.

[10] A similar detailed modelling of ZEF's system is done by Ilias Daniil [18] and reveals interesting results, which are included in section C.2

3

Basis of Design

Conventionally, a *Basis of Design* (BoD) is made prior to the actual design. It serves as a document to record every line of reasoning in decision making with respect to the design. It maps the 'What', often documented in the *Owner's Project Requirements* (OPR), to the 'How'. First it takes the (often non-technical) desired requirements and structures them into distinguishable technical functions, purposes and subsystems [80].
However, the BoD of ZEF's electrolysis system is somewhat different, as it is made in retrospect and therefore the 'why' questions are central. Specifically recording design considerations is very convenient, both for future engineers to acknowledge reasoning made in the past and for keeping the overview. The latter is especially beneficial in an integration of different subsystems.

3.1. System Description

Due to IP reasons, the detailed system design, summation of the open ends toward an integrated setup and the new system design can be found in Appendix C.

4

Experimentation & Methodology

In this chapter the experimental methods are explained, through which the obtained system is characterised and the research questions answered. The complete balance of plant (BoP) is redesigned to solve all aforementioned open ends, therefore system behaviour and performance have to be redetermined and the implemented solutions have to be examined.
To answer the first main research question an operational envelope is mapped experimentally and its limitations characterised
Secondly, relevant system traits that are complementary to the operational envelope are captured. Lastly, to answer the second main research question, electrolyte samples are analysed to investigate possible deterioration of the electrolyte over time.

4.1. Determination of the operational envelope

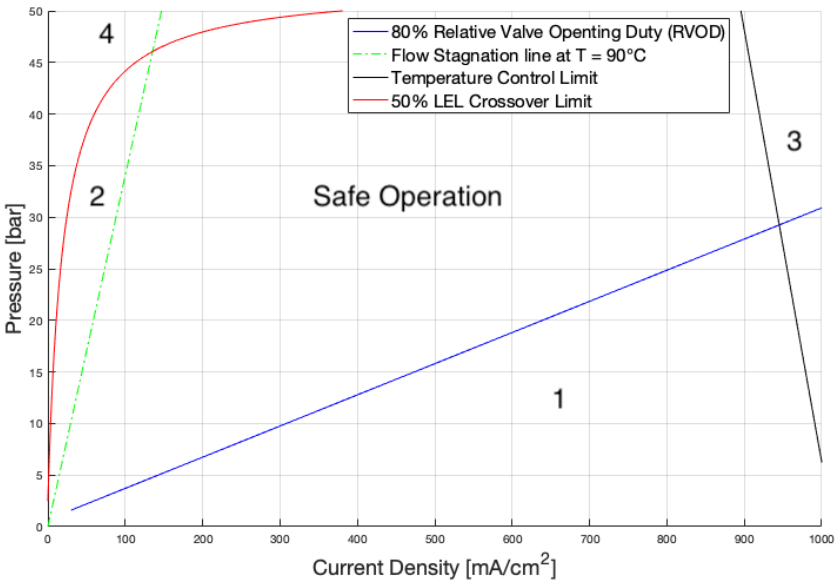

Figure 4.1: Qualitative representation of a possible operational envelope. The current density-pressure characteristics of the four limitations are found experimentally:

1. The 80% RVOD limitation is based on a model involving the capillary tubes as described in subsection C.3.5.
2. The flow stagnation limitation is based on the work of Kleist [39].
3. The temperature control limitation is neither based on previous work nor on models, but is depicted indicative only: a possible limitation with its expected shape, orientation and approximate location on the operational envelope.
4. The crossover limitation is based on the work of Mulder [53], the work of Brauns et al. [13] and on the work of Trinke et al. [86].

The main deliverable of this thesis is the operational envelope of ZEF's integrated AEC setup. An operational envelope is a schematic depiction of all safe operating points of a system, expressed in

terms of relevant parameters. The operational envelope of the integrated AEC system is determined experimentally, focusing on mapping the limitations in terms of current density, pressure and temperature. In Figure 4.1 a qualitative example of a complete operational envelope can be seen. The four possible limitations and the corresponding shape in Figure 4.1 are detailed in the upcoming subsections.

4.1.1. Relative Valve Opening Duty

As explained in subsection C.3.5, the RVOD system characteristic is a consequence of the implementation of capillary tubes and accompanying opening times that followed from a steady state mass-balance and laminar flow model which is based on a fixed discharge volume.
The experimentation regarding this specific limitation consists of logging the cycle times of oxygen and hydrogen purge cycles. Cycle time is defined in Equation C.7 as the sum of the time a valve is closed and opened during a single purge. The current, pressure and temperature of the electrolyte are measured and used to deduce valve opening times which are imposed on the valves by the control scheme. Consequently, the cycle times are monitored and used to validate the model.
Three important notions are in place. Firstly, the developed model considers steady state operation and therefore assumes a constant pressure and temperature. In reality however, both temperature and pressure are dynamic quantities and change throughout a valve cycle. Particularly pressure is influenced by valve openings and can deviate up to 20% [1], which in turn influences the molar flow rate through the capillary tubes. During the cycle time experiments, pressure is monitored and averaged such that cycle times can be verified approximately.
Secondly, the model treats the oxygen and hydrogen sides independently, but in reality the two are highly intertwined. For example, if the hydrogen purge valve is opened due to an exceedance of the control pressure, the hydrogen level increases and consequently the oxygen side electrolyte level decreases, leading to a shorter cycle time on the oxygen side. On the other hand, if oxygen is purged due to the middle level sensor on the oxygen side falling dry, the opposite effect is expected. An additional pressure drop is present during the hydrogen purge valve cycle time monitoring and therefore a longer cycle time is expected to be observed in comparison to the calculated cycle time.
Lastly, the capillary tube model on which the cycle time model is based is imperfect and therefore deviation from the calculated cycle times are expected, model deviates up to 10% [93].

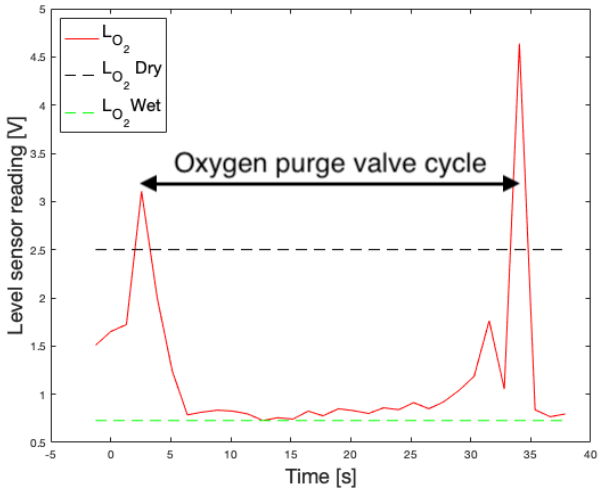

Figure 4.2: A typical example of an oxygen purge valve cycle as monitored in the experimental setup
Operating conditions: $3.8\,\mathrm{bar}$, $20\,^{\circ}\mathrm{C}$, $64\,\mathrm{mA\,cm^{-2}}$

Hydrogen purge valve cycle time measurement

The aforementioned examples exemplify that the control scheme for normal operation has to be adjusted to validate the cycle times under different operating conditions in order to avoid valve interfer-

[1] Based on a back-of-the-envelope calculation, given the discharge volume, the total gas volume in the buffer tank and assuming an adiabatic expansion ($p \cdot V^{c_p/c_v} = constant$)

ence. To validate the hydrogen purge valve cycle time, oxygen level control is switched off and the additional pressure drop is avoided. The time between two actuations of the hydrogen purge valve is measured as a cycle time.

Oxygen purge valve cycle time measurement
To compare the actual cycle times of the oxygen purge valve to the calculated cycle times, pressure control is switched off, so that the electrolyte level are not disturbed by hydrogen purging. The aforementioned pressure correction is applied during these experiments. The cycle times are measured as the time between to two subsequent droughts of the middle electrolyte level sensor on the oxygen side sensor. An example of how the oxygen purge valve cycle time is monitored can be seen in Figure 4.2.

4.1.2. Flow Stagnation

Flow stagnation in ZEF's electrolysis system is first reported by Kleist [39]. In his work, flow stagnation is defined as a certain period of time in which the product gas stops flowing through the top channel of a cell to the header. The explanation can be found in coalescence of bubbles and bubble growth at the top of a cell to a size large enough to block the top channel. The series of events before, during and after flow stagnation are depicted in Figure 4.3. Detailed analysis of this phenomenon can be found

Figure 4.3: A qualitative representation of the sequential events during a flow stagnation cycle

in the work of Kleist [39]. Besides, the relevance of avoiding flow stagnation is illustrated in his work; during a flow stagnation experiment the product gas caught fire inside the stack. The working principle being illustrated in Figure 4.3, the competing forces governing flow stagnation emerge to be buoyancy, responsible for the electrolyte circulation flow, and surface tension on the other hand. The latter is considered to be fixed at a given temperature, electrolyte and gas composition and is related to the increase in curvature of a bubble required to pass through the top channel, expressed as a Laplace pressure.
However, buoyancy force is directly proportional to the gas volume in the riser, which is a function of the void fraction and riser height, as can be seen in Equation C.2. The void fraction in the riser is proportional to the number of cells and the volume production in each cell and therefore depends on operating conditions directly. In other words, a sufficient gas volume flow rate prevents flow stagnation, because enough buoyancy force is generated to overcome the Laplace pressure at all times.
This is in correspondence with the experimental data set of Kleist, in which flow stagnation was observed dominantly on the oxygen side where gas volume production is only half of the gas volume production at the hydrogen side.
The critical volume flow rate is drawn from the experimental data set and can be seen as a system characteristic. For different experiments, a number of critical volume flow rates are determined and

a maximum value of 3.4 is found (at $500\,\mathrm{mA\,cm^{-2}}$, $47\,^{\circ}\mathrm{C}$ and $47\,\mathrm{bar}$). Taking the most conservative value, a concrete flow stagnation criterion is deduced in terms of the operating conditions and can be seen in Equation 4.1. In this equation i is the current density in Ampère per squared centi meter, T temperature in Kelvin and system pressure p is expressed in bar, taking over the units used in the work of Kleist.

$$\frac{i \cdot T}{p} > X \qquad \text{Flow stagnation prevention criterion, previous setup X=3.4} \tag{4.1}$$

The green line in item 4.1 represents the limit at which this inequality holds. Operation in the area indicated by the number 2 induces a risk of flow stagnation and is therefore considered a limitation of the operational envelope. Only one line, at $90\,^{\circ}\mathrm{C}$, is depicted for clarity reasons. In Figure 4.4, three different flow stagnation lines are depicted corresponding to $30\,^{\circ}\mathrm{C}$, $55\,^{\circ}\mathrm{C}$ and $90\,^{\circ}\mathrm{C}$. As Figure 4.4 shows, flow stagnation typically occurs at high pressures in combination with a low current density. The flow stagnation lines in Figure 4.4 and item 4.1 are based on experiments on the previous electrolysis setup. As the buoyancy force depends on the riser height and number of cells as explained above, the new system is therefore expected to be less prone to flow stagnation. This results in a smaller flow stagnation prevention criterion value, steeper flow stagnation lines and consequently a larger operational envelope with respect to flow stagnation limitation.

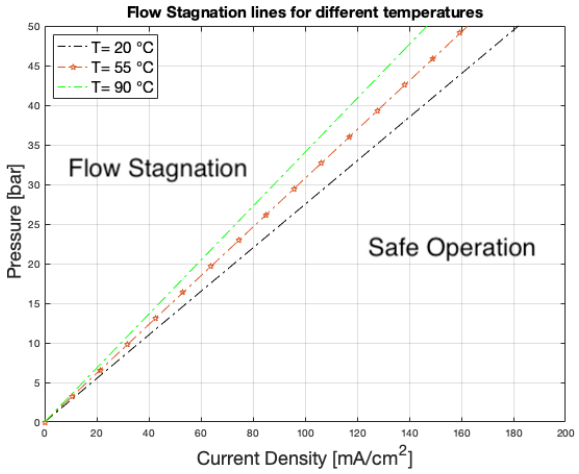

Figure 4.4: Flow stagnation lines at different temperatures. At a given temperature, flow stagnation can be avoided by operation under conditions on the right hand side of the corresponding flow stagnation line.

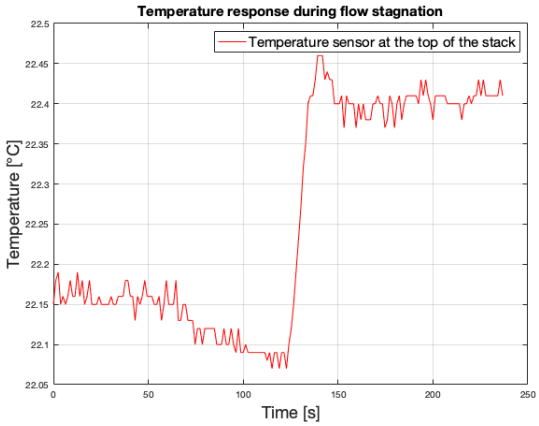

Figure 4.5: Temperature response during a flow stagnation cycle. Temperature sensor is placed on top of the midplate on the oxygen side, at the start of the riser column.

Flow Stagnation Measurement

Two different aspects are used to detect flow stagnation. First and foremost, the temperature response of the temperature sensors at the top of the stack are captured, an example of which is given in Figure 4.5. The fluid flow in the riser stops and therefore the stagnant liquid in the riser cools down, which is indicated by the small temperature decrease right before the sharp rise in Figure 4.5. The sharp rise in temperature indicates sudden continuation of flow in the riser and the heated liquid in the cells passing the temperature sensor. The use of this characteristic temperature response to detect flow stagnation is developed and verified by Kleist, in which video footage confirmed the characteristic temperature response related to flow stagnation.

Secondly, one header channel is visible and distinction between a stagnant electrolyte and a two-phase flow is made visually.

4.1.3. Temperature Control

As explained in subsection C.3.2, a finned tube heat exchanger is implemented to achieve temperature control. The highest allowable temperature is $90\,^{\circ}\mathrm{C}$ and is limited by material properties of the stack. Heat is generated by the overpotentials in the stack; as explained in chapter 2 the overpotential increases with increasing current density and so the heat generation. The electrolyte heats up in the cells, circulates and is cooled in the tanks and downcomers by natural convection for one part and

by forced convection by the crossflow fans. The temperature control system is designed to cool the electrolyte only and leaves the heat generation to the stack itself, resulting in an inherent partial temperature control. At relatively low current densities for instance, overpotentials are small and therefore heat generation is relatively small and passive convection suffices to keep the electrolyte at a constant temperature, as was observed in past generations of ZEF's electrolysis system [39, 53]. The degree of temperature control is experimentally characterised by a minimum and a maximum achievable temperature at a given current density. The minimum steady state operational temperature at a given current density is found by operating the cross-flow fans at maximum capacity. The maximum achievable temperature at a given current density is found by operation without the cross flow fans. A possible outcome of the experiments can be seen in Figure 4.6, in which the green area represents the possible reachable temperatures. The modest pressure dependency of the temperature control limitation of the

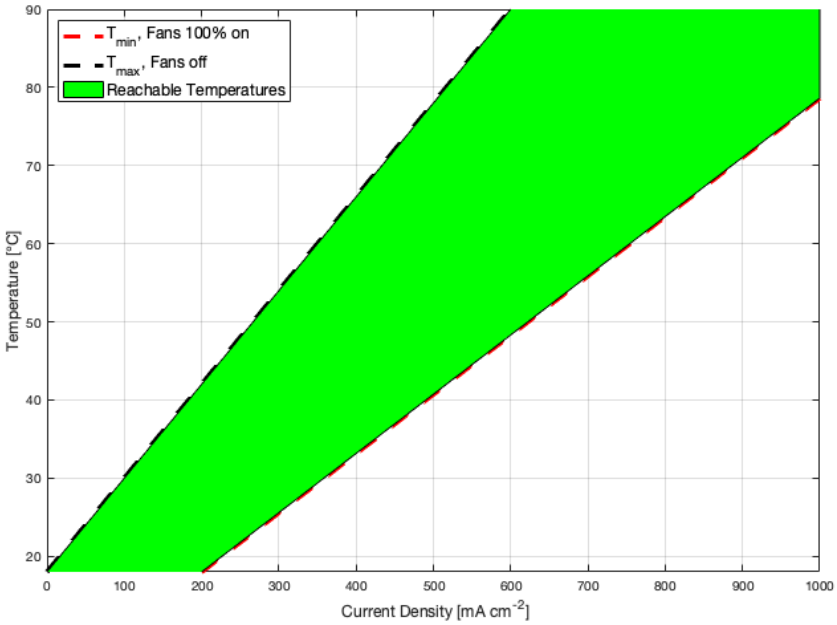

Figure 4.6: Qualitative representation of possible reachable temperatures at different current densities at a constant pressure

system, as depicted in the indicative operational envelope in item 4.1, is a consequence of decreasing gas volume production with increasing pressure at constant temperature and current density. As explained in previous sections and in particular in section B.1, the gas volume production determines the level of flow circulation and is therefore a determining factor in the heat transfer.

4.1.4. Crossover

In section 2.4, the influence of operating parameters is discussed and in Table 2.3 a brief summary of the influential parameters can be found.
Recapitulatory, an increase in pressure is associated with an increase in crossover, an increase in temperature is associated with a decrease in crossover. However, the decrease of crossover related to an increase in current density typically dominates the other influences [13]. Resulting in the red line depicted in item 4.1, the area indicated by number 4 is restricted due to crossover. The red line is based on literature [13, 86] and on the crossover performance of ZEF's previous system. An important notion is in place: as explained in subsection C.3.1, the stack design is adjusted drastically to solve the crossover limitations found in ZEF's previous electrolysis setup [53]. Consequently, the crossover limitation is likely to deviate substantially from previously determined crossover limitations, hence the red line is indicative only and not a quantitative estimate. Nevertheless, the hypothesis of parasitic hydrogen production and applied solution are experimentally validated.

Crossover measurement

Oxygen crossover is measured by an optical oxygen sensor, the specifications sheet can be found in section B.5. The output signal is converted to a volume percentage and subsequently compared to the

UEL. Up to 50% of the UEL (and LEL) is deemed safe in industry [86, 14]. The sensor head is placed in a PVC sensor housing to secure an accurate measurement and avoids mixing with the surrounding air, details and demonstrations of many repeatable crossover measurements are included in the work of Mulder[53].
Measurement of hydrogen crossover is less straightforward, as the pure oxygen environment showed to impose a relatively high deterioration rate on the electrochemical sensor used in ZEF's previous electrolysis setup. The more commonly used caloric sensor or the catalytic metal-oxide sensor cannot withstand the high oxygen content to which it is exposed [15]. Commercially available electrochemical hydrogen sensors, such as the K1550 from KI Instruments used in the works of Brauns et al.[13], Haug et al. [26] and Trinke et al.[86], are deemed too expensive. Therefore, gas chromatography is chosen as final option through which the gas composition on the oxygen side is measured. Gas samples at different temperatures, pressures and current densities are taken and analysed using the Varian CP-4900 Micro-GC. Starting at a point of which the measured crossover definitely exceeded the 50%LEL in the previous setup, $50\,\mathrm{mA\,cm^{-2}}$, $50\,\mathrm{bar}$ and $20\,^{\circ}\mathrm{C}$ and depending on the outcome, the current density is increased or decreased at constant temperature and pressure. A schematic of the bisection search to the 50% LEL induced limitation can be seen in Figure 4.7.

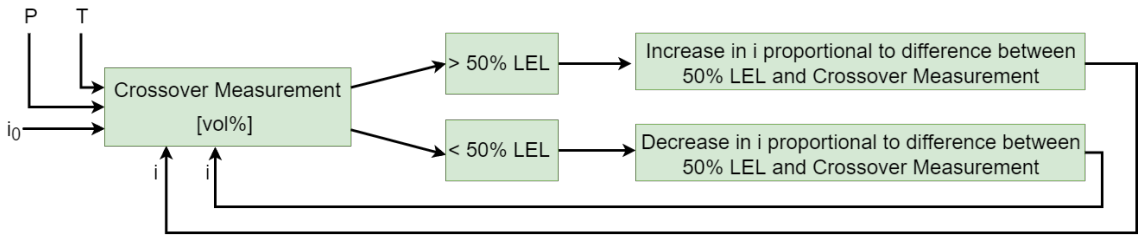

Figure 4.7: Schematic description of bisection search used to find the 50% LEL induced limitation on the operational envelope at a given pressure and temperature.

4.2. General system characteristics complementary to the operational envelope

The second line of research has a generic character, focusing on finding character traits of the new BoP design and capturing all relevant information complementary to the operational envelope. In section C.3, all described elements are included to improve the system in different ways and therefore, their performance are to be examined. The relevance of this research line originates from the fact that not all adjustments to the BoP design are expressed in the operational envelope necessarily. For example, testing the degasser replenishing method. In addition to examination of expected system behaviour, this research line captures all relevant unforeseen system traits and design deficiencies that may arise during experimentation. Besides relevant foreseen and unforeseen general system traits that are not captured in the operational envelope, this research line is intended to give the reader a general sense of how the system as a whole performs. Therefore, efficiencies and power consumption are captured and electrolyte mass flows are calculated using an energy balance. Ultimately, relevant aspects, such as efficiencies are compared to targets set by ZEF and to industry standards.
This research line does not require any additional experiments beforehand. Objectives of this research can be summarised by the following three points:

- Relevant system/operational traits not captured in the operational envelope.
- Relevant unforeseen system traits and design deficiencies.
- General system properties: H_2-production rates, efficiencies, power consumption related to the ZEF-targets and compared to industry and literature.

4.3. Electrolyte Deterioration

The electrolyte deterioration has not been inferred experimentally in previous generations of ZEF's AEC setup. Insight in electrolyte deterioration and the possible contamination by carbonates is a relevant

outcome to infer the performance of the installed degasser and forms the first step in the lifetime analysis of the AEC-branch of the micro plant. The electrolyte deterioration due to CO_2 contamination is not a complete characterisation of possible system performance deterioration over time. For example, deterioration of nickel electrodes is described as a different source of significant loss in electrolysis performance in literature and is caused by hydrogen absorption and hydride formation [65, 78, 74].

Reference Calculations

The CO_2 in the feed water is involved in several equilibrium reactions, which are listed below in the left column. The degasser is intended to shift the first reaction to the gaseous CO_2 by removing the CO_2 adhered to the O_2-rich bubbles, such that the equilibrium is not sustained but the reaction rate of the forward reaction is larger than the reverse reaction, essentially removing the dissolved CO_2.
The right column of the chemical reaction equations shown below display the reactions occurring in the electrolyte, if the carbonates of the feed water are introduced to the electrolyte. The right columns starts with the acid-base reaction, between the hydroxide (OH^-) and the hydronium (H_3O^+) ions. The other two reactions shown in the right column display a deposition reaction between potassium and the available carbonates. In the following analysis is the consumption of hydroxide ions in the acid-base reaction assumed to be solely responsible for the loss of conductivity of the electrolyte. This assumptions is made to simplify the effect of residual CO_2 in the feed water, analogously to the analysis made in the work of Nauta [55]. In reality, the formed carbonate ions are charged and therefore have a contribution to conductivity in principle. On the other hand, carbonates might induce side reactions that lead to passivisation [55].As the chemical equilibria show, the amount if consumed hydroxide ions depends directly on the moles of CO_2 in the feed water. The work of Nauta shows a linear dependency of the KOH concentration decrease and the number of moles CO_2 present in the feed water.

$$CO_{2(aq)} \Leftrightarrow CO_{2(g)} \qquad H_3O^+_{(aq)} + OH^-_{(aq)} \Leftrightarrow H_2O_{(l)}$$

$$CO_{2(aq)} + H_2O_{(l)} \Leftrightarrow HCO^-_{3(aq)} + H_3O^+_{(aq)} \qquad HCO^-_{3(aq)} + K^+_{(aq)} \Leftrightarrow KHCO_{3(s)}$$

$$HCO^-_{3(aq)} + H_2O_{(l)} \Leftrightarrow CO^{2-}_{3(aq)} + H_3O^+_{(aq)} \qquad CO^{2-}_{3(aq)} + 2K^+_{(aq)} \Leftrightarrow K_2CO_{3(s)}$$

The following analysis is based on the work of Nauta and adjusted to the system dimensions of the acquired electrolysis system. Given the ZEF-target of 20 years lifetime and starting from a maximal allowable electrolyte deterioration of 10 % KOH concentration decrease, the maximum allowable CO_2 concentration allowed in the feed water can be deduced.
The model made by Nauta determines that 3.5 $wt\%CO_2$ corresponds to a 10% loss of hydroxide concentration. Subsequently Equation 4.2 is used to determine the total allowed number moles of CO_2 given the 3.5 $wt\%$, the electrolyte volume of $1.1\,\mathrm{L}$, the electrolyte density of $1.292 \times 10^3\,\mathrm{g\,L^{-1}}$ and the molecular weight of CO_2, $44\,\mathrm{g\,mol^{-1}}$. The total allowed number of moles n_{CO_2} is $1.13\,\mathrm{mol}$.

$$n_{CO_2} = \frac{CO_2wt\% \cdot 10^{-2} \cdot V_e \cdot \rho_e}{MW_{CO_2}} \qquad (4.2)$$

$$x_{CO_2} = \frac{n_{CO_2}}{3 \cdot n_{CH_3OH} \cdot 365 \cdot LT} \qquad (4.3)$$

As described in the work of Dimitrou [20], the degasser is designed for a system producing approximately $20\,\mathrm{mol\,d^{-1}}$ methanol. With a lifetime, denoted LT, of 20 years and the deduced maximum number of moles of CO_2, the maximum allowable CO_2 concentration in the feed water is determined to be $2.58\,\mathrm{ppm}$ or $1.43 \times 10^{-4}\,\mathrm{mol\,L^{-1}}$ via Equation 4.3.
The experiments described by Al Shareef, show a CO_2 concentration of below $2.5\,\mathrm{ppm}$[3], the expectation is therefore that the estimated electrolyte lifetime based on the experiments is at least 20 years.

Methodology

The impact of CO_2 residues on ZEF's electrolysis system has not been inferred experimentally in the past as mentioned before. For the first time, the degasser is put into use with pure oxygen and in the dynamic environment which has only been simulated before. Besides the dynamic use of the degasser, the impact of the carbonates, salt deposition and the hydroxide concentration decrease are

experimentally investigated by making use of Inductively Coupled Plasma (ICP), with which the potassium level in the electrolyte is measured. Moreover, it detects a large variety of possible contaminants, which possibly gives insight in electrolyte deterioration by phenomena yet unknown. In principle, ICP delivers the total potassium level in the sample, both the potassium dissolved in the electrolyte as ions and the potassium bonded as potassium (hydrogen) carbonate. Therefore, the samples are taken from the electrolyte level in the buffer tanks, the highest possible locations in the system, such that the deposited potassium carbonate salts are unlikely to end up in the electrolyte sample. By taking electrolyte samples throughout time, the amount of deposited potassium carbonates is estimated by taking the difference between the potassium level in the ICP samples and the benchmark potassium level which corresponds to a sample of unused electrolyte.

5

Results & Discussion

In this chapter, outcomes of the aforementioned experimentation are central. The interpretation and explanation of the outcomes is essential to come to a complete understanding of the system and to validate design adjustments as described in section C.3.
The experimental operational envelope, the main deliverable of this thesis, is presented in the first section and the four limitations are detailed in corresponding subsections. Regarding the four limitations, performance of the integrated AEC setup is compared to the previous setup and to alkaline electrolysis systems found in literature if applicable and possible. In the second section, relevant characteristics not captured in the operational envelope are presented. Furthermore, different design choices are validated and possibly reconsidered and the performance of the acquired setup is compared to the targets set by ZEF. Additionally, relevant unforeseen outcomes (and additional experimentation) are included. Lastly, in the third section the outcomes of the deterioration experiments as described in section 4.3 are presented and examined.

5.1. Operational Envelope

The operational envelope is considered the main deliverable of this thesis and can be seen in item 5.38. The following subsections show the results, interpretation and analysis of the results of the experiments and accompanying limitations.

5.1.1. Relative Valve Opening Duty

The relative valve opening duty (RVOD) experiments serve two purposes. First and foremost, finding the operational limitations of the capillary tubes on the operational envelope. Secondly, validation of the RVOD model presented in subsection 4.1.1 (based on the capillary tube sizing which is reported in subsection C.3.5). So that capillary tubes can be selected in future generations of ZEF's electrolysis system in case different control algorithms or buffer tank sizes are implemented. Data is extracted at different pressures, temperatures and current densities; the data extraction can be summarised as follows:

1. Pressure, current and temperatures are plotted directly from the raw data.
2. A relatively long period of operation under the same pressure and current is selected.
3. The number and duration of valve openings are retrieved from the log-file corresponding to the period which has been selected.
4. The average cycle time is calculated by dividing the total period length by the number of valve openings. The logged opening times and the temperature are averaged and subsequently the RVOD is determined.
5. For the same pressure, current density and temperature the corresponding cycle time and RVOD are calculated by the model. Subsequently the experimental values and the modelled values for the cycle time and RVOD are compared. The Matlab code and experimental data used to validate the opening time model can be found in section B.6.

In the coming two subsections, the results of the RVOD experiments are presented and compared to the modelled valve opening times. Subsequently, explanations and solutions to the established discrepancy are formulated and a corrected model is presented. A schematic depiction in Figure 5.1 summarises the RVOD experiments and outcomes.

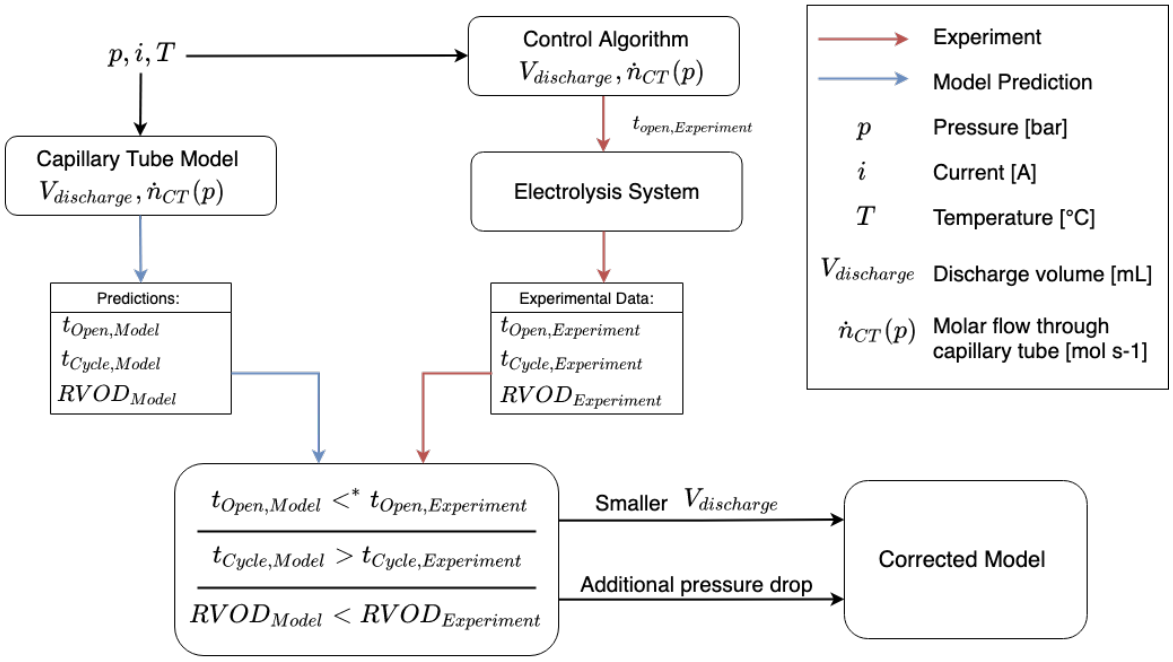

Figure 5.1: Schematic depiction of the relative valve opening duty experiments, outcomes and development of the corrected model. The asterisk ($*$) indicates an inequality that holds for the oxygen side only. The corrected model is based on the comparison between experiments and the model, a model in which the oxygen an hydrogen side valve timings were determined separately and independently.
The corrected model on the oxygen side: the additional pressure drop accounts for the O_2-valve opening directly after a H_2-valve opening and the smaller discharge volume accounts for the shortened cycle time due to the intervening H_2-valve opening which rises the electrolyte level in the oxygen tank and lowers the pressure at the moment of valve opening.
The corrected model on the hydrogen side: the additional pressure drop accounts for a physical, additional pressure drop over the capillary tube. The pressure drop results in a smaller discharge volume.

Cycle Time & RVOD: Oxygen side

The results of the RVOD experiments for the oxygen purge valve can be seen in Figure 5.2 and 5.3.

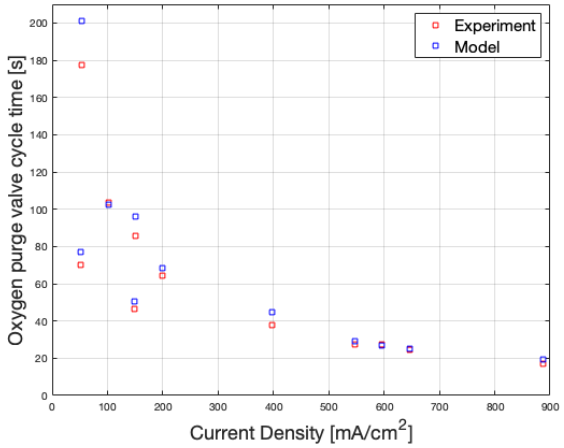

Figure 5.2: Cycle time versus current density of the oxygen purge valve. The values found with the experiments (red) and the values obtained form the capillary tube model at corresponding operating conditions (blue).

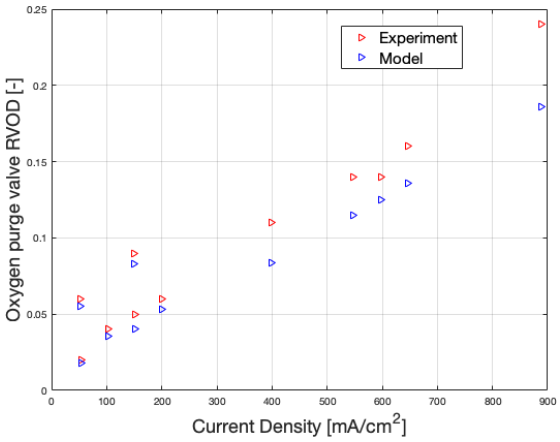

Figure 5.3: Relative valve opening duty versus current density of the oxygen purge valve. The values found with the experiments (red) and the values obtained form the capillary tube model at corresponding operating conditions (blue).

The experiments show shorter cycle times than the modelled cycle times and higher RVOD. As described in subsection 4.1.1, the opening times are governed by the operating conditions via Equation C.5 and a linearisation of the Darcy-Weisbach capillary tube model (relating molar flow through the capillary tube as a linear function of the pressure difference over the capillary tube).
However, the opening times implemented by the control algorithm and opening times as calculated by the model show deviation with respect to each other, see Figure 5.4.

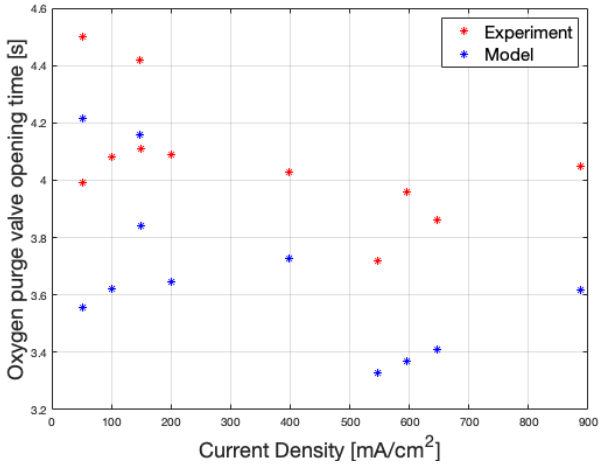

Figure 5.4: Oxygen purge valve opening time of the oxygen purge valve versus current density. The values found with the experiments (red) and the values obtained form the capillary tube model at corresponding operating conditions (blue).

Underestimation of the opening times

The model structurally underestimates the opening times implemented by the control algorithm and has a maximum of 10 % underestimation for the acquired data set.
Two possible sources of the discrepancy between opening times registered during experiments and the modelled opening times can be distinguished, besides the general notion that the opening times depend on a linear approximation of an imperfect model. First and foremost, the data acquisition is not done according to the steps described in subsection 4.1.1 due to time constraints, which results in the lack of independence between cycle time measurements between the hydrogen and oxygen side. Nevertheless, a large data base was available in which operating conditions and valve opening times are stored. An essential consequence of the interference of the H_2 and O_2 valve openings is that the

oxygen valve generally opens directly after the hydrogen valve [1] and therefore the oxygen purge valve opening times are determined by the control algorithm at lower pressures than in the model (which uses the time-averaged pressure), approximately 5 %[2].
If the pressures are corrected with an additional pressure drop to pressures at the moment of valve opening, a smaller overestimation is still observed, see Figure 5.5. An additional explanation is required to explain this residual discrepancy.

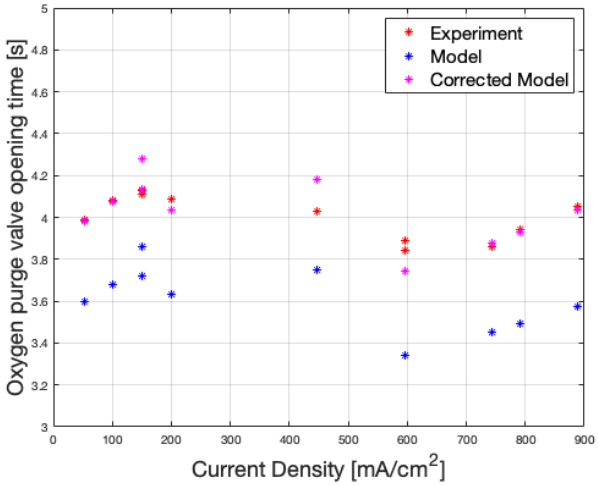

Figure 5.5: Opening times of the oxygen purge valve versus current density. The values found with the experiments (red) and the values obtained form the capillary tube model at corresponding operating conditions (blue) and the corrected model (magenta).

The second explanation for the discrepancy in the opening times is that the coefficients used in the linearisation of the capillary tube model are constant and corresponding to operation at $90\,°\mathrm{C}$. At low temperatures, this results in an underestimation of the molar flows through the capillary tubes and subsequently an overestimation of the opening times corresponding to the $1\,\mathrm{cm}$ electrolyte level rise. The difference in molar flows at different temperatures increases with pressure. At $50\,\mathrm{bar}$ the difference in (modelled) molar flow through the oxygen side capillary tube at $20\,°\mathrm{C}$ and $90\,°\mathrm{C}$ is a 12% decrease.

Overestimation of the cycle times
The cycle times show an opposite trend, the model overestimates the cycle time. Given the overestimation of the opening times, the closing times are significantly lower in the experiments compared to the model. Again, this can be attributed to the interference of the hydrogen purge valve openings, a hydrogen valve opening lowers the electrolyte level on the oxygen side and subsequently the level sensor becomes dry before the calculated closing time, effectively shortening its cycle. The combination of the larger opening time and shorter closing time in the experiments compared to the model results in a relative large difference between the modelled RVOD and the RVOD determined in experiments as can be seen in Figure 5.3. Recapitulatory, the interference of the hydrogen purge valve openings effectively shortens the oxygen purge valve cycle and essentially lowers the pressure at which the opening times are calculated and implemented by the control scheme. In Table 5.1, the outcomes, suspected causes and implications are summed up.
A correction model has been made to improve the predictions on cycle time and RVOD. The two aforementioned consequences of the hydrogen purge valve interference are adopted in the model as a

[1] A general trend is observed: if the control pressure is reached, the hydrogen valve is opened resulting in an electrolyte level drop in the oxygen tank. Thereafter the oxygen valve is opened due to the level sensor drought. The observed trend is considered a consequence of reaching the exact 1:2 ratio in the buffer tanks.

[2] The pressure drop due to the hydrogen purge valve opening can be determined by assuming an adiabatic expansion in the oxygen gas phase ($p \cdot V^{\kappa} = c$). Given that the electrolyte level drops approximately $2\,\mathrm{cm}$(based on the assumption that T_{open,H_2} is correct and corresponds to a $1\,\mathrm{cm}$ electrolyte level rise in the hydrogen tank, which corresponds to an approximate $2\,\mathrm{cm}$ electrolyte level rise in the oxygen tank) and the cylindrical buffer tank has a total length of $120\,\mathrm{cm}$. Assuming $\kappa = 1.4$ [93], the pressure drop is ~7 %, which has the same order of magnitude as the 5% found in the experiments (which were captured at the start of the oxygen valve opening and not necessarily at the end of the oxygen expansion due to the hydrogen purge valve opening).

pressure reduction of ~4.5 % and by a scaling of the discharge volume by a factor 0.95. Both values are found by a bisection optimisation in which the root mean squared error (RMSE) between the experimental cycle time and its corresponding model value has been minimised. The results can be seen in Figure 5.6 and 5.7 and 5.5.

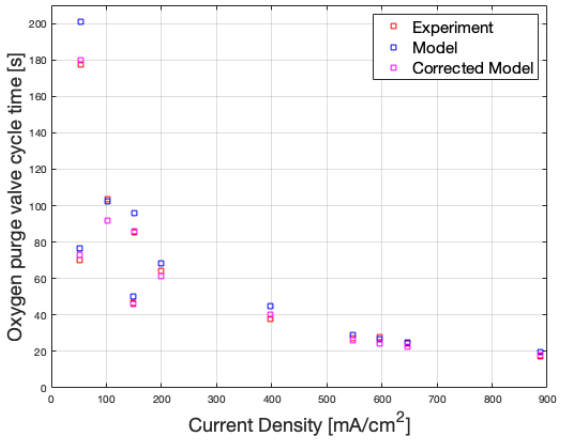

Figure 5.6: Cycle time of the oxygen purge valve versus current density. The values found with the experiments (red) and the values obtained form the capillary tube model at corresponding operating conditions (blue) and the corrected model (magenta).

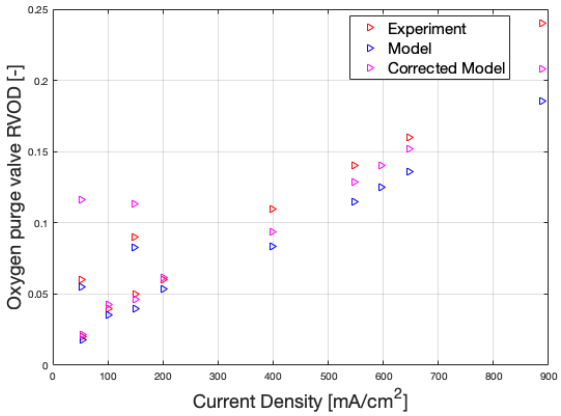

Figure 5.7: Relative valve opening duty of the oxygen purge valve versus current density. The values found with the experiments (red) and the values obtained form the capillary tube model at corresponding operating conditions (blue) and the corrected model (magenta).

The cycle times are captured more accurately (RMSE of the uncorrected model is twice the RMSE of the corrected model), nevertheless the modelled values deviate from the experimental values. The deviation in the RVOD is attributed to the fact that the modelled opening times correspond to a system with the pressure drop and smaller discharge volume due to the hydrogen purge valve opening, whereas the control algorithm calculates the opening times as if the discharge volume remained unchanged.

	Model vs. Experiment	**Cause**	**Implication**
$\mathbf{t_{Open}}$	M<E	O_2-Valve opening directly after H_2-Valve opening	p at moment of valve opening lower than average p
$\mathbf{t_{Closed}}$	M≫E	Valve interference	Smaller $V_{discharge}$/shortened cycle
$\mathbf{t_{Cycle}}$	M>E	Valve interference and pressure difference	Smaller $V_{discharge}$/shortened cycle
RVOD	M≪E	Combination of t_{Open} and t_{Cycle}	Underestimation of RVOD

Table 5.1: A brief summation of the RVOD experiments on the oxygen side. The outcome, a cause for the outcome and the implications of the outcome are displayed. The corrected model is made by applying an additional pressure drop and a decrease of the discharge volume, scaled according to a minimised RMSE between the experimental and modelled cycle times.

Cycle Time & RVOD: Hydrogen side

The results of the RVOD experiments for the hydrogen purge valve can be seen in Figure 5.8 and 5.9.

A similar trend as the oxygen purge valve opening is observed, except that the valve opening times are not necessarily overestimated that are therefore not depicted. A similar corrected model has been implemented to improve the prediction of cycle times and RVOD. The result of which can be seen in Figure 5.10 and 5.11. The additional pressure drop is found to be ~ 1.4% and a 9 % smaller discharge volume or, equivalently, shortened cycle.
The explanation and justification of the additional pressure drop and accompanying smaller discharge volume is however different from the reasoning given to explain the oxygen side discrepancy. Two relevant differences between the hydrogen and oxygen side can be made with respect to valve opening

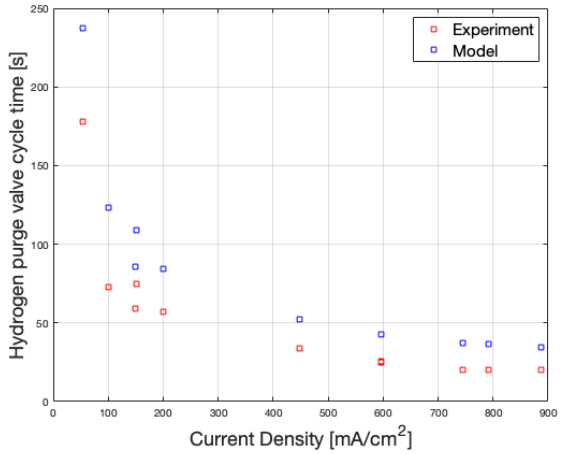

Figure 5.8: Cycle time of the hydrogen purge valve versus current density. The values found with the experiments (red) and the values obtained form the capillary tube model at corresponding operating conditions (blue).

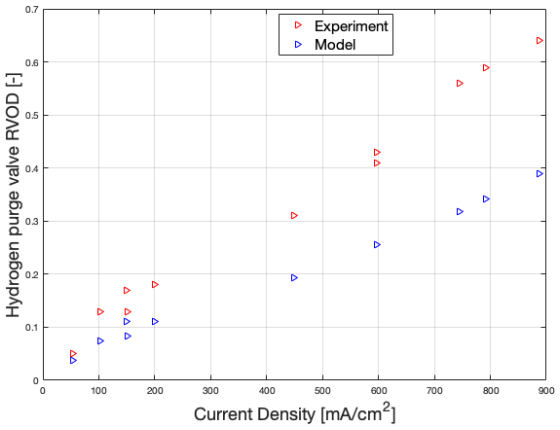

Figure 5.9: Relative valve opening duty of the hydrogen purge valve versus current density. The values found with the experiments (red) and the values obtained form the capillary tube model at corresponding operating conditions (blue).

times. Firstly, the hydrogen purge valve is opened when the control pressure is reached and is therefore not lower than the average pressure, hence the opening times are not necessarily overestimated, a different reasoning is required to explain the required pressure drop. The second difference is that the hydrogen side capillary tube has a significantly smaller diameter ($0.254\,\mathrm{mm}$ versus $0.127\,\mathrm{mm}$). This, together with the tube length, was a design choice, see subsection C.3.5, made from a safety perspective to ensure that the hydrogen side RVOD is higher than the oxygen side RVOD and electrolyte levels can be controlled under all circumstances. The unintended consequence is that the hydrogen side is more prone to clogging or other obstructions that induce an additional pressure drop, hence the required pressure drop is 1.4 % only. Another possibility is that the capillary tube is simply too long. The installed filters which intercepts particles that possibly block the capillary tubes have a $140\,\mu\mathrm{m}$ gap size; that is in between the diameters of the capillary tubes, so possibly an object with a size $127\,\mu\mathrm{m}$ to $140\,\mu\mathrm{m}$ (partially) blocks the capillary tube or contributes to an additional pressure drop. As can be read in subsection 5.2.2, observations of electrolyte droplets have been made on the low pressure side of the oxygen capillary tube. The electrolyte mist, or electrolyte droplets, possibly cause the additional pressure drop on the hydrogen side.

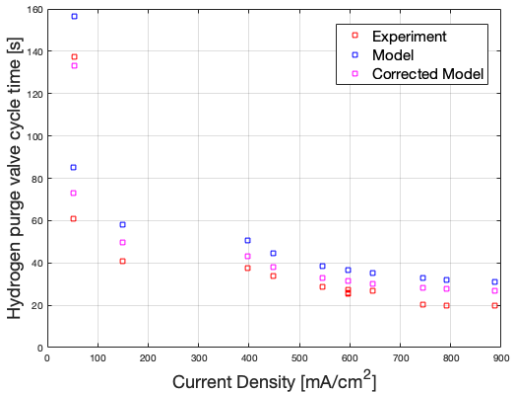

Figure 5.10: Cycle time of the hydrogen purge valve versus current density. The values found with the experiments (red) and the values obtained form the capillary tube model at corresponding operating conditions (blue) and the corrected model (magenta).

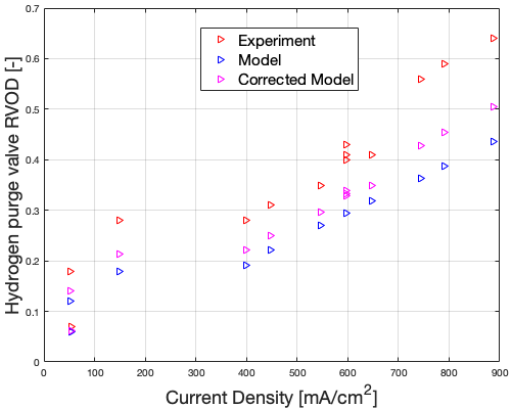

Figure 5.11: Relative valve opening duty of the hydrogen purge valve versus current density. The values found with the experiments (red) and the values obtained form the capillary tube model at corresponding operating conditions (blue) and the corrected model (magenta).

Analogously to the corrected model for the oxygen purge valve cycle time, the RVOD of the corrected model deviates significantly from the experimental values. This is attributed to the fact that the control

algorithm does not take in to account the shortened valve opening cycle (equivalent to the smaller discharge volume cycle) and therefore the opening times are relatively large and and the closing times relatively short, resulting in an overestimated RVOD. Therefore, the corrected model is considered to be the best representation of cycle times of the physical system if the valve interference is incorporated in the control scheme by means of an additional pressure drop and smaller discharge volume.

General findings
Additional to cycle time and RVOD comparison, two general finding with respect to the working of the capillary tubes are considered worth mentioning:

1. **Exact 1:2 ratio in the buffer tanks**
   A first general finding is that the gas phases reach the 1:2 ratio in the buffer tanks. For example, if the system is not operating and at atmospheric pressure, the electrolyte levels are equal and the oxygen gas volume is slightly smaller than one half of the hydrogen gas volume. Consequently if the system is switched on, the electrolyte level in the oxygen tank decreases and therefore the oxygen gas volume increases and the hydrogen gas volume decreases due to the electrolyte level rise in the hydrogen tank. Subsequently the gas volumes appear to reach the exact 1:2 ratio, because a pressure is built up to the control pressure without valve openings[3]. This finding is highly relevant to the second general finding as it prevents possible electrolyte overflows.

2. **Minimum required operating pressure of 5 bar**
   A second finding is that below $\sim 5\,\mathrm{bar}$, the level and pressures are not controllable with the opening times as described in Equation C.5 and this observation is attributed to the low pressure difference over the capillary tube. Occasionally, this lead to overflow of electrolyte on the oxygen side, because this capillary tube is less throttling in comparison to the hydrogen side. Concluding that a first limitation of the system has been found: a $5\,\mathrm{bar}$ minimum operating pressure[4].

Concluding this subsection with the contribution of the limitation to the operational envelope, the 80 % and 100 % RVOD lines can be seen in Figure 5.12 and are based on the corrected model.

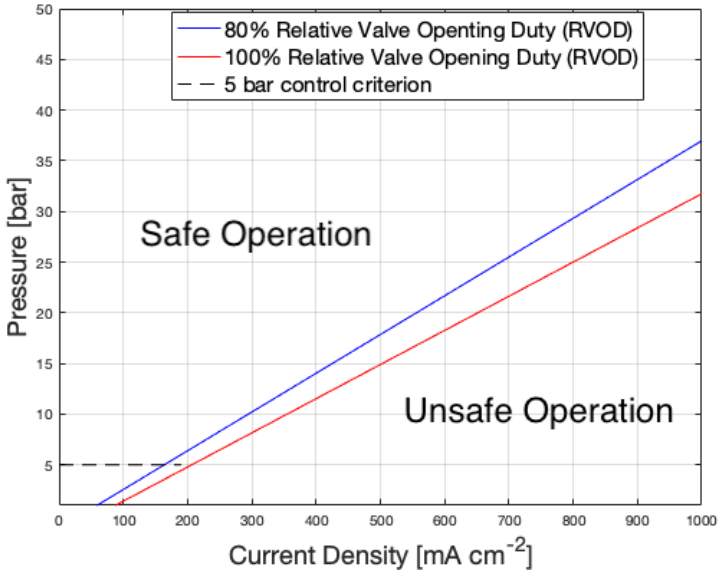

Figure 5.12: The 80 % and 100 % RVOD line based on the corrected model for the hydrogen purge valve cycle time.

[3]The buffer tanks' cross-sectional areas are close to the 1:2 ratio (1:2.20); assuming that the buffer tanks are exactly 50% filled with electrolyte, a level difference of $6.8\,\mathrm{mm}$ is required to reach the 1:2 ratio. This shows that gases reaching control pressure without purge valve openings is a reasonable scenario. However, the electrolyte volume in the system changes with respect to time as water is consumed; therefore a limited number of oxygen purge valve openings during pressure buildup have also been observed.

[4]Evidently, this limitation only applies to a system where the gasses flow through the capillary tubes for all operating conditions. A bypass valve without capillary tubes, as is included in the P& ID (Figure C.8 in section C.3), solves this limitation and is therefore recommended

5.1.2. Flow Stagnation

The flow stagnation experiments primarily made use of the characteristic temperature response as explained in subsection 4.1.2. However this temperature response appeared to be not decisive enough. A clear distinction between flow stagnation and a situation without flow stagnation can not be made unambiguously considering temperature signals only. Therefore, in addition to examining temperature profiles, a video camera was installed to visually detect flow stagnation. Examples of frames corresponding to (a) the end of a flow stagnation cycle, (b) normal operation (c) and flow stagnation are depicted in Figure 5.13.

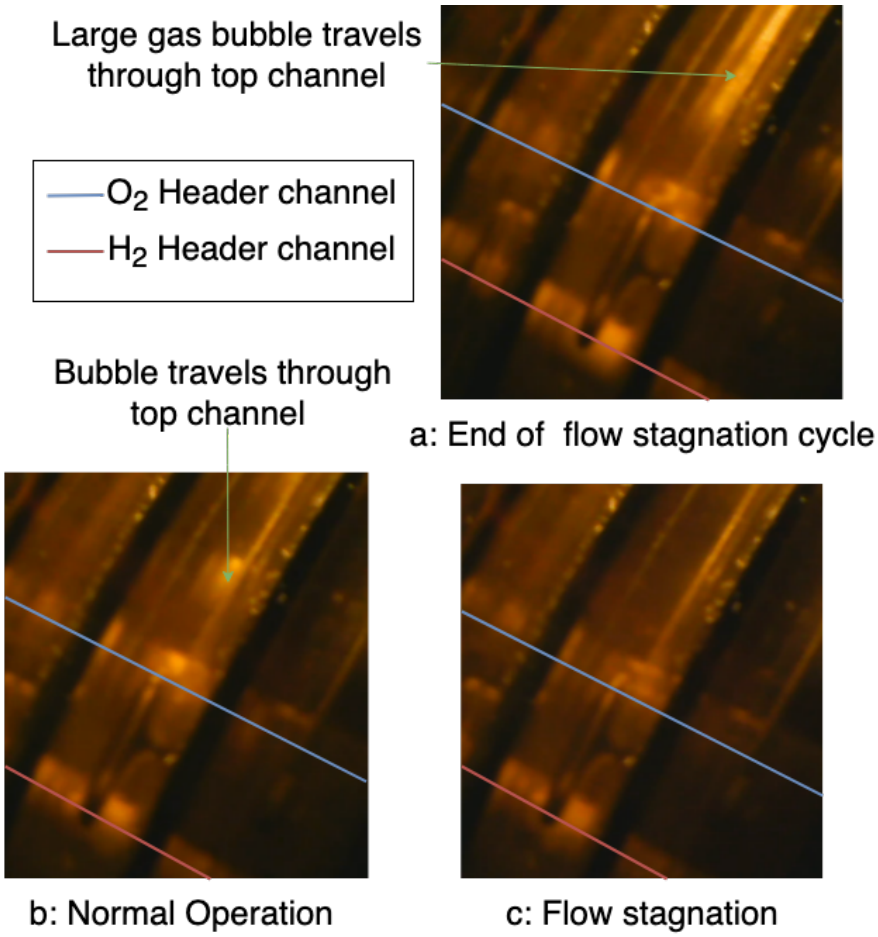

Figure 5.13: Images made by the camera to detect flow stagnation. Distinction between the gas phase and the liquid electrolyte is made by the colours: a relatively light colour corresponds to gas bubble and the relatively dark colour to the liquid electrolyte. The H_2 and O_2 header channels are indicated by the red and blues centre lines respectively.

The results of the flow stagnation experiments can be seen in Table 5.2, the variable indicated with X is introduced in subsection 4.1.2 and represents the gas production volume flow rate which is the driving force for the electrolyte circulation as explained in subsection C.3.2, paragraph titled ”Increasing electrolyte recirculation velocity”. The determined values for X show a distinction between operation with flow stagnation and without flow stagnation, which indicates the existence of the previously described critical volume flow rate: a minimum gas production per unit of time to avoid flow stagnation. Starting from the acquired data, the critical value for X is between $0.62\,\mathrm{A\,K\,bar^{-1}\,cm^{-2}}$ to $0.74\,\mathrm{A\,K\,bar^{-1}\,cm^{-2}}$. In comparison to the setup operated by Kleist, the critical volume flow rate has decreased significantly from 3.4 to $0.74\,\mathrm{A\,K\,bar^{-1}\,cm^{-2}}$. This decrease is expected and is attributed to the number of cells and the increased riser length as explained in subsection C.3.2, paragraph titled ”Increasing electrolyte recirculation velocity”. Evidently, a lower critical volume flow rate is considered to be beneficial in perspective of the operational flexibility.

However, the qualification of flow stagnation is inherently ambiguous. Specifically at low current densities, the gas bubbles travel in a discontinuous manner through the top channel. The flow is qualified

to be stagnated when no movement is observed in the header channel and top channels for over 15 seconds[5]. As described by Kleist, flow stagnation is a stochastic process and its determination is a matter of interpretation. To avoid flow stagnation with more certainty, operation at a significantly higher gas volume production rate is recommended. In addition to that, the results of the flow stagnation experiments consists of a limited data set and the aforementioned inherent ambiguity of qualifying a flow as stagnated. Therefore, it is recommended to both enlarge the data set by conducting experiments and to define a flow stagnation criterion that is less interpretation-dependent.

	P [bar]	CD [$\mathrm{mA\,cm^{-2}}$]	T [°C]	X [$\mathrm{A\,K\,bar^{-1}\,cm^{-2}}$]
Flow Stagnation:	30	50	31	0.5069
	50	100	30	0.6063
	50	100	35	0.6163
Not Flow Stagnation:	40	100	25	0.7454
	40	150	40	1.1743
	30	100	33	1.0205
	50	200	40	1.2526
	40	200	40	1.5657
	50	150	30	0.9094

Table 5.2: Results of the flow stagnation experiments. Operating conditions for two cases are distinguished: in the case a flow stagnation was observed and in cases where operating conditions to conditions corresponding to flow stagnation did not results in flow stagnation. The values for X ($X = \frac{CD \cdot T}{P}$) in the rightmost column suggest a critical volume flow rate as explained in subsection 4.1.2 and is found to be fin the range of $0.62\,\mathrm{A\,K\,bar^{-1}\,cm^{-2}}$ to $0.74\,\mathrm{A\,K\,bar^{-1}\,cm^{-2}}$

Flow stagnation and purge valve openings

During the flow stagnation experiments, it has been hypothesised that the control scheme possibly interferes with flow stagnation. For example, if the flow appears to stagnate and the oxygen purge valve opens, the flow stagnation is possibly resolved due to the sudden pressure drop and accompanying volume expansion associated with a valve opening. Consequently, if flow stagnation has not been observed in a given amount of time, but a purge valve is opened in that same period of time, one cannot directly discard flow stagnation under these operating conditions. However, the temperature profiles on the oxygen side reveal an additional insight about the relationship between flow stagnation and the oxygen purge valve openings.

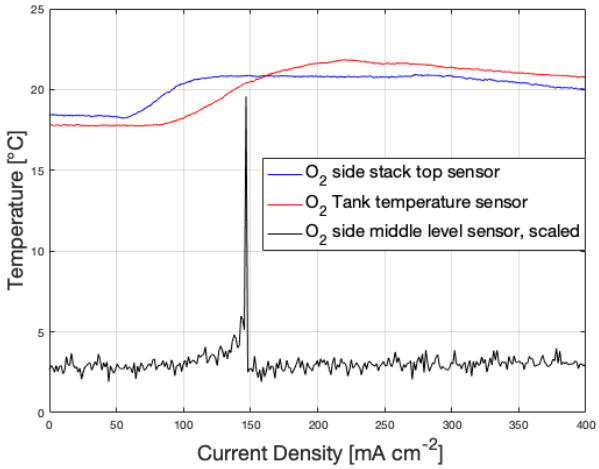

Figure 5.14: Temperature reading of the sensor placed on top of the stack at the oxygen outlet and the oxygen buffer tank, together with a scaled sensor reading of the middle oxygen level sensor which controls the oxygen purge valve openings; the peak value corresponds to a level sensor drought and subsequent oxygen valve opening.

In Figure 5.14, the temperatures of the oxygen tank and the oxygen side stack-top are plotted together

[5] 15 seconds is chosen in correspondence to the minimum observed flow stagnation duration of 17 s reported in the work of Kleist [39]

with a scaled version of the middle level sensor of the oxygen tank. The temperature increase of the stack-top temperature sensor is the characteristic ending of a flow stagnation, in which the warmed up liquid electrolyte flows past the sensor and as one can see, the increase is prior to the valve opening. Moreover, the flow stagnation is resolved first, such that the gas flows to the buffer tank resulting in the subsequent electrolyte level drop and level sensor drought, indicated by the spike of the black line in Figure 5.14. The level sensor drought subsequently results in the opening of the oxygen purge valve, implying that the opening did not interfere with the flow stagnation. This cascade of events is only applicable to the oxygen side, because the hydrogen purge valve is pressure controlled; so interference of the hydrogen purge valve opening with flow stagnation is possible and avoidance of openings during a stagnation cycle is necessary to acquire correct insight in flow stagnation conditions.

Concluding this subsection with the limitations flow stagnation have on the operational envelope. In Figure 5.15 three different flow stagnation lines can be seen, similar to subsection 4.1.2; except that in the new system flow stagnation at $90\,°\mathrm{C}$ is limiting below $87\,\mathrm{mA\,cm^{-2}}$ and in the previous system below $400\,\mathrm{mA\,cm^{-2}}$, which underlines the improvement on the operational flexibility.

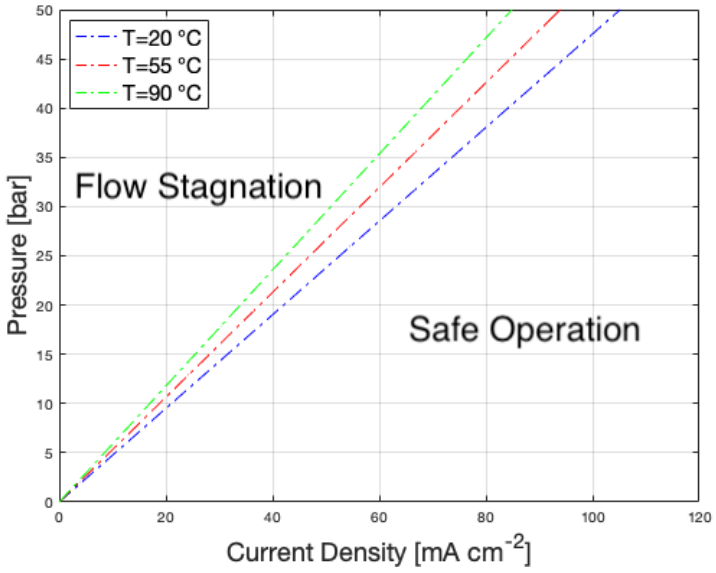

Figure 5.15: Flow stagnation limitations of the operational envelope for different steady state temperatures. At $50\,\mathrm{bar}$ and $90\,°\mathrm{C}$, flow stagnation limits from approximately below $87\,\mathrm{mA\,cm^{-2}}$.

5.1.3. Temperature Control

The installation of the PID-controlled cross-flow fans provides a certain degree of temperature control, as explained in subsection 4.1.3. To what extent the operational temperature is controllable and what relevant implications that reveals are central in this subsection, the most important outcomes and limitations of the temperature control experiments are summed up in Table 5.3 at the end of this subsection. In Figure 5.16, the locations of the eight temperature sensors are indicated and in Figure 5.17, an example of typical steady state temperature readings can be seen.
For all experiments T_5 (oxygen stack top sensor) is exceptionally lower than all other values, including the oxygen tank (T_2) and oxygen-side electrolyte bulk temperature after the finned tube heat exchanger (T_3). Furthermore, T_5 is closer to the heat generating stack and therefore, an explanation to the significant difference in measured temperatures can be found in sensor placement imperfections. For example, the T_5 sensor is badly taped or taped with isolation material in between the sensors and the riser wall, or an additional resistance in the sensor cable or connections introduces a significant offset.

Figure 5.16: Locations of the eight different temperature sensors in the system.

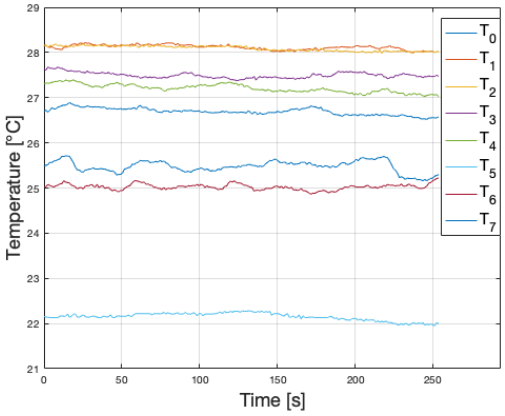

Figure 5.17: Typical temperature sensor reading at steady state. This measurement is taken at $50\,\mathrm{mA\,cm^{-2}}$ and $10\,\mathrm{bar}$, without operation of the fans.

Because the maximum allowable temperature is the limiting factor regarding temperature control, steady state temperatures stated throughout this subsection are the maximum measured values of all sensors. In Figure 5.18, the influence of cross flow fan operation can be inferred. At first glance, the decrease of temperatures after the fans have turned on (at a constant current density) directly show that implementation of the fans extents the maximum allowable operational current density. Approaching the $88\,°\mathrm{C}$ control temperature, the PID-control starts fan operation. The fluctuations of the fan power originate from the PID-control and the measured temperature responses fluctuate likewise. Another characteristic that can be seen in Figure 5.18 is that temperature differences between the tanks (T_0 & T_2) and the electrolyte bulk temperature measured after the heat exchangers (T_1 & T_3) significantly increase after the cross flow fans are turned on.
The highest allowable current densities that correspond to a steady state temperature of $90\,°\mathrm{C}$ at $50\,\mathrm{bar}$ are experimentally found to be approximately $450\,\mathrm{mA\,cm^{-2}}$ and $850\,\mathrm{mA\,cm^{-2}}$ corresponding to operation without cross flow fans and with 100% power cross flow fan operation, Figure 5.21 and 5.20 respectively. However, temperature sensor signals take time (order of magnitude: hours) to reach steady state and consequently the 'thermal history' of the signal plays a role. The ambient air conditions may vary between experiments and other practicalities (e.g. a different operator judges differently about steady state) limiting the certainty of the observed values. An example of a non-linear curve fit model is displayed in Figure 5.19, it used to estimate a steady state temperature based on transient data, acquired in a time restricted experiment.
The heat transfer and therefore the steady state temperatures depend to a large extent on surrounding conditions; temperature responses and therefore temperature control are inherently dependent on (possibly uncontrollable) surrounding factors. Consequently, applying this system under different conditions, e.g. in the Sahara dessert in stead of the lab facility, is expected to yield different temperature

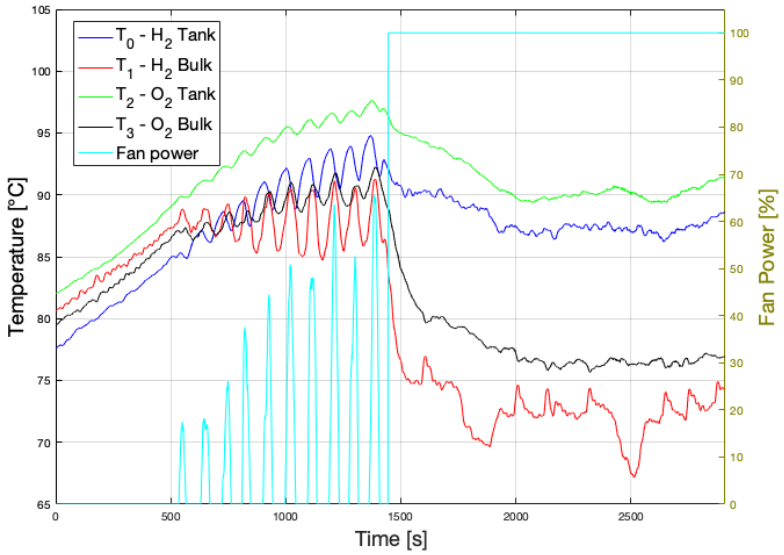

Figure 5.18: Temperature response to cross flow fan operation of the four highest measured temperatures. The PWM-signal to the cross flow fans corresponds to the light blue line and its values can be read on the right y-axis. Operating conditions: $600\,\mathrm{mA\,cm^{-2}}$, $50\,\mathrm{bar}$, control temperature $88\,°\mathrm{C}$. A decrease of temperature proportional to the fan power can be seen. Furthermore, an increase of temperature differences before (T_0 & T_2) and after the heat exchangers (T_1 & T_3) proportional to the fan power is visible.

responses. The experiments reported in this research were conducted with an ambient temperature of $16.5\,°\mathrm{C}$ to $17.5\,°\mathrm{C}$.

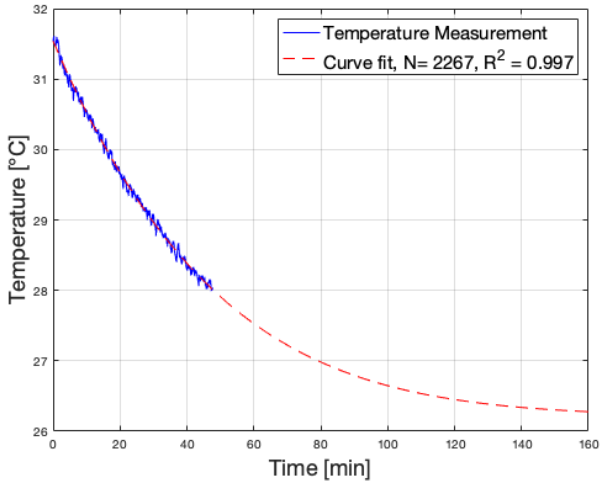

Figure 5.19: Steady state temperature estimation by making use of a transient temperature profile at constant current density and pressure. The plots exemplifies the relatively large timescale at which steady state is reached and it shows an estimation of the steady state temperature if transient data is provided only.
Curve fit was done using a non linear regression model in Mathworks' Matlab: $T(t) = a + b \cdot erfc((t-c)/d)$, with $a = 26.22, b = 54.53, c = -165.74, d = 141.49$. $R^2 = 0.997, N = 2267, RMSE = 0.0559$

Steady state temperatures at different current densities at constant pressure

In Figure 5.20, the thermal limitation of the system without cross flow fan operation is displayed. At constant temperature of right below $90\,°\mathrm{C}$, $450\,\mathrm{mA\,cm^{-2}}$ is the limiting current density for which fans are just not switched on by the PID-controller. For the system with cross flow fan operation, Figure 5.21, a maximum current density of approximately $850\,\mathrm{mA\,cm^{-2}}$ is reached. As one can see, if the current density is increased to $900\,\mathrm{mA\,cm^{-2}}$, temperature exceeds $90\,°\mathrm{C}$.
Testing at different current densities delivers ultimately the desired temperature control map, which has been introduced in subsection 4.1.3. The steady state temperatures for a system without cross flow fan operation can be seen in Figure 5.22 and in Figure 5.23 the steady state temperatures can be seen

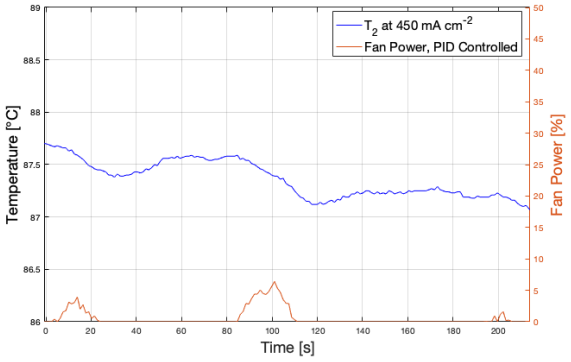

Figure 5.20: $90\,°C$ Temperature limit found at approximately $450\,\mathrm{mA\,cm^{-2}}$ without cooling from cross flow fans. Control pressure:$50\,\mathrm{bar}$.

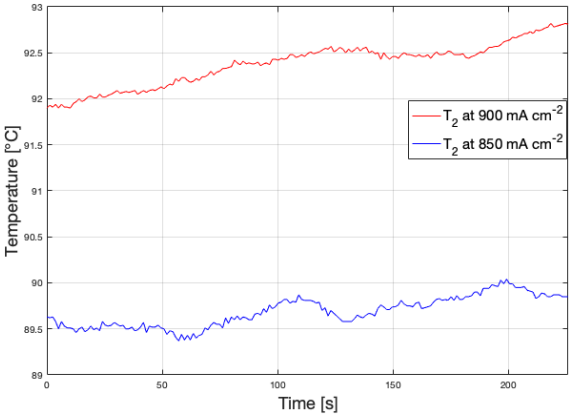

Figure 5.21: $90\,°C$ Temperature limit found at approximately $850\,\mathrm{mA\,cm^{-2}}$ with cross flow fans operating at maximum power. Control pressure:$50\,\mathrm{bar}$.

with the cross flow fans operating at 100% power; both operating pressures are $50\,\mathrm{bar}$. Evidently, the number of data points is limited and the linear relationship between current density and steady state temperature is an assumption. Given the aforementioned difficulties with measuring steady state temperatures, additional long duration experiments at intermediate current densities, are recommended. Such that the system analysis is based on more reliable data and the relationship between current density and steady state temperature can be described in more detail.

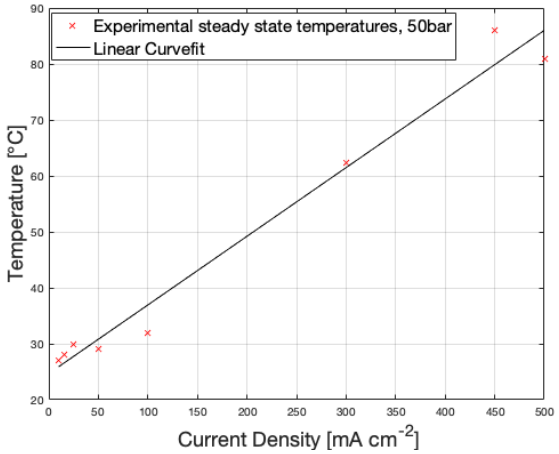

Figure 5.22: Experimentally found steady state temperatures at different current densities, operating pressure: $50\,\mathrm{bar}$. System without cross flow fans, the $90\,°C$ temperature limitation is found to be at approximately $450\,\mathrm{mA\,cm^{-2}}$

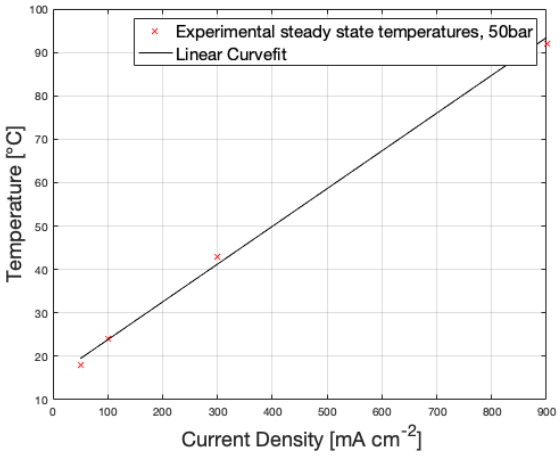

Figure 5.23: Experimentally found steady state temperatures at different current densities, operating pressure: $50\,\mathrm{bar}$. System with cross flow fans operating at 100% power, the $90\,°C$ temperature limitation is found to be at approximately $850\,\mathrm{mA\,cm^{-2}}$

Given the approximation of the minimum and maximum reachable temperatures, the experimental version of the qualitative temperature control map in subsection 4.1.3 is presented in Figure 5.24. The temperature is controllable within the ranges of possible temperatures and current densities corresponding to the green shaded area. The ratio of the green area and the area limited by external factors, in this situation: $16\,°C$ to $90\,°C$ [6] and $0\,\mathrm{mA\,cm^{-2}}$ to $1000\,\mathrm{mA\,cm^{-2}}$ [7], gives a measure of the degree of temperature control (DoTC) and the mathematical expression is given in Equation 5.1. Given the assumption of a linear relationship between the steady state temperatures and current density, Equation 5.1 can be solved by making use of the triangular and rectangular shapes in Figure 5.24. The degree of temperature control is determined to be 0.25. The degree of temperature control can be

[6] Temperature limitation of $16\,°C$ to $90\,°C$ is limited by the ambient air temperature and the material limitations respectively
[7] Current density is limited by the power supplies

used comparing operational flexibility to other electrolysis systems.

$$DoTC = \frac{\int_{i_{min}}^{i_{max}} [T_{max}(i) - T_{min}(i)]di}{(i_{max} - i_{min}) \cdot (T_{max,material} - T_{min,ambient})} = 0.25 \quad (5.1)$$

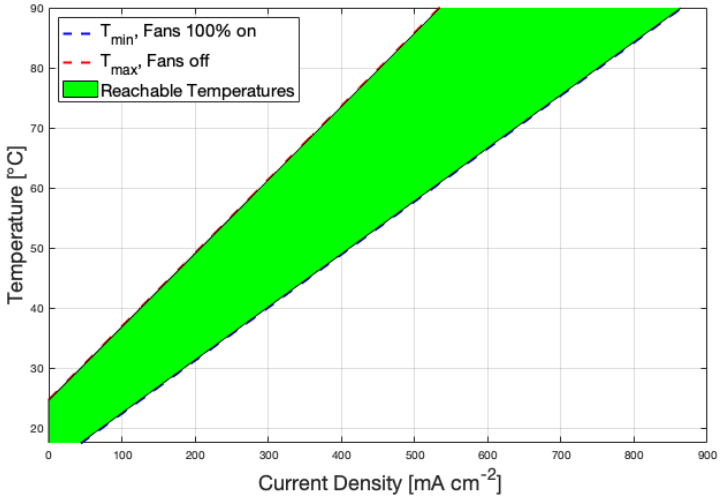

Figure 5.24: Temperature control map in which the reachable temperatures at every current density are shaded in green at $50\,\mathrm{bar}$. The lines indicated with T_{max} and T_{min} represent the steady state temperature response with 0% and 100% cross flow fan power respectively and are based on experimental data which can be seen in Figure 5.22 and Figure 5.23.

Steady State Temperatures at different pressures at constant current density

In principle, the cooling capacity depends on the electrolyte flow velocity, which in turn depends on the buoyancy driving force which in turn depends on the gas volume in the riser which in turn depends on the pressure. So in principle, a higher pressure is expected to result in a higher steady state temperature at a given current density an d heat generation. The voltages are reported together with the steady state temperatures as the heat generation possibly differs with pressures.

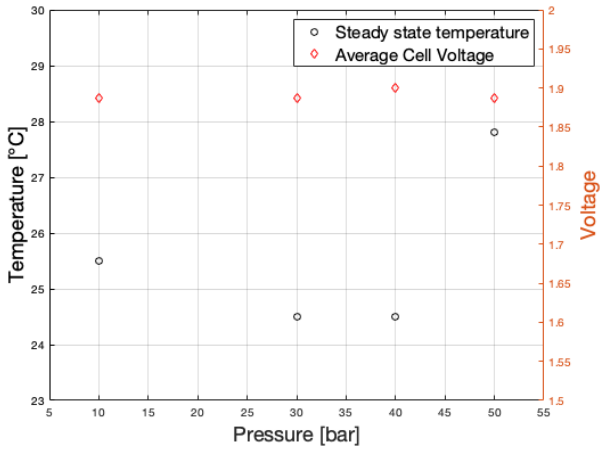

Figure 5.25: Steady state temperatures at different operating pressures, at $50\,\mathrm{mA\,cm^{-2}}$. Based on the results of this experiment, no general conclusion can be drawn regarding the possible pressure dependency of the temperature control. At higher current densities, overvoltage and accompanying heat generation due to bubble resistance plays a more significant role and temperature control is possibly pressure dependent.

Results of the pressure dependency tests can be seen in Figure 5.25, the experiments were conducted at $50\,\mathrm{mA\,cm^{-2}}$. Experiments in the $850\,\mathrm{mA\,cm^{-2}}$ range were not conducted, as the RVOD approached the 80-100% regime which is deemed unsafe to operate beyond, see subsection 5.1.1.

The average cell voltage, indicated by the red diamonds, does not show a pressure dependence. The steady state temperatures appear to be independent from pressure, except from the region $40\,\mathrm{bar}$ to $50\,\mathrm{bar}$ where an increase of approximately $3\,^{\circ}\mathrm{C}$ is observed. This could be explained by the possibility that the aforementioned reasoning plays a significant role at pressures exceeding a certain threshold. A different, more plausible explanation is that the electrolyte circulation velocity and therefore the cooling capacity is influenced by flow stagnation in this experiment, as the relatively low current density in combination with the low temperatures and high pressure triggers flow stagnation, see subsection 5.1.2. If flow stagnation is present, the time-averaged electrolyte velocity and consequently the cooling capacity is lower in comparison to the cooling capacity during normal operation.
Besides, at higher current densities, overvoltage and accompanying heat generation due to bubble resistance plays a more significant role and temperature control is possibly pressure dependent.
Concluding that the conducted experiments on the pressure dependency of temperature control or cell voltages do not reveal a relationship at relatively low current densities. Further research is recommended to investigate the pressure dependence of the temperature control and voltages at high current densities and at lower current densities but without interference of different phenomena such as flow stagnation.

Electrolyte mass flow calculations

The mass flow rates of the electrolyte can be determined by via an energy balance, presented in Equation B.1, which was used to design the finned tube heat exchangers. In section B.1, the flow thermal capacity (described by Mills et al.[52]) is introduced and an estimation of 98% of the heat transfer is attributed to the electrolyte. Assuming heat transfer by the electrolyte only, Equation B.1 simplifies to:

$$\dot{Q}_{Stack} = \Delta T \cdot \dot{m}_{el} = (V_{Stack} - 1.48 \cdot N) \cdot I \tag{5.2}$$

Rearranging Equation 5.2 gives the electrolyte mass flow as function of measured values: Voltage, current and the temperature difference over the stack. An important notion is in place: due to the aforementioned T_5 sensor failure, this approach is not applied on the oxygen side. As the gas production rate is exactly half the hydrogen production, an estimation of the electrolyte mass flow on the oxygen side can be done[8]. In Figure 5.26 and Figure 5.27 the approximate electrolyte mass flows can be seen in a situation with 0% and 100% cross flow fan operation respectively.

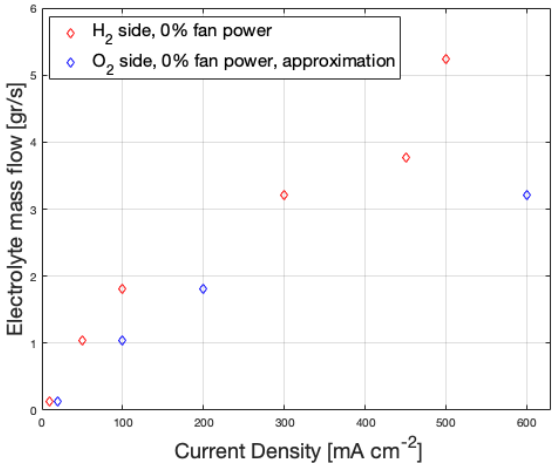

Figure 5.26: Electrolyte mass flow rates determined as a function of voltage, current and temperature difference between the inlet and outlet of the stack on the hydrogen side, Equation 5.2. Experiments without cross flow fan operation, $450\,\mathrm{mA\,cm^{-2}}$ was temperature limited.

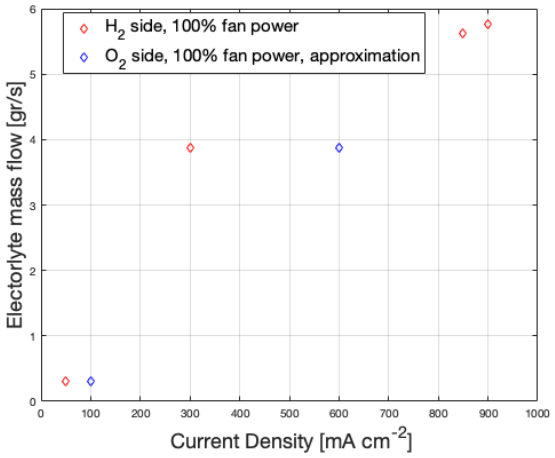

Figure 5.27: Electrolyte mass flow rates determined as a function of voltage, current and temperature difference between the inlet and outlet of the stack on the hydrogen side, Equation 5.2. Experiments with cross flow fan operation at 100%, $850\,\mathrm{mA\,cm^{-2}}$ was temperature limited.

The heat exchanger design, section B.1, determined a required electrolyte mass flow of approximately $4.8\,\mathrm{g\,s^{-1}}$.The $4.8\,\mathrm{g\,s^{-1}}$ is in the ball park of the experimentally found values presented in Figure 5.27.

[8]With more data points at intermediate current densities, a relationship between electrolyte mass flow and gas production rate can be made. Additionally, the electrolyte mass flow rate on the oxygen side can be determined.
For the experimental results as presented, the electrolyte mass flow rate on the oxygen side are approximated by the electrolyte mass flow rate on the hydrogen side at double current density.

Analogously to the pressure dependency and temperature control experiments, more long duration experiments at intermediate current densities are recommended to describe the relationship between current density and electrolyte mass flow rate in detail.

The contribution to the operational envelope concludes this subsection. The $850\,\mathrm{mA\,cm^{-2}}$ current density limitation is experimentally found in the temperature control experiments. Additionally, the steady state temperatures did not show a relationship with pressure independently from other phenomena (e.g. interference of flow stagnation) and therefore the temperature control line in the operational envelope is vertically oriented and located at $850\,\mathrm{mA\,cm^{-2}}$. As mentioned before, this is not directly tested and therefore is ultimately assumed. The outcomes and limitations to the temperature control experiments are summed up in Table 5.3.

General Steady State Temperature Measurements		
Outcomes	Limitation	Figures
450 & $850\,\mathrm{mA\,cm^{-2}}$ CD limits	Dependency on surrounding T	5.16,5.17,5.18.
	Timescale to reach steady state temperatures	5.19,5.20,5.21
	Practicalities, e.g. different operators	
	Temperature sensor accuracy	
Steady State Temperatures at different current densities at constant pressure		
Outcomes	Limitation	Figures
Reachable T's for different CD's	Data set size	5.22,5.23
Temperature Control Map	A: a linear $T - CD$-relationship	5.24
DoTC = 0.25	Experiments only at $50\,\mathrm{bar}$	
Steady state temperatures at different pressures at constant current density		
Outcomes	Limitation	Figures
No relationship has been found	Tested only at $50\,\mathrm{mA\,cm^{-2}}$	5.25
	Flow stagnation influenced T measurement	
Electrolyte mass flow calculations		
Outcomes	Limitation	Figures
Mass flow at current densities	Limited data set	5.26,5.27
	A: constant thermoneutral voltage	
	A: electrolyte heat transfer only	
	A: zero heat loss through the stack walls	
	Mass flow on O_2 side is based on H_2 mass flows only	
	Limited voltage & current measurement accuracy	

Table 5.3: Table summarising the most important outcomes and limitations of the temperature control experiments and presented data. Used abbreviations: CD is current density, T is temperature and A stands for assumption.

5.1.4. Crossover

Operational flexibility of ZEF's previous electrolysis setup was limited by hydrogen crossover to large extent and by the lack of cooling for the other part. An improvement with respect to crossover was a central theme in the design of the new system, reported in section C.3. Moreover, the capillary tubes, large diameter downcomer and midplate stack are designed to mitigate (H_2-)crossover among other things. Consequently, the hydrogen crossover performance of the new system is considered to be a key parameter to validate both the new system design and the parasitic hydrogen production hypothesis described in subsection C.3.1. As explained in subsection 4.1.4, crossover experiments have an explorative nature, because effects of the different system adjustments have not been modelled quantitatively. Moreover, in the same subsection it has been explained that the crossover experiments were guided by the outcomes themselves, searching for the 50% LEL line in the operational envelope. Results of the steady state hydrogen crossover tests can be seen in Figure 5.28 and 5.29.

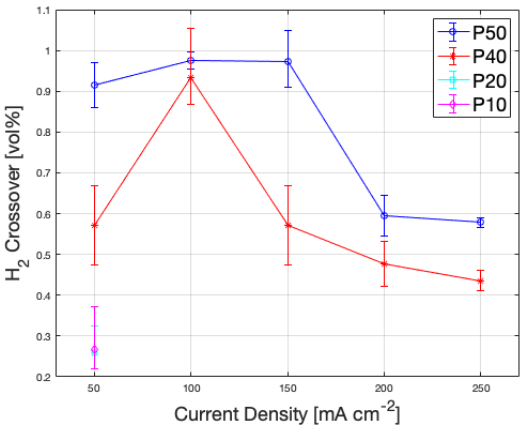

Figure 5.28: H_2-Crossover of the new AEC system at different current densities for different pressures. Values are averaged over multiple samples.

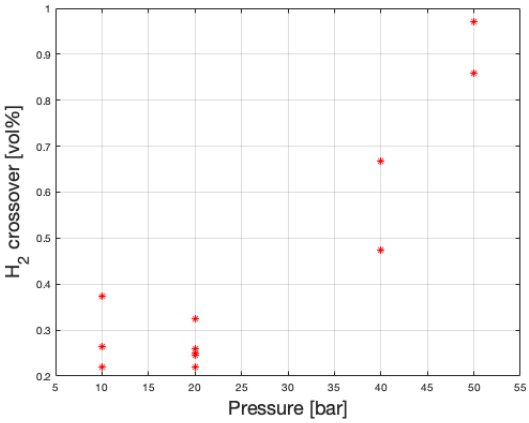

Figure 5.29: H_2-Crossover at different pressures at a current density of $50\,\mathrm{mA\,cm^{-2}}$

In Figure 5.29, the acquired data is plotted directly and as one can see, the deviation in data points is relatively large. This could be explained by several phenomena. Firstly, the gas phase above the liquid electrolyte has a certain timescale to reach steady state analogously to temperature. If a sample is taken before steady state is reached, the data is disturbed by the lower or higher hydrogen content from the past. Besides, the gas is analysed by manually taking samples and subsequent analysis using a gas chromatograph (GC) and therefore inherently dependent on practicalities influencing the measurements e.g. dead volume in the syringes and the leak tightness of the couplings of the syringes. Also the exact temperature, electrolyte concentration and pressure the sample was taken at in principle deviate over time has and have impact on the obtained crossover value.
Secondly, time between sampling and analysis in the GC is demonstrated to have a significant impact on the obtained crossover value [9]; time between sampling and analysis returns effectively an underestimation of the H_2-crossover.

Starting from the obtained values in the presented figures, several noteworthy aspects can be distinguished. First and foremost, all the obtained values are significantly below the 50% LEL (2.7% at $50\,\mathrm{bar and 50\,°C}$) and therefore operation in this entire regime can be deemed safe[10]. Concluding that the system adjustments provide the desired improvement of operational flexibility by means of a hydrogen crossover decrease.
Secondly, crossover increases with increasing system pressure, which is an expected consequence of a higher dissolved hydrogen content according to Henry's law as described in subsection 2.4.3.

[9] To exemplify the impact of time between sampling and analysis, two samples with identical syringes have been taken directly after one another at steady state operation. The first was directly analysed and yielded a $0.853\ vol\%\ H_2$ content, the second was analysed after $23.5\,\mathrm{h}$ and yielded $0.513\ vol\%$, a decrease of 40%.

[10] An additional experiment has been conducted at $50\,\mathrm{bar}$, $20\,°\mathrm{C}$ and the minimum possible current density of $10\,\mathrm{mA\,cm^{-2}}$, which is limited by the power supplies. A maximum value of 1.8 $vol\%$ was observed, notably below the 50% LEL of 2.7 $vol\%$ at $50\,\mathrm{bar}$.

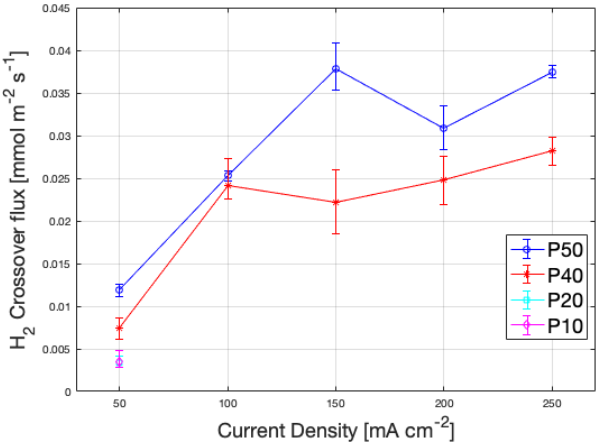

Figure 5.30: Hydrogen crossover expressed as an absolute molar flux per square meter versus current density at different pressures. Conversion of the volume percentage, as depicted in Figure 5.28 are converted to molar flows using Equation 5.3, taken from the work of Trinke et al. [86].

Another noteworthy characteristic, is that the H_2-crossover is generally decreasing with current density, with an exception for low current densities, $50\,\mathrm{mA\,cm^{-2}}$ to $100\,\mathrm{mA\,cm^{-2}}$. The trend of an increase at relatively low current densities, reaching a plateau, and a subsequent decrease at higher current densities is also found in literature, e.g. in the work of Trinke et al [86, 13]. Focusing on the relatively high current densities first, the decrease of crossover with increasing current density is explained by the increase of produced oxygen with increasing current density, which decreases the fraction of hydrogen crossover (which is approximately constant in the high current density regime at a given pressure).

To understand the crossover increase at low current densities, the absolute molar flux of hydrogen crossover is calculated and depicted in Figure 5.30. The molar flux, expressed in $\mathrm{mmol\,m^{-2}\,s^{-1}}$ is determined via Equation 5.3, which converts the measured crossover as volume percentage (denoted Φ_{H_2}, expressed as a fraction) in to a molar flux by making use of the current density (CD, units: $\mathrm{mA\,m^{-2}}$), the Faraday constant ($F = 96\,485\,\mathrm{C\,mol^{-1}}$) and the assumption that both oxygen and hydrogen have the same molar volume. The equation is found in the work of Trinke et al.[86] and is applicable to cells with equal separator and electrode areas.

$$\dot{N}_{H_2} = \frac{CD}{4 \cdot F} \cdot \frac{\Phi_{H2}}{1 - \Phi_{H2}} \tag{5.3}$$

The trend in Figure 5.30 is approximately similar to what is found in the work of Trinke et al.: for relatively high current densities, the molar flux neither decreases nor increases significantly with current density. On the other hand, for low current densities the molar flux increases with increasing current density. The latter could explain the increase of crossover expressed as a volume percentage in Figure 5.28 with increasing current density in the low current density regime. If the molar H_2 crossover flux increases relatively more than the production of oxygen, the volume percentage of H_2 increases with increasing current density.
Given the reasoning above, the underlying question is rephrased: Why does the molar H_2 flux increase with current density in the low current density regime? An explanation can be found in the work of Vogt et al.[92] and Trinke et al.[86]. The explanation makes use of the term *gas evolution efficiency*, which is the ratio of the product gas adhered in gas bubbles to the total generated product gas at the electrode. At low current densities, the gas evolution efficiency is found to be relatively low: a relatively large portion of the produced hydrogen is transported in dissolved form either to the electrolyte bulk or to the other side of the separator as crossover. An increase of current density results in a higher dissolved hydrogen content and therefore increase of crossover. This holds up to the point where the (local) hydrogen concentration is high enough for bubble nucleation, consequently the gas evolution efficiency increases. The gas evolution efficiency typically has the form: $\eta = a \cdot i^b$ with $a, b \in [0, 1]$, indicating the strong relationship with current density, specifically at low current densities.

Benchmarks

It has been concluded that for the new system, hydrogen crossovers are below the 50% LEL and therefore the operational envelope is not limited by crossover. In Figure 5.31, the obtained value are compared to the previous electrolysis setup, the plotted data can be found in the work of Mulder [53]. The significant shift of the lines downwards is attributed to the removal of the parasitic hydrogen production by implementation of the midplate stack.

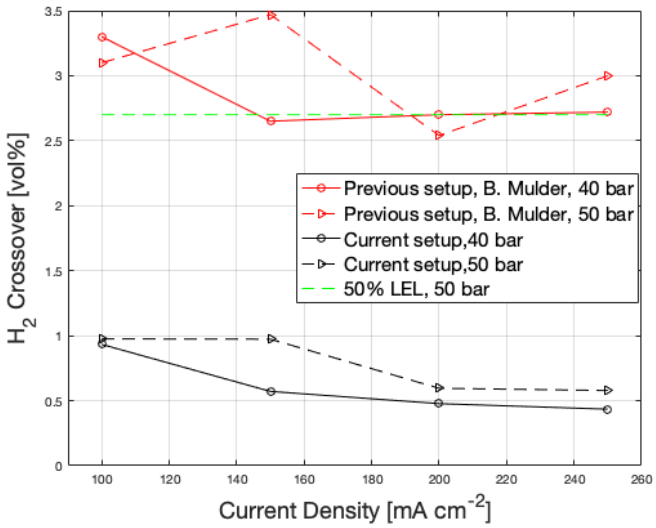

Figure 5.31: Hydrogen crossover at different current densities and pressures,comparison between the current system (black) and ZEF's previous setup (red), values based on the work of Mulder [53].

However a comparison with alkaline electrolysis systems in literature has not been included yet. In Figure 5.32, the $50\,\mathrm{bar}$ line is plotted together with $1\,\mathrm{bar}$ systems described in the work of Haug et al. [25] and with $1\,\mathrm{bar}$ and $20\,\mathrm{bar}$ systems described in the works of Trinke et al.[86] and Brauns et al.[13]. It can be seen that the observed crossovers of the obtained system at $50\,\mathrm{bar}$ are comparable to systems operating at atmospheric pressures with mixed cycles. In the bottom left corner, it ban be seen that the obtained system at $10\,\mathrm{bar}$ and $50\,\mathrm{mA\,cm^{-2}}$ has only a slightly higher crossover in comparison to an atmospheric system with separated electrolyte cycles. Given the tenfold pressure increase, the results suggests that ZEF's electrolysis system is more than competitive with respect to crossover performance.

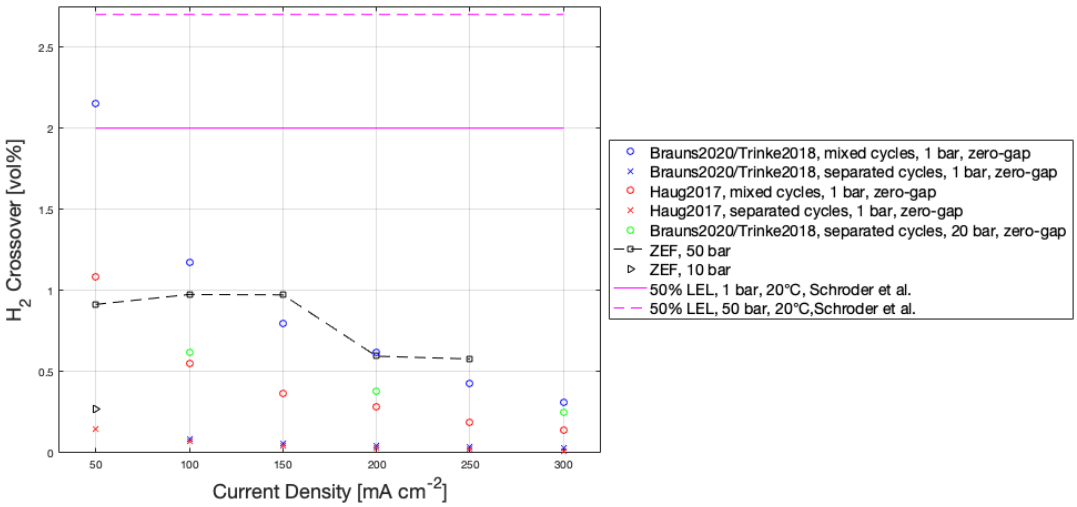

Figure 5.32: Hydrogen crossover characteristic compared to $1\,\mathrm{bar}$ and $20\,\mathrm{bar}$ alkaline electrolysis systems found in literature: Brauns et al.[13], Trinke et al[86] and Haug et al.[25]

An inherent system property is that the number of valve openings at a given pressure is proportional to

the gas production rate, previously reported by Mulder [53]. The gas production rate depends on the current density, pressure and temperature ($\dot{V}_{H_2} \sim \frac{i \cdot T}{P}$) as described in Equation 4.1. Consequently both a pressure decrease and a current density increase result in a higher gas volume production rate and with that an increased valve opening frequency resulting in higher convectional crossover. Concluding that both the decrease of crossover with increasing current density and the increase of crossover with increasing of pressure that is observed in literature is expected to be mitigated in the acquired system, which can be observed in the presented figures, 5.32 and 5.28.

Concluding this subsection with the relevant notion of the difference between a zero gap and non-zero gap design. The consulted literature consistently presented zero gap designs, a cell in which the distance between electrodes and separator is minimised. This design is considered to be superior to gap designs in terms of resistance losses and efficiency. However, a zero gap design is expected to have larger crossovers through the separator due to a decrease in distance between the (super) saturated zones across the separator. Consequently, significantly less crossovers in comparison to systems found in the consulted literature is expected.

Overnight diffusion

If the electrolysis is put in to the context of ZEF's solar powered methanol synthesis plant, periods without production are conceivable e.g. during nighttime. During a period without production, diffusion takes place and the two gas volumes start to equilibriate over time, resulting in the 'Spike after start-up' as observed by Mulder [53] and predicted by Schwarze [75]. The overnight diffusion experiments, intended to quantify the amount of overnight diffusion are repeated for the new system, to complete the perspective on operational flexibility in terms of crossover. The results are depicted below. In Figure 5.33, crossover results are shown of the start-up after leaving the system under a pressure of $1.3\,\mathrm{bar}$ for over a night, approximately $16\,\mathrm{h}$, the 50% LEL is exceeded and therefore an overnight pressure of $1.3\,\mathrm{bar}$ is considered to be too low. In Figure 5.34, crossover results are shown of the start-up after leaving the system under a pressure of $49.5\,\mathrm{bar}$, the 50% LEL is not reached and so leaving pressure on the system is considered to be favourable in comparison to atmospheric conditions. Apart from the safety aspect, a second benefit is that the system requires less time to start up to continue at $50\,\mathrm{bar}$ operation. The crossover peak value due to overnight diffusion decreases with increasing

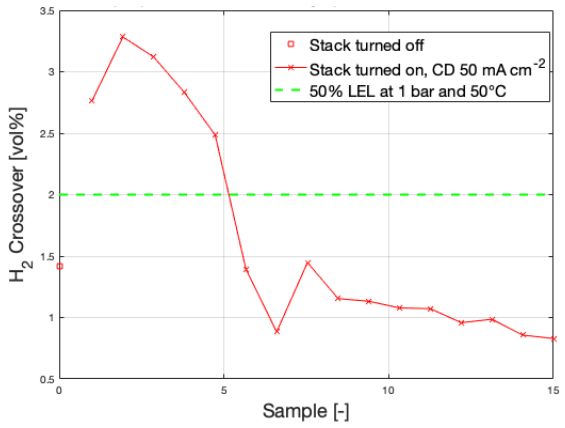

Figure 5.33: Hydrogen crossover during a start-up experiment, overnight pressure: $1.3\,\mathrm{bar}$. The stack was turned on at a current density of $50\,\mathrm{mA\,cm^{-2}}$. The peak exceeds the 50% LEL.

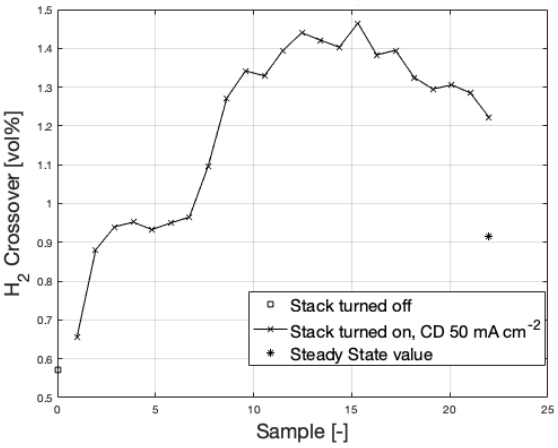

Figure 5.34: Hydrogen crossover during a start-up experiment, overnight pressure: $50\,\mathrm{bar}$. The stack was turned on at a current density of $50\,\mathrm{mA\,cm^{-2}}$. All values are below the 50% LEL

pressure, this trend was also observed in the work of Mulder [53] and is attributed to the increased number of oxygen molecules in the gas phase. This results in a lower relative hydrogen content in gas phase, once the system is turned on and the dissolved hydrogen in the electrolyte in the stack starts to transfer to the oxygen gas phase over time. Leaving the system under a $3\,\mathrm{bar}$ pressure for over a weekend, approximately $64\,\mathrm{h}$ later, resulted in a maximum observed concentration of 6 $vol\%$, not only exceeding the 50% LEL but also the 100% LEL. The effect of time on the measured crossover is

illustrated by this experiment of which the results can be seen in Figure 5.35.

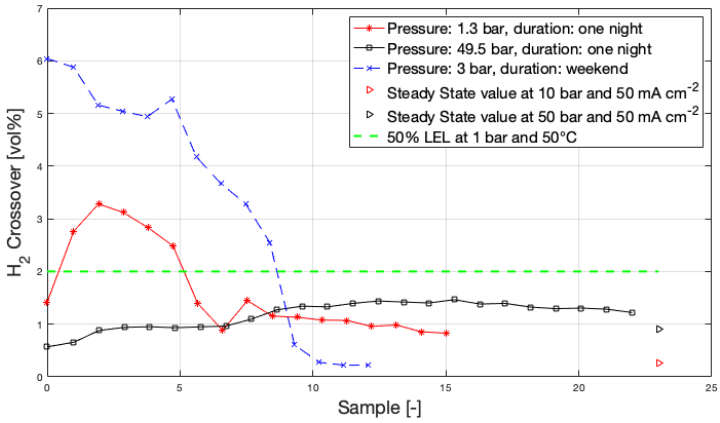

Figure 5.35: Effect of time on overnight crossovers. Comparison of observed crossovers during start-up between two experiments ($1.3\,\mathrm{bar}$ and $50\,\mathrm{bar}$ overnight pressure) with a period of $16\,\mathrm{h}$ without production and an a period of $64\,\mathrm{h}$ without production (at overnight pressure of $3\,\mathrm{bar}$. Start-up current densities are $50\,\mathrm{mA\,cm^{-2}}$

Hydrogen crossover versus temperature

In addition to the experiments described above, H_2-crossover is tested at different temperatures at constant current density and pressure in an attempt to investigate to what extent the system can be considered with separated or mixed electrolyte cycles as described in the work of Haug et al. [25]. As this experiment yielded inconclusive results, the results and background information can found in an appendix, section A.1.

Oxygen crossover

The experiments and analysis regarding the oxygen crossover are less extensive in comparison to the hydrogen crossover. The oxygen crossover in the previous electrolysis system has been described in detail by Mulder [53]. In his work, oxygen crossover is concluded to not be limiting in ZEF's electrolysis setup. Hydrogen crossover is reported to be limiting in literature as well [38, 74, 86, 99], this can be attributed to the higher absolute molar crossover flow due to a higher H_2 diffusion coefficient and a equal or higher H_2 solubility (depending on electrolyte molarity). The aforementioned, in combination with testing the parasitic hydrogen production hypothesis prioritised the investigation on hydrogen crossover, rather than oxygen crossover. No significant changes with respect to oxygen crossover are expected. As can be seen in Figure 5.36, the steady state values are below the 50 % UEL for all current

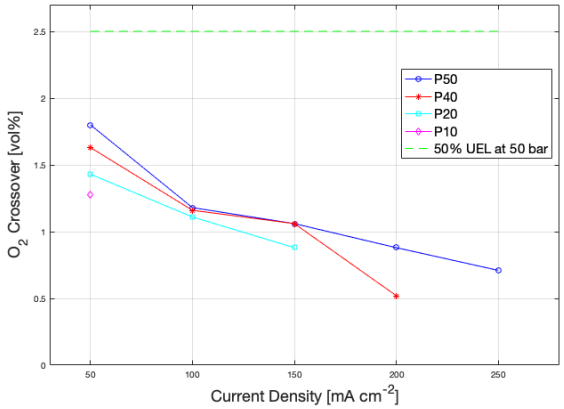

Figure 5.36: Steady state O_2 crossover versus current density for different pressures.

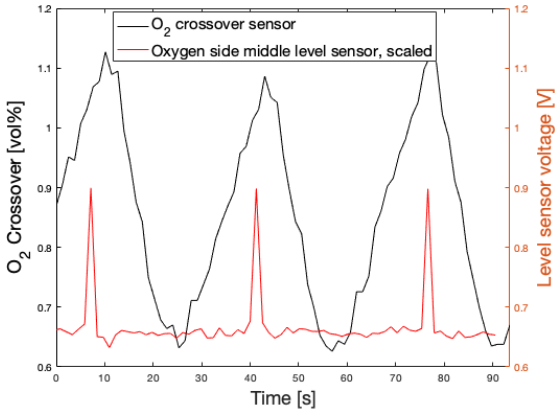

Figure 5.37: A typical O_2-crossover sensor reading (black) and a scaled version of the middle level sensor reading throughout time (red). The O_2-crossover sensor reading drops right after an oxygen purge, which corresponds to a spike in the red curve. The sharp rise of the O_2-crossover sensor reading indicates a leaking sensor housing.

densities and all pressures. A significant increase in comparison to the previous system is observed, as can bee seen in Table 5.4. However, the data is considered to be distorted by a leaking sensor housing. The sensor housing used in the work of Mulder has shown to produce steady O_2-crossover value for $\sim 150\,\mathrm{s}$ after a purge valve (figure 4.14 in [53]). In addition to that, Mulder showed that leak-tightness of the sensor housing is paramount to stable and reliable O_2-crossover sensor readings and is rather challenging to obtain [53]. As can be seen in Figure 5.37, the sensor readings drop to the

	Current Density [$\mathrm{mA\,cm^{-2}}$]			
	100	150	200	250
$50\,\mathrm{bar}$	0.32	0.39	0.33	0.34
$40\,\mathrm{bar}$	0.33	0.39	0.32	0.32
$20\,\mathrm{bar}$	0.24	0.27		

Table 5.4: O_2-Crossover values of ZEF's previous electrolysis setup. Values obtained from the work of Mulder [53]. Not all values are at steady state temperature, because the previous system did not have temperature control.

minimum value in a relatively short time, this corresponds to the hydrogen product gas entering the sensor housing. Directly after reaching the minimum value, the senor reading rapidly increases again indicating a leak of ambient air with 20.9 $vol\%$ O_2 in to the sensor housing. The local minimum O_2-crossover value is considered to represent the O_2-crossover in the hydrogen gas, but is likely to be an overestimation. However, as a constant value is not obtained over a period of time, the question remains about how reliable the obtained values are. As mentioned before, the probably overestimated values are nevertheless below the 50% UEL. Therefore the O_2-crossover is not considered to be safety risk, but it is highly recommended to improve the sensor housing and repeat the experiments to obtain reliable data and insight in the O_2-crossover of the acquired system, as the described experiments are considered inconclusive.

5.1.5. Conclusion

All the experiments, limitations and impact on the operational envelope being described, the contributions of the limitations to the operational envelope are summed up in the experimentally found operational envelope, which can be seen in Figure 5.38.

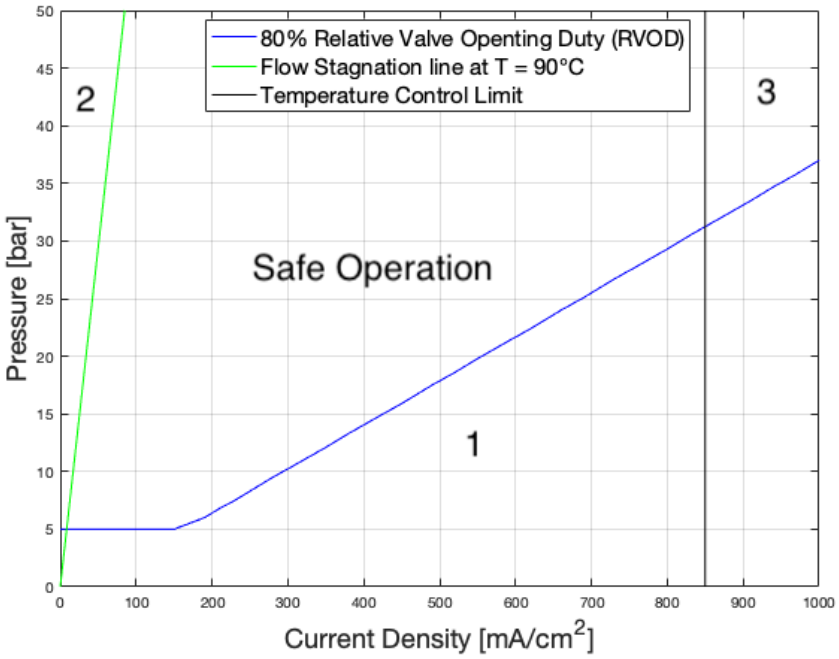

Figure 5.38: Operational envelope as determined through experiments, this version corresponds to operation at $90\,^{\circ}\mathrm{C}$. The current density-pressure characteristics of three limitations are found experimentally:

1. The 80% RVOD limitation is based on the corrected model involving the capillary tubes, subsection 5.1.1.
2. The flow stagnation limitation is experiments in which flow stagnation has been determined by use of a video camera and temperature profiles. The parameter X which represents the critical volume flow rate is found to be in the range of $0.62\,\mathrm{A\,K\,bar^{-1}}$ to $0.74\,\mathrm{A\,K\,bar^{-1}}$, subsection 5.1.2.
3. The temperature control limitation is based on the experimentally found $850\,\mathrm{mA\,cm^{-2}}$ at which the temperature reached $90\,^{\circ}\mathrm{C}$ with the fans blowing at maximum power. The pressure dependence of the temperature has not been found in the experiments, although this could not be tested at $850\,\mathrm{mA\,cm^{-2}}$, subsection 5.1.3.
4. The experiments of which the results and analysis are reported in subsection 5.1.4 show that crossover does not have an operational limitation on the system.

The limitations govern to what extent the electrolysis system can be operated under different operating conditions. A relative flexible system has a relative large number of safe operating points in comparison to all possible operating points to which the system is designed, resulting in a relative large area marked with 'Safe Operation' in the operational envelope. Therefore the *Degree of Flexibility* is defined as the ratio of the safe operating points to all possible operating points, given the design criteria. All possible operating points for which the syste is designed: CD $0\,\mathrm{mA\,cm^{-2}}$ to $1000\,\mathrm{mA\,cm^{-2}}$, pressure $1\,\mathrm{bar}$ to $50\,\mathrm{bar}$ and temperature $15\,^{\circ}\mathrm{C}$ to $90\,^{\circ}\mathrm{C}$. At $90\,^{\circ}\mathrm{C}$ the degree of flexibility is determined to be 0.5269. In principle, the degree of flexibility can be used to compare electrolysis systems, together with power consumption, costs, purity, efficiency and hydrogen yield for example. In a scenario of using an electrolysis system in combination with intermittent energy sources, the degree of flexibility is possibly a relevant parameter to take into consideration if operation under multiple conditions is desired. The idea of defining a degree of flexibility is not necessarily limited to safe and unsafe operation, but can be extended to for example efficiencies or costs. The general idea is to map the relative number of operating points satisfying a certain criterion, in this thesis: safe operation, to the operating range for which the system is originally designed.

5.2. General Characteristics & Unexpected Findings

As described in subsection 2.1.3, different efficiencies are used to describe the performance of electrolysis systems. The most commonly used are the Faradaic efficiency, which uses the equilibrium cell potential ($1.23\,\mathrm{V}$ under standard conditions), see Equation 2.8; another commonly used efficiency is the thermal efficiency, Equation 2.9 which is based on the total energy demand (heat + electricity) of the reaction and uses the thermal neutral voltage ($1.48\,\mathrm{V}$ under standard conditions). The thermal neutral voltage does not have a strong temperature dependence as the equilibrium potential, making it a suitable efficiency measure. Both experimentally found efficiencies at $50\,\mathrm{bar}$ at two different temperatures are depicted in Figure 5.39. The average cell voltages are also commonly used to indicate electrolysis performance, as this avoids using a particular definition of an efficiency, the IV-curve of the acquired system operating at $50\,\mathrm{bar}$ for two different temperatures can be seen in Figure 5.40.

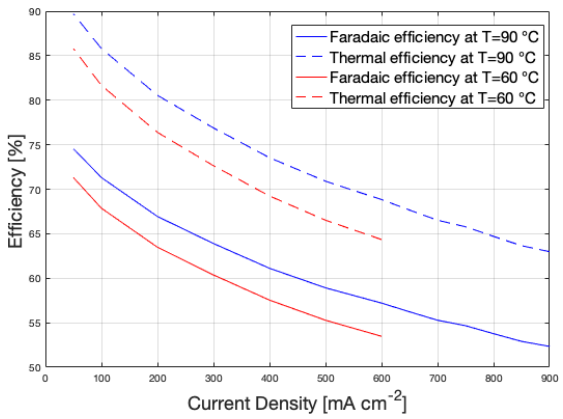

Figure 5.39: Experimentally found faradaic and thermal efficiencies versus current density at $90\,^{\circ}\mathrm{C}$ (blue) and $60\,^{\circ}\mathrm{C}$ (red) at $50\,\mathrm{bar}$. The $60\,^{\circ}\mathrm{C}$ line is limited at high current densities by the limited temperature control .

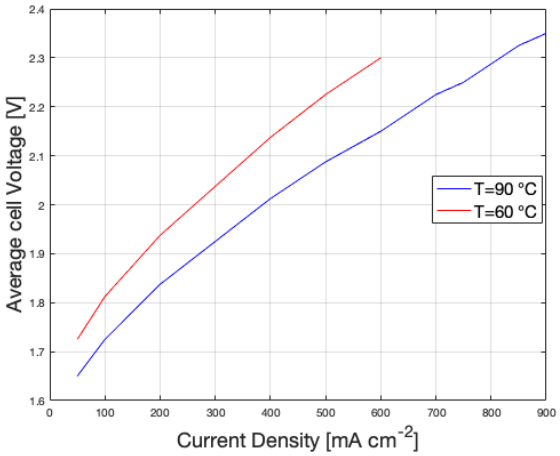

Figure 5.40: Averaged cell potential versus current density at $90\,^{\circ}\mathrm{C}$ (blue) and $60\,^{\circ}\mathrm{C}$ (red) at $50\,\mathrm{bar}$. The $60\,^{\circ}\mathrm{C}$ line is limited at high current densities by the temperature.

The targets set by ZEF are in terms of efficiency, crossover, lifetime and costs at a specific operating points: $100\,\mathrm{mA\,cm^{-2}}$, $50\,\mathrm{bar}$ and $90\,^{\circ}\mathrm{C}$. A detailed cost and lifetime estimation is not included in this research and is left as a recommendation. Two other targets are: 70 % faradaic efficiency and a crossover below the 50% LEL. It is concluded that both targets have been accomplished with the acquired system. The electrolyte deterioration experiments of which results are reported in section 5.3 form the first step of a lifetime estimation.

Pressure booster flow rates

The pressure booster was tested at different pressures as part of the electrolysis setup. If the pressure booster was correctly primed and operational [11], the pressure booster was able to overcome the system pressure at replenish the consumed water at the entire pressure range of $1\,\mathrm{bar}$ to $50\,\mathrm{bar}$. The volume flow rate of the pressure booster at $50\,\mathrm{bar}$ is derived by shutting down the electrolysis system and switching on the pressure booster and record the pressure increase with respect to time. Under the assumption that the gasses are compressed adiabatically, an average volume flow rate is determined to be approximately $6\,\mathrm{mL\,min^{-1}}$. Therewith the maximum allowed water consumption is set if. Using the number of cells (16), the Faraday constant ($96\,485\,\mathrm{C\,mol^{-1}}$ and the cell area ($60\,\mathrm{cm^2}$), the maximum allowable current density is determined to be $1126\,\mathrm{mA\,cm^{-2}}$; this is higher than the maximum current density of the power supplies and therefore the pressure booster is not expected to form a bottleneck and the dimensions and power consumption are considered to be satisfactory.

Degasser overflow

An important finding regarding the degasser is that it overflows from a pressure of $20\,\mathrm{bar}$ and higher, a picture of the experiment in which the $20\,\mathrm{bar}$ overflow pressure is found is included in Figure 5.41. The overflow typically takes place right after the start of the oxygen purge, introducing a relative large

[11] Frequently the pressure booster was not operational as a consequence of unexpected system traits, see subsection 5.2.2.

amount of gas into the degasser which pushes the liquid upwards causing the overflow. Instead a more quiescent flow is desired in which relatively small bubbles are formed and the pushed up water flows down along the bubbles. However the initial gas is purged to violently through the degasser.

Figure 5.41: Degasser overflow pressure experiment. The water level of overflow tank and the water level of the degasser are indicated with the red markers. The pressure is gradually increase until the overflow level is increased after an oxygen purge valve opening

Prior to installation at the electrolysis setup, the degasser was tested in a separate test facility using water and nitrogen. Overflow was solely observed at the electrolysis setup and not in the separate test facility. Therefore the degasser was considered satisfactory and installed in the electrolysis system.
An important difference between the test facility and the electrolysis setup are the capillary tubes on the oxygen side, besides the difference in operating gas (oxygen versus nitrogen). The capillary tube used in the test facility was significantly longer and possibly has a smaller diameter. Therefore the gas flow is entered more gradual and overflow is prevented.
The overflow can finally be attributed to the fact that the degasser is developed independently form the electrolysis setup and the capillary tubes, opening times and accompanying flows in specific. The recommendation following from this finding is dual-fold. First of all, it is recommended to design the degasser not independently from the electrolysis setup, but to size and test the degasser accordingly. The second recommendation is, considering the acquired system, to enlarge the degasser diameter to accommodate the more violent gas purges and to increase the oxygen outlet diameter on top of the degasser[12].
Valve opening times were adjusted to accommodate the initial gas purge which causes overflow. The oxygen purge valve is opened for $400\,\mathrm{ms}$ and subsequently closed for $400\,\mathrm{ms}$ and then the oxygen purge valve is opened for the remaining valve opening time. This increased the overflow pressure from $20\,\mathrm{bar}$ to $25\,\mathrm{bar}$. The degasser was disregarded for the experiments regarding the limitations of the operational envelope.

[12] An additional observation has been made, in an experiment in which the degasser did not overflow: oxygen reached the bottom of the overflow tank and bubble through the overflow tank water to the atmosphere. This indicated that the pressure drop over the oxygen outlet is too large and pressure builds up in the degasser which is designed to have atmospheric pressure.

5.2.1. Use case & Comparison to industry and literature

Apart from the aforementioned efficiencies, other relevant properties are included to give a complete picture of system performance. The 16-cell stack corresponds to a micro plant in which approximately $30\,\mathrm{g\,h^{-1}}$ is produced. Given the 3:1 ratio in the reaction between hydrogen and methanol moles, the molar mass of methanol ($32\,\mathrm{g\,mol^{-1}}$), the number of cells (16) and cell area ($60\,\mathrm{cm^2}$), the required current density is calculated to be $\sim 150\,\mathrm{mA\,cm^{-2}}$. Given the intermittent energy source in the form of solar power, a scenario which deviates from this particular point is conceivable and therefore a range of current densities is considered: $100\,\mathrm{mA\,cm^{-2}}$ to $200\,\mathrm{mA\,cm^{-2}}$ at $50\,\mathrm{bar}$ and $90\,^{\circ}\mathrm{C}$.
ZEF's electrolysis system is compared on different aspects with one example taken from literature: the recent work of Jang et al. presents an elaborate analysis on the influence of pressure on alkaline electrolysis, balance of plant power and overall system efficiency [35]. Furthermore, the performance of the acquired system is compared to an example from industry: the HyProvide A30 from Green Hydrogen Systems [23], Table 5.5 shows the characteristic properties of the three evaluated systems. However, both the system evaluated in the work of Jang et al. and the HyProvide A30 are considerably different from the acquired system, the HyProvide system operates at $35\,\mathrm{bar}$ and has a significantly larger H_2-production for example. As one can see is ZEF's system comparable in terms of power con-

Comparison at 50% load conditions, 100 $\mathbf{mA\,cm^{-2}}$ in ZEF's system and Jang et al.[35]

Parameter	Unit	ZEF	HyProvide	Jang et al.[35]
Pressure	bar	50	35	50
Temperature	$^{\circ}\mathrm{C}$	90	-	70
H_2-Production rate	$\mathrm{N\,m^3\,h^{-1}}$	40.43×10^{-3}	30	33.43
H_2-Production rate	$\mathrm{kg\,h^{-1}}$	3.61×10^{-3}	2.7	2.99
Average cell voltage	V	1.725	-	1.62
Power consumption	$\mathrm{kWh/Nm^3}$	4.10	4.15	3.80
Efficiency (HHV)	%	85.8	85.2	91.3

Comparison at 100% load conditions, 200 $\mathbf{mA\,cm^{-2}}$ in ZEF's system and Jang et al.[35]

Parameter	Unit	ZEF	HyProvide	Jang et al.[35]
Pressure	bar	50	35	50
Temperature	$^{\circ}\mathrm{C}$	90	-	70
H_2-Production rate	$\mathrm{Nm^3\,h^{-1}}$	80.85×10^{-3}	60	66.85
H_2-Production rate	$\mathrm{kg\,h^{-1}}$	7.22×10^{-3}	5.4	5.97
Average cell voltage	V	1.83	-	1.69
Power consumption	$\mathrm{kWh/Nm^3}$	4.34	4.17	3.96
Efficiency (HHV)	%	80.5	85.0	87.6

Table 5.5: Efficiency and power consumption benchmarks, ZEF's electrolysis system compared to state-of-the-art pressurised alkaline electrolysis systems. One benchmark is taken from industry: HyProvide-A20 by Green Hydrogen Systems[23]. One benchmark is taken from literature: in 2021 Jang et. published an elaborate modelling study of alkaline electrolysis under operating conditions corresponding to $100\,\mathrm{mA\,cm^{-2}}$ to $200\,\mathrm{mA\,cm^{-2}}$.

sumption and efficiency. The relatively small scale of ZEF's electrolysis is also directly reflected in the table: almost a factor 1000 smaller in terms of production rate in comparison to the benchmark systems. In addition to the more elaborate comparison presented in Table 5.5, an additional comparison considering power consumptions only and commercially available alkaline electrolysers can be seen inf Figure 5.42. Starting from Figure 5.42, it can be seen that the acquired system (leftmost bar) has a comparable power consumption as commercially available systems. However, only comparison of a rather generic metric is displayed and relevant details of the systems are not expressed. For example, whether stack power only, or BoP power is also included in the power consumption. In the study of Jang et al., the power consumption of the BoP is analysed separately. In Table 5.5, only the stack power consumption and efficiency are compared. Comparison of BoP power consumption depends largely on the definition of the BoP and with that what is considered to be part of the BoP and what not.

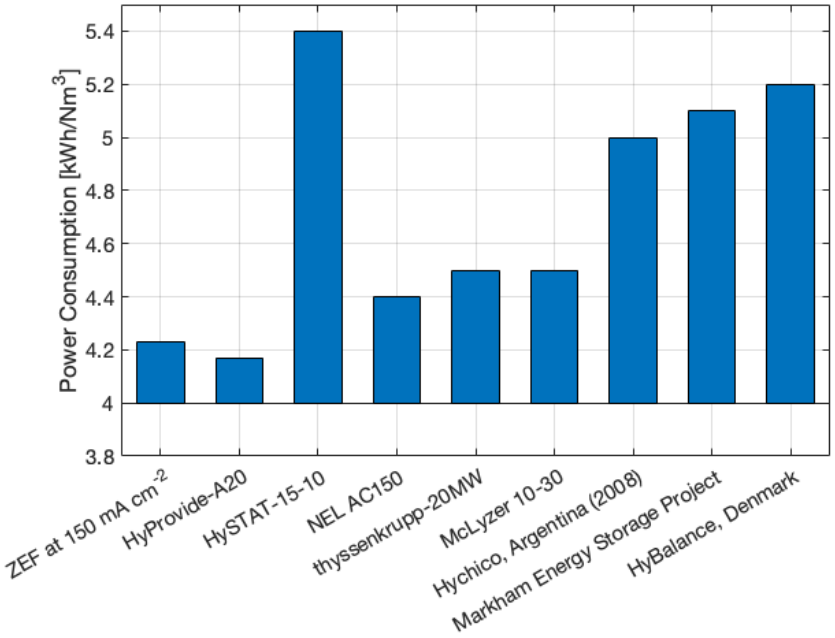

Figure 5.42: Power consumption expressed in kilo watt hour per normal cubic meter, the leftmost bar represents the power consumption of ZEF's electrolysis system at at current density of $150\,\mathrm{mA\,cm^{-2}}$. The other bars represent the power consumption of alkaline electrolysers in industry, values obtained from references in order of appearance: [23, 84, 56, 85, 51, 84, 84, 84]

Besides, the exact power consumption of all electronics is ZEF's electrolysis system is not determined and possibly differ substantially from the final product, because the current setup has a number of sensors implemented for research in contrast to the final product which has to be more cost-effective [43]. Therefore, BoP power consumption is considered not suitable for comparison in this stage of ZEF's electrolysis system and is therefore not included.
To complete the perspective on ZEF in relation to industry and literature, a detailed life cycle assessment, BoP power consumption determination and cost analysis is recommended.

5.2.2. Unexpected findings

In the experimentation phase, different unforeseen findings have been done and the most relevant are described in this subsection. Other unexpected findings are considered irrelevant in view of ZEF's desired electrolysis setup or the scientific reporting of the system characteristics and are therefore not included in this research. The findings are reported chronologically, because specific additional verification experiments or imposed solutions led to other relevant findings. The findings are structured as follows: first, the notable observations are stated which led to further investigation. Secondly, a possible explanation for the found observation is presented. In addition, verification of the proposed explanation is described, if applicable. Lastly, recommendations are formulated such that the described phenomenon can be considered in the design of future generations of ZEF's electrolysis system.

Pressure Booster Priming issues
Observation - 1) The pressure booster showed difficulties during installation, bubbles stuck in the compression chambers and it was not able to build up pressure. 2) Once the pressure booster was primed it showed difficulties similar to the aforementioned priming issues, but after a long period of smooth operation. Bubbles were observed in the filter right on the low pressure side of the pressure booster. In addition to that, a pressure increase from $1.2\,\mathrm{bar}$ to $2.3\,\mathrm{bar}$ overnight was observed while the stack was turned off.
Explanation - 1) The pressure booster is taken from a pressure washer with a significantly volumetric flow rate and a motor with a higher rotational speed than applied in the electrolysis system. Possibly, the internal check valves leak and therefore loose the ability to build up pressure at very low volumetric flow rates. 2) A first possible explanation comprehends a leaking check valve on the high pressure

side. With a leaking check valve, electrolyte (30 wt% KOH solution) leaks into the aluminium pressure booster which subsequently corrodes, see Figure 5.45a. In this corrosion process, hydrogen gas is produced and aluminium is oxidised to aluminium hydroxide. Subsequently, the formed hydrogen gas in the pressure booster opposes the initially primed state of the pressure booster.

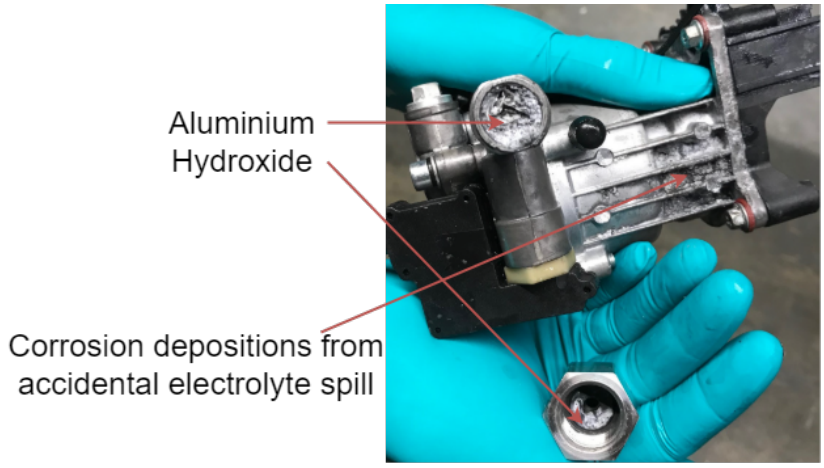

Figure 5.43: Corroded pressure booster, picture taken from the high pressure side. Aluminium hydroxide can be seen in the high pressure line itself, indicated by the upper red arrows and on the coupling to which it is attached, indicated by the lower red arrow.

Figure 5.44: A sample taken from the liquid on the high pressure side. The white-grey colour originates from the formed aluminium hydroxide - $Al(OH)_3$, an intermediate product of the corrosion of aluminium in alkaline media, pH 12.5

Verification - 1) The priming issues are solved by manually loosening the bubbles by hitting the pressure booster, indicating that indeed the bubbles are causing the initial priming issues. Secondly, another motor, with higher rotational speed, is tested and pressure was indeed built up rapidly at a higher RPM, approximately 300 RPM suffices to build up pressure. 2) The pressure booster is opened and a large deposition was found, see Figure 5.43. As one can see in Figure 5.44, the liquid inside the high pressure line was grey-white coloured and a pH of 12.5 was measured, indicating an alkaline solution which can be explained by electrolyte reaching the pressure booster. The grey-white colour indicates the presence of aluminium hydroxide salt - $Al(OH)_3$ which is an intermediate product in aluminium corrosion in alkaline solutions with a limited solubility [100, 61]. The overall reaction equation (without intermediate steps) of aluminium corrosion in alkaline media can be seen in Equation 5.4 and is based on the work of Zhang et al.[100] and Pyun et al.[61][13].

$$Al + 3H_2O + OH^- \longrightarrow Al(OH)_4^- + \frac{3}{2}H_2 \qquad \text{Aluminium corrosion in alkaline media} \qquad (5.4)$$

The ICP results of the liquid inside the high pressure line of the pressure booster, depicted in Figure 5.44, showed a large dissolved aluminium content: approximately 520 ppm. In addition, the check valves were tested separately both at high pressure differences and low pressure difference across the check valve. A possible check valve leakage was not detected.

Recommendation - 1) A simple solution to the priming issues is to install a motor with a higher rotational speed. If the same pump is used, the resulting higher volumetric flow rate can be compensated by a shorter filling duration. 2) The water line from the pressure booster to the system is routed differently, see Figure 5.45b. Instead of replenishing water at the bottom of the pressure equalisation tube, the top level sensor on the hydrogen side is replaced by a tube connected to the high pressure side of the pressure booster. In this configuration, water is replenished in the gas phase in the hydrogen tank, such that the water line and the electrolyte do not longer make contact.

[13] In which the oxygen content is assumed to be negligible in the electrolyte solution at the aluminium surface. In the presence of oxygen, an oxygen reduction reaction takes place in addition to the water reduction to hydrogen[61]

(a) Original design, water is replenished at the bottom of the downcomer tube. Leakage through the check valve could have led to the observed corrosion of the pressure booster and the alkaline solution found in the pressure booster.

(b) Adapted water replenishment. In this configuration the water line and the electrolyte are not separated by a check valve prone to leaking, but by a gas phase. In this configuration, electrolyte reaching the pressure booster is avoided.

Figure 5.45: Schematic representation of two different water replenishment routings. The original design (left) and the adapted design (right).

Spilling accident November 11th 2021
Observation - 1) During water replenishment, the level sensors (on the bottom and in the middle of the tank) on the hydrogen side did not show a low value corresponding to a wet level sensor but continued to show a high value, corresponding to a dry level sensor. On the oxygen side however, the corresponding level sensors showed values as expected: first the bottom level sensor became wet and subsequently the middle level sensor. Alongside, pressure on both sides increased during the excessive filling, indicating an increase in liquid volume, corresponding to a compression of the gasses. 2) After switching on the system for a second, the hydrogen level sensors did show low voltage values, corresponding to wet level sensors. Subsequently, the system turned out to be overfilled and therefore an electrolyte volume was drained at atmospheric pressure. The level sensors on the oxygen side again show values as expected: first the middle sensor and subsequently the bottom sensor became dry. The hydrogen side however remained at low voltages, corresponding to wet level sensors. Removal of a level sensor on the hydrogen side led to a spillage of transparent, uncoloured liquid.
Explanation - Both observations can be explained by stratification of water on top of the electrolyte, because water has a significantly lower density ($0.998\,\mathrm{g\,mL^{-1}}$) than the electrolyte, 30 wt% KOH solution ($1.292\,\mathrm{g\,mL^{-1}}$ [22]) and the poor conductance of demi water in comparison to the electrolyte. Conduction through the liquid is essential to level detection of that liquid using the particular level sensors as explained in subsection C.3.2. The short duration of stack operation in between observation 1 and 2 mixed the water stratification enough to recover the conductance throughout the water layer. However, the density difference between the water layer and the electrolyte remained and explains the difference in levels measure by the level sensor on hydrogen and oxygen side and the spill accident. The stratification is depicted schematically in Figure 5.46.
Verification - An elaborate verification of the aforementioned explanation is not executed. Although, the aforementioned spill accident showed coherence to the given explanations; the spilled liquid did not leave salt deposits and did not discolour paper towel. Both observations do not apply to electrolyte spill. In light of the volume of spilled liquid and the circumstances of the spill accident, pH measurement was deemed unfeasible.
Recommendation - To avoid the stratification and malfunctioning level sensors, multiple solution suffice. Firstly, water replenishment only during stack operation secures mixing and prevents the stratifi-

Not included for copyright reasons

spillevent11-11-2021.drawio.png

Figure 5.46: Stratification of water on top of the relatively more dense electrolyte. In this configuration, water is replenished in the hydrogen gas phase to avoid pressure booster corrosion. It demonstrates that a density difference between pure water and electrolyte results in different levels on the hydrogen and oxygen side.

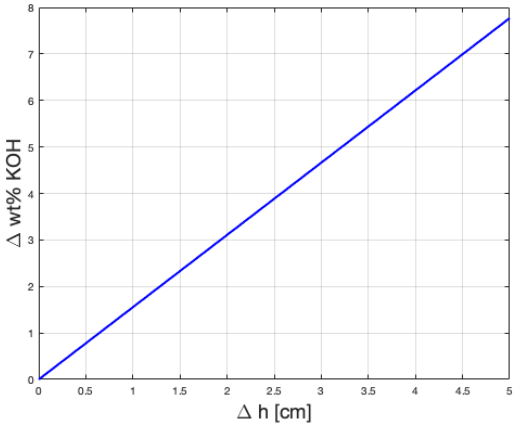

Figure 5.47: Difference of weight percentage of the electrolyte between the hydrogen and oxygen side as a function of the height difference. A concentration difference between the two sides can be determined indirectly by measuring the liquid level difference. The weight percentage difference is defined as $\Delta wt\%KOH = wt\%KOH_{H_2} - wt\%KOH_{O_2}$ and the liquid level difference is defined as $\Delta h = h_{O_2} - h_{H_2}$

cation. Secondly, reverting the routing of the water replenishment line to the bottom of the downcomer and the use of functioning check valves avoids stratification independent from stack operation.
Nevertheless, the spilling accident points out an unforeseen, but possibly relevant feature of the current system: an average concentration difference between the electrolyte on the hydrogen and oxygen side can be determined indirectly. Due to the multiple level sensors and due to the fact that a KOH-concentration difference corresponds to a density difference and consequently a level height difference. The measured liquid level difference can be used to determine the concentration difference using a force balance, Equation 5.5, and assuming that the weighted average of two densities is equal to the density of 30 wt% KOH-solution, denoted as ρ_{el}, which is essentially a mass balance, Equation 5.6.

$$\rho_{el,H_2} \cdot g \cdot h_{H_2} = \rho_{el,O_2} \cdot g \cdot h_{O_2} \qquad \text{Force Balance} \tag{5.5}$$

$$\rho_{el} = \frac{V_{el,H_2} \cdot \rho_{el,H_2} + V_{el,O_2} \cdot \rho_{el,O_2}}{V_{el,H_2} + V_{el,O_2}} \qquad \text{Mass Balance} \tag{5.6}$$

In Figure 5.47, a graphical representation of the two governing equations can be seen and a level difference can be linked to a concentration difference. The relevance of this feature emerges from the possibility of creating concentration differences over time and its implications. A possible source of concentration difference is continuous operation for a relatively long time, in which water is consumed in the cathodic hydrogen side (increasing the KOH-concentration on the hydrogen side) and creating water at the oxygen side (decreasing the KOH-concentration), as can be seen in the half reactions, Equation 2.2 and Equation 2.3. Deviation from the 30 wt%KOH optimum possibly leads to loss of efficiency. In literature, this concentration gradient in the electrolyte is put forward as an argument to use mixed electrolyte cycles, despite the accompanying increased crossovers [86, 73].

Electrolyte Mist

Observation - 1) After continuous operation, the pressure booster was in an unprimed state en bubbles were visible in the fuel filter on the low pressure side. 2) The polycarbonate degasser tube was burst as can be seen in Figure 5.48 and leaked. In Figure 5.49, a close up of the bottom part of the degasser tube can be seen, in which more and smaller cracks can be seen. 3) The water left in the cracked degasser tube had a pH of 13, indicating an alkaline solution.

Figure 5.48: Image of the burst degasser, the crack is located an approximate $7\,\mathrm{cm}$ from the degasser bottom, close to the air stone thorough which the oxygen, and electrolyte mist, enters the degasser.

Figure 5.49: A close-up of the bottom part of the cracked degasser depicted in Figure 5.48, several small cracks and damage are visible

Explanation - All three observations can be explained by electrolyte reaching the degasser tube through the line connecting the oxygen buffer tank and the degasser bottom. Polycarbonate degrades in alkaline media, which could lead to the observed crack [33].The entering of electrolyte in the degasser is considered to have two possible root causes. Firstly, it has been observed during commissioning that the system was accidentally overfilled; possibly the electrolyte was injected directly in to the degasser or residues in the oxygen purge line have been transported to the degasser by the purged oxygen. A second explanation can found in what is referred to as electrolyte mist: small droplets leaving the buffer tank and ending up in the degasser, carried by oxygen gas during valve openings.
In retrospect, it explains the initial corrosion of the pressure booster. The result of the aforementioned check valve leaking test was not in agreement with the initial hypothesis of electrolyte leaking through the check valve.

Verification - The surroundings of the degasser are examined to exclude the possibility of a bending moment causing the cracks. Secondly, the oxygen purge line is replaced by a new line and couplings are cleaned thoroughly. A $200\,\mathrm{mL}$ demi water sample is connected at to the oxygen purge line and the system is operated for several hours. During the verification experiment, the top level sensor on the oxygen side remained dry, excluding the direct electrolyte spill case. pH-Measurement before and after the stack operation showed a significant increase: from 7 to 11.2. With the number of oxygen purges during stack operation, 52, an average of $8.6 \times 10^{-4}\,\mathrm{mL}$ electrolyte entering the degasser per oxygen purge is determined. The calculations are depicted schematically in Figure 5.50. This experiment and additional calculations are done in this specific situation, the possible dependency of electrolyte mist volume on operating conditions is not investigated.

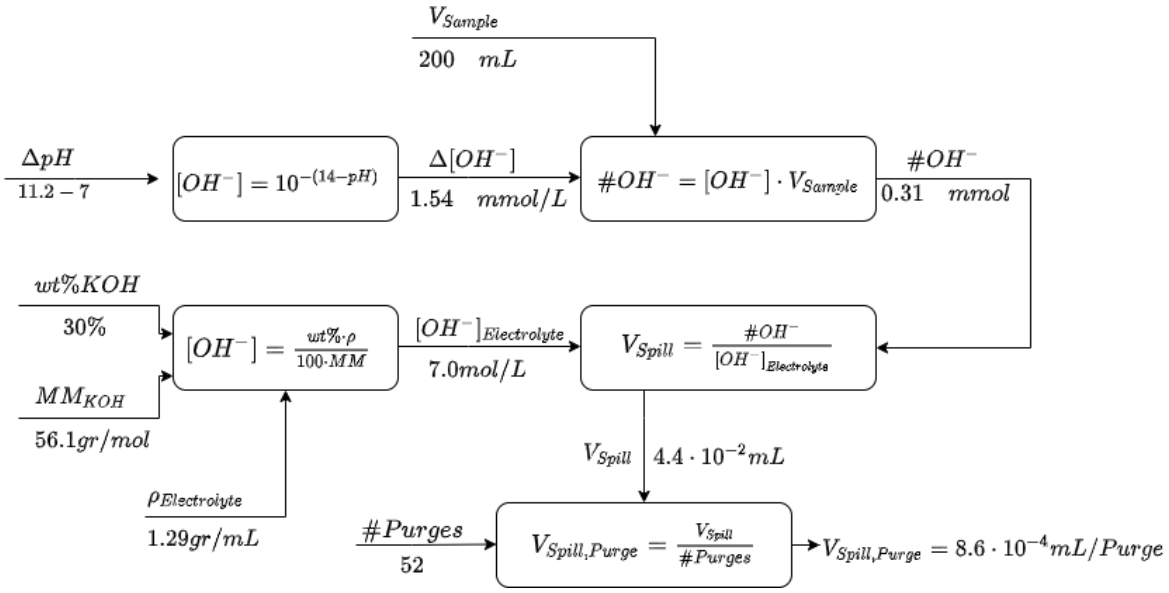

Figure 5.50: Schematic representation of the calculations steps to determine the average electrolyte volume that enters the degasser during oxygen purges.

Recommendation - To avoid damaging the degasser, pressure booster and the methanol synthesis reactor in future generations of ZEF's setup, removal of electrolyte from the product gases is necessary. Consultation of literature manifests the widely applied solution to this undesired phenomenon: demister pads or gas washers [13, 86, 38, 10, 25, 66, 49]. In Figure 5.51, an example of an aerosol filter from industry is depicted, in which the filtered liquid can be reintroduced in principle. Recuperation of the spilled electrolyte ensures a constant electrolyte concentration. The implementation of demisters or gas washers is considered to be paramount to obtain a durable electrolysis setup an is therefore considered to be one of the most important outcomes of this research.

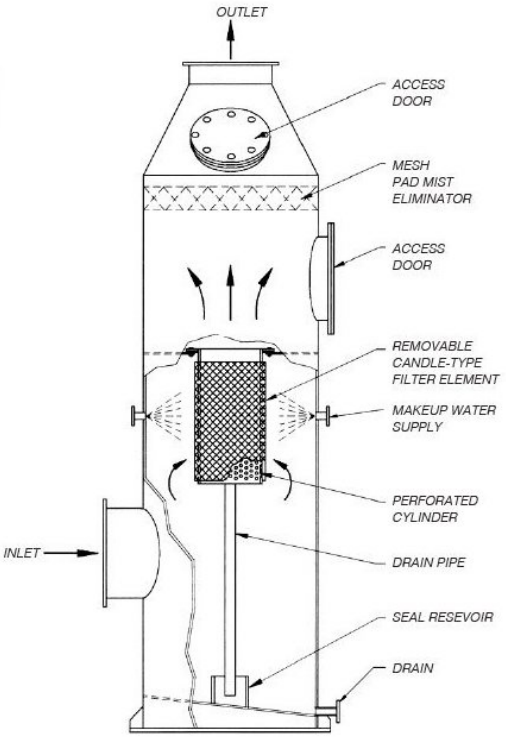

Figure 5.51: Example of an industrial aerosol filter, Cleanable High Efficiency Aerosol Filtration System (CHEAF), made by Verantis [89] and used in ammonium nitrate production.

Residual Findings

In addition to the operational envelope, the general characterisation and the findings described above, additional findings, experiments and outcomes can be found in an appendix ,Appendix A. For example the observed 10% current difference in power supplies in section A.3, or the pressure difference tests to explicitly capture the influence of the capillary tubes during valve openings in section A.2. All experiments described in Appendix A have in common that conclusions could not have been drawn from the experiments and are therefore included in the appendices. In addition to the aforementioned additional experiments, a table of residual findings can be found in a table in Table A.2. The residual findings are relevant to obtain a complete image of the system, but neither additional experiments have been conducted, nor all explanations to findings are validated. The residual findings are complementary to the previously described findings.

5.3. Electrolyte Deterioration

The results of the analysed electrolyte samples can bee seen in Table 5.6. The previously described electrolyte mist has a significant effect on the electrolyte deterioration experiments as can be seen in the table directly. Firstly, the increasing aluminium content which originates from the corrosion of the pressure booster. Secondly, a 30 wt% KOH solution corresponds to a potassium level of about $209 \times 10^3\,\mathrm{mg\,kg^{-1}}$, Table 5.6 manifests the loss in potassium level, either via reactions or via electrolyte mist. The purging of electrolyte mist dilutes the electrolyte, because electrolyte leaves the system through the capillary tubes at approximately $8.6 \times 10^{-4}\,\mathrm{mL}$ per oxygen purge and is replenished with demineralised water. Therefore the loss in potassium is not only due to the deposition of salts, but also due to gas purges. The samples are taken with relatively long periods of operation in between, given the large variety of operating conditions (and thus valve opening frequency) and the uncertainty in the exact volume of total spilled electrolyte, the potassium loss as a consequence of the electrolyte mist cannot be determined reliably.
The electrolyte deterioration experiments are disturbed in a second form, the observed increase of pH in the degasser water is not representative to normal operation from a chemical perspective. The reactions between CO_2, $HCO^-_{3(aq)}$ and hydroxide ions, Equation 5.7 and 5.8 have a higher reaction rate in comparison to the equilibria represented in section 4.3 [8, 46]. Consequently, the carbonate level in the feed water is higher in comparison to a situation with neutral feed water in the degasser. Essentially introducing a relatively high amount of carbonates in the electrolyte, which in turn distort the outcomes.

$$CO_{2(aq)} + OH^- \iff HCO^-_{3(aq)} \qquad (5.7) \qquad\qquad HCO^-_{3(aq)} + OH^- \iff CO^{2-}_{3(aq)} \qquad (5.8)$$

Focusing on the third sample, both the potassium level and density of the sample taken after approximately $200\,\mathrm{h}$ are determined. Starting from the density, using Equation 5.9 found in the work of Gilliam et al.[22], delivers a corresponding weight percentage of 25.2 wt% of KOH, which underlines the significant electrolyte loss due to electrolyte mist. Under the assumption that only water and KOH form the electrolyte, the determined weight percentage prescribes a potassium level of $176 \times 10^3\,\mathrm{mg\,kg^{-1}}$. However Table 5.6 shows a potassium level of $112 \times 10^3\,\mathrm{mg\,kg^{-1}}$, indicating that potassium has reacted with carbonates and deposited as described in section 4.3. This example shows that additional density measurement gives insight in the actual electrolyte concentration and is therefore recommended to include in follow-up research. In addition to density measurements, pH measurements and ionic chromatography are considered to give more insight in the composition of the electrolyte.

$$\rho_{el} = A \cdot e^{(0.0086 \cdot wt\%)} \qquad \text{For } T = 20\,^\circ\mathrm{C},\ A = 998.15\ [22] \qquad (5.9)$$

In conclusion, the electrolyte deterioration experiments are deemed inconclusive and confirmation of appropriate degasser performance regarding limited electrolyte deterioration by CO_2 is left as a recommendation.

	Approximate Operation Duration		
	10 h	50 h	200 h
ρ [kg m^{-3}]			$1.239\,65 \times 10^3$
Element			
K [mg kg^{-1}]	167801	2390	112×10^3
Al [mg kg^{-1}]	18.5	64.0	
Ni [mg kg^{-1}]	1	0.0	
Si [mg kg^{-1}]	22.8	5.7	
Remarks	During pressure booster corrosion	After pressure booster corrosion	Without degasser and pressure booster

Table 5.6: Results of the electrolyte deterioration experiments.
The first two columns correspond to the Inductively Coupled Plasma (ICP) analysis of the electrolyte samples after respectively 10 h, when the electrolyte mist was still undiscovered, and 50 h directly after the aforementioned discovery. The last sample is taken 200 operation hours after the electrolyte has been refreshed and without degasser or pressure booster connected, only the potassium level and the density are determined for this sample.

6

Conclusions & Recommendations

6.1. Conclusions

In this research, the experimental characterisation of an integrated $50\,\mathrm{bar}$ alkaline electrolysis system was central. A new balance of plant is designed and realised to solve problems in the previous setup and to add functionalities. The system is characterised by means of an operational envelope, which depicts al safe operating points in terms of current density and pressure at a given temperature. Furthermore, the electrolyte quality is tested to investigate a possible decrease of system performance over time. The research questions, as defined in section 1.3, are answered throughout the system characterisation and operational envelope.

"How does the safe operational envelope look in terms of pressure & current density of the AEC system with the proposed conceptual solutions implemented?"

This research question is answered by the experimentally determined operational envelope, Figure 6.1.

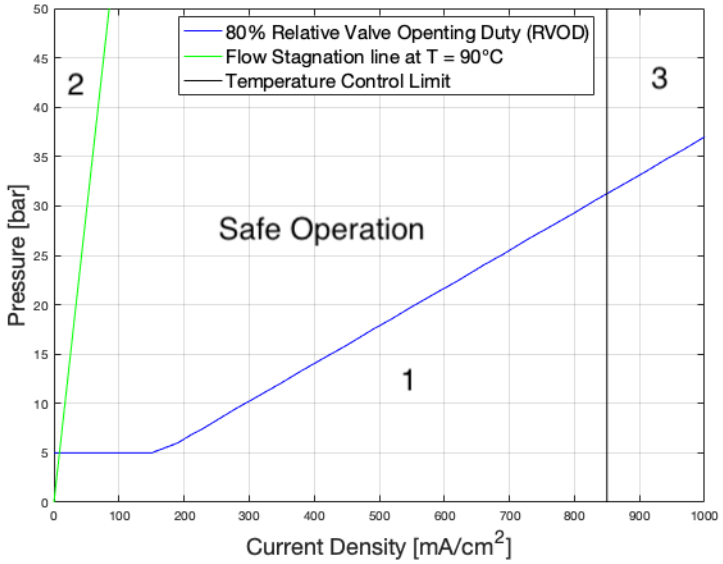

Figure 6.1: The experimentally determined operational envelope at $90\,^{\circ}\mathrm{C}$. The three limitations emerge from three different phenomena: (1) Relative valve opening duty as a consequence of purging through capillary tubes. (2) Flow stagnation as a consequence of a buoyancy driven electrolyte circulation. (3) Temperature control as consequence of the limited cooling capacity of the finned tube heat exchanger. Crossovers are found to be not limiting for all operating points.

An additional parameter, the Degree of Flexibility, was defined to capture to what extent the system

allows to operate safely under different operating conditions and is calculated by the ratio of number of safe operating points to the total number of possible operating points the system is designed for; the degree of flexibility (at $90\,°\mathrm{C}$) corresponds to the ratio of the area marked with 'Safe Operation' to the total area bounded by the horizontal and vertical axis in Figure 6.1 and has a value of 0.527.
In the derivation of the operational envelope and the evaluation of the balance of plant design, the following sub questions are answered:

To what extent is the stack temperature controllable?

A finned tube heat exchanger with cross-flow fans is designed and implemented to cool the electrolyte and therefore acquire temperature control. A fundamental change with respect to the previous system in which temperature was uncontrollable and an outcome of the other operating conditions: pressure and current density.
Based on a limited data set, the temperature control experiments showed that the limiting $90\,°\mathrm{C}$ is reached at approximately $450\,\mathrm{mA\,cm^{-2}}$ and $850\,\mathrm{mA\,cm^{-2}}$ corresponding to operation at 0 % and 100 % cross-flow fan power respectively at an operating pressure of $50\,\mathrm{bar}$. A pressure dependency of the temperature control is not found at low current densities; relative valve opening duty prohibited to test the pressure dependency at high current densities. The electrolyte mass flows are derived from the temperature difference over the stack for different current densities. The required electrolyte flow in the heat exchanger design was found to be in the ball park of the electrolyte mass flows found experimentally. The degree of temperature control is defined as a measure to describe to what extent the temperature is controllable on the available current density and temperature domain, its numerical value is determined to be 0.25.

What is the effect of purging through capillary tubes ?

The capillary tubes are implemented together with a control algorithm that is designed to calculate valve opening times corresponding to a discharge volume corresponding to a $1\,\mathrm{cm}$ electrolyte level drop, at a given current density, pressure and temperature. The relative valve opening duty (RVOD), that is the percentage of time the valve is opened, is defined as a parameter to examine safe operation: the operational conditions corresponding to a RVOD larger that 80 % are considered unsafe. The model predicting the cycle times and RVOD is validated and the experiments show an additional pressure drop resulting in a smaller discharge volume and a shortened cycle. On the oxygen side, both are attributed to the interdependency of the two valve cycles; on the hydrogen side, the additional pressure drop results in an smaller discharge volume and is considered a result of (partially) clogging of the capillary tube.
A corrected has been made which approximates the cycle times more accurate. Furthermore, a $5\,\mathrm{bar}$ minimum operating pressure was found to control the electrolyte levels.
The capillary tubes increase the opening times significantly and therefore the electrolyte levels drop and raise less violently, with the intention to result in less pressure difference across the membrane, less mixing through the pressure equalisation tube and therefore less crossover. The pressure differences across the membrane during a valve opening have been measured experimentally, but the sensor noise was too large to draw conclusions.

What is the effect of long, large diameter downcomers on crossover and flow stagnation?
As a consequence of an increase of the number of cells and the increased height difference between the stack and the buffer tanks, the operational limitation due to flow stagnation is decreased significantly. A defined value X, which represents the gas volume production rate, has been used to derive a flow stagnation prevention criterion: $X > 0.74\,\mathrm{A\,K\,bar^{-1}\,cm^{-2}}$. The large height difference between the stack and the buffer tanks have decreased the minimum current density to avoid flow stagnation at a given pressure and temperature, resulting in a minimum current density criterion of $\sim 87\,\mathrm{mA\,cm^{-2}}$ at $90\,°\mathrm{C}$ and $50\,\mathrm{bar}$.
The large volume pressure equalisation tube decreases the crossover due to electrolyte mixing between the hydrogen and oxygen side, although the particular contribution of the large volume pressure equalisation tube to crossover decrease has not been tested explicitly.

What is the effect of the midplate-stack design on crossover?

The midplate-stack design was based on the parasitic hydrogen production hypothesis described in subsection C.3.1, which has been confirmed. The crossovers are significantly below the 50 % LEL and 50 % UEL safety criteria. Concluding that crossover does not form a limitation on the operational envelope, up to the lowest tested current density of $10\,\mathrm{mA\,cm^{-2}}$.

Apart from the operational envelope itself, the system has additional properties which are not, or not directly, expressed in the operational envelope.
The pressure booster, which replenishes the consumed water, is found to be sensitive to priming issues due to the combination of internally leaking check valves and relatively low angular velocity of the motor shaft. Apart from priming issues, the pressure booster was able to provide appropriate pressure and flow rate to replenish the water for all operating points.
From $20\,\mathrm{bar}$ and higher, an overflow of the degasser was observed and this was attributed to the mismatch between the capillary tubes used in the electrolysis setup and in the test facility, on which the degasser has been tested at all operating pressures. The larger diameter capillary tube used in the system lead to relatively violent oxygen purges which caused the overflow and can be prevented by using a larger diameter degasser.
The pressure booster and degasser have been damaged by electrolyte mist, which lead to what is considered to be one of the most impactful findings: a gas washer or demister is essential to yield pure product gases and to avoid damage and malfunctioning of the degasser and pressure booster.
The system efficiency on the reference point of $100\,\mathrm{mA\,cm^{-2}}$, $50\,\mathrm{bar}$ and $90\,^{\circ}\mathrm{C}$ is concluded to be satisfactory according to the targets set by ZEF: 71 % Faradaic efficiency. The power consumption at the same operating point is $4.10\,\mathrm{kWh/Nm^3}$ which is comparable to systems found in literature and industry.

"What is the effect of degassing CO_2-rich feedwater on the quality of the KOH electrolyte?"

Determination of electrolyte deterioration could not have been determined in this research. The results of the inductively coupled plasma analyses are considered inconclusive as a consequence of the electrolyte mist. The electrolyte is diluted over time, because electrolyte leaves the system and is replenished by demineralised water. Furthermore, the hydroxide ions purged into the degasser water convert the CO_2 in the degasser water to carbonates, essentially increasing the level of contaminants in the electrolyte which impedes reliable electrolyte deterioration determination.

6.2. Recommendations

The final section of this thesis is dedicated to formulate and propose next steps in the development of ZEF's electrolysis setup. This work presented a system characterisation considering a variety of aspects, but additional experiments can be done to comprehend system behaviour on every aspect and in more detail. In subsection 6.2.1, recommendations in the form of experiments are listed. The experiments can be conducted directly, or with a slight modification to the system and are aimed at improving or complementing the data presented in this thesis.
Recommendations regarding system development are central to subsection 6.2.2 and consist of components, system adjustments and proposals intended to advance the electrolysis system towards integration in ZEF's microplant.

6.2.1. Experimental recommendations

- **Ionic chromatography.**
  Instead of using ICP and pH to determine electrolyte deterioration, ionic chromatography can be used to determine the level of the ionic components. The level of dissolved potassium in the electrolyte, the carbonate ions and the hydroxide ions can be determined. Subsequently the expected electrolyte deterioration can be assessed with respect to the desired lifetime of 20 years.

- **Continuous system operation for several days and nights.**
  With long duration experiments, the development of a concentration gradient in the electrolyte between the oxygen and hydrogen side can be quantified experimentally. Furthermore, the robustness of stand-alone water replenishment by the pressure booster and degasser can be tested.

- **Additional flow stagnation experiments.**
  More flow stagnation experiments are recommended, as the presented data set in Table 5.2 is limited in size. If the duration of the experiments is extended, flow stagnation is ensured at certain operating conditions and flow stagnation as a consequence of operating conditions in the past is excluded. A larger data set results in either a more reliable claim regarding the flow stagnation prevention criterion in terms of the defined value X, or possibly reveals an underlying coherence to operating conditions for example.

- **Explicit capillary tube model tests.**
  The capillary tube model is only tested implicitly in this thesis, that is to say with the interference of the two purge valves. The original experimentation methodology as described in subsection 4.1.1 can be used to remove the valve interference. On the other hand, the valve interference occurs in reality and therefore the additional pressure drop and smaller discharge volume ought to be implemented in the control scheme as described in subsection 6.2.2. The electrolyte mist might cause the additional pressure drop, as described in subsection 5.1.1, which can be validated experimentally.

- **Additional temperature control experiments.**
  With more steady state temperatures at different current densities, the minimum and maximum temperature lines can be established with more accuracy and the assumed linear relation between steady state temperature and current density is possibly falsified.
  The influence of pressure on temperature control is only investigated at $50\,\mathrm{mA\,cm^{-2}}$ in this research. Investigation of pressure dependency of temperature control at high current densities is therefore recommended, as this possibly differs from pressure influence at low current densities and $850\,\mathrm{mA\,cm^{-2}}$ is found to be the limiting current density at $50\,\mathrm{bar}$.

- **Pressure difference tests.**
  The capillary tubes are installed for multiple reasons, one is to reduce the pressure difference across the membranes during a valve opening. The pressure differences have been tested in the previous electrolysis setup which operated without capillary tubes. An example of the observed damped oscillation can be found in the work of Mulder [53]. The recommendation is to repeat the experiments in the acquired system but with pressure sensors suffering less from sensor noise, such that the effect of capillary tubes on pressure differences can be assessed directly. The

pressure difference tests have been repeated in this research, but are deemed inconclusive as a consequence of relatively large sensor noise.

6.2.2. System development recommendations

- **A demister, aerosol filter or gas washer.**
  As described in subsection 5.2.2, demisting the purge gases is an essential element to adopt in the next generation of the integrated electrolysis setup. Both to avoid damage to the pressure booster, degasser and methanol reactor, but also to keep the electrolyte concentration at a constant level.

- **Pressure booster and degasser upgrades.**
  The flow rates of the pressure booster are found to be sufficient in this research. However the pressure booster was found to be sensitive to priming issues, which can be addressed by a motor with a higher RPM.
  The degasser diameter has to increase to accommodate the oxygen gas purges at all operating pressures. Furthermore, it is highly advised to size the degasser after and in correspondence with the capillary tube selection, such that overflow can be avoided. DAC water supply to the degasser has to be controlled differently than in the acquired system. Via calculation of the consumed water using the current density and time for instance.

- **Control algorithm upgrades.**
  Firstly, the implementation of the additional pressure drop and smaller discharge volume in the control scheme minimises the discrepancy between the experimental and modelled valve opening times.
  Secondly, the control algorithm can be designed to be less operator-dependent. For example, the top level sensors can be implemented as circuit breakers to switch off stack power. All sensors can be incorporated in a *Normal-Based Operation* scheme, in which any anomaly in sensor values leads to a safe shut down for example. Background information regarding ZEF's NBO strategy can be found in an appendix, section B.3.
  A start-up protocol is advised to develop and implement, such that catastrophes due to the minimum operating pressure requirement of $5\,\mathrm{bar}$ or a current density increase during a valve opening at low pressures are prevented.

- **Crossover senors upgrade.**
  As described in subsection 5.1.4, the crossover sensor housing of the oxygen sensor leaked which lead to inaccurate measurements. Applying a leak tight sensor housing directly solves this, accurate oxygen crossover data can be acquired subsequently.
  An effective improvement to the crossover measurements is a hydrogen crossover sensor that can operate in an oxygen rich environment, such as an electrochemical sensor. Such that the hydrogen crossover is determined more safe and without possible distortions due to manual gas sampling. An additional advantage is that determination of steady state can be done more reliably.

- **Temperature control upgrade** Depending on the final desired steady state operating current density, insulation might be needed to reach $90\,^{\circ}\mathrm{C}$ at low current densities using the current balance of plant (BoP). In a different, conceivable scenario, applying multiple stacks in the current BoP provides enough heat generation to reach $90\,^{\circ}\mathrm{C}$ at low current densities and is an opportunity to test the capabilities of the BoP to process larger gas production rates.

- **Product Development** The acquired setup is not a complete, saleable product yet. As mentioned before, a detailed life time and life cycle analysis is not included in this research. Furthermore, a detailed cost analysis is advised to assess the system on the final ZEF-target regarding costs per kilogram produced hydrogen: €1.20 per kilogram hydrogen.

Bibliography

[1] Tasneem Abbasi and S A Abbasi. "'Renewable' hydrogen: Prospects and challenges". In: *Renewable and Sustainable Energy Reviews* 15.6 (2011), pp. 3034–3040. ISSN: 1364-0321. DOI: https://doi.org/10.1016/j.rser.2011.02.026. URL: https://www.sciencedirect.com/science/article/pii/S1364032111000748.

[2] Agfa-Gevaert N.V. Technical Data Sheet: Zirfon Perl UTP 500. *Technical Data Sheet: Zirfon Perl UTP 500.* URL: https://www.agfa.com/specialty-products/wp-content/uploads/sites/8/2020/06/TDS_ZIRFON_PERL_UTP_500_20200525.pdf.

[3] K Al Shareef. *Optimize a degassing system and integrate it with electrolysis system*. Tech. rep. Delft: Zero Emission Feuls B.V., 2021.

[4] Afroz Alam et al. "Comparative analysis of performance of alkaline water electrolyzer by using porous separator and ion-solvating polybenzimidazole membrane". In: *Renewable Energy* 166 (Apr. 2020), pp. 222–233. ISSN: 18790682. DOI: 10.1016/j.renene.2020.11.151.

[5] Kemal Aldas, Nur Pehlivanoglu, and Mahmut D. Mat. "Numerical and experimental investigation of two-phase flow in an electrochemical cell". In: *International Journal of Hydrogen Energy* 33.14 (July 2008), pp. 3668–3675. ISSN: 03603199. DOI: 10.1016/j.ijhydene.2008.04.047.

[6] S.A.D. Ashruf. *The characteristics of an alkaline electrolysis system with integrated pressure booster*. Tech. rep. Delft: Zero Emission Fuels B.V., 2021.

[7] R. J. Balzer and H. Vogt. "Effect of Electrolyte Flow on the Bubble Coverage of Vertical Gas-Evolving Electrodes". In: *Journal of The Electrochemical Society* 150.1 (2003), E11. ISSN: 00134651. DOI: 10.1149/1.1524185. URL: https://iopscience.iop.org/article/10.1149/1.1524185.

[8] Lihong Bao and Michael C Trachtenberg. "Facilitated transport of CO2 across a liquid membrane: Comparing enzyme, amine, and alkaline". In: *Journal of Membrane Science* 280.1 (2006), pp. 330–334. ISSN: 0376-7388. DOI: https://doi.org/10.1016/j.memsci.2006.01.036. URL: https://www.sciencedirect.com/science/article/pii/S0376738806000792.

[9] Allen J. Bard and Larry R. Faulkner. *Electrochemical methods : fundamentals and applications*. 2nd ed. John Wiley & SONS, INC., p. 833. ISBN: 0471043729.

[10] Kay Bareiß et al. "Life cycle assessment of hydrogen from proton exchange membrane water electrolysis in future energy systems". In: *Applied Energy* 237 (Mar. 2019), pp. 862–872. ISSN: 0306-2619. DOI: 10.1016/J.APENERGY.2019.01.001.

[11] Michael K Bates et al. "Charge-Transfer Effects in Ni–Fe and Ni–Fe–Co Mixed-Metal Oxides for the Alkaline Oxygen Evolution Reaction". In: *ACS Catalysis* 6.1 (Jan. 2016), pp. 155–161. DOI: 10.1021/acscatal.5b01481. URL: https://doi.org/10.1021/acscatal.5b01481.

[12] P Boissonneau and P Byrne. *An experimental investigation of bubble-induced free convection in a small electrochemical cell*. Tech. rep. 1999.

[13] Jörn Brauns and Thomas Turek. *Alkaline water electrolysis powered by renewable energy: A review*. Feb. 2020. DOI: 10.3390/pr8020248.

[14] Jörn Brauns et al. "Evaluation of Diaphragms and Membranes as Separators for Alkaline Water Electrolysis". In: *Journal of the Electrochemical Society* 168.1 (Jan. 2021), p. 14510. DOI: 10.1149/1945-7111/abda57. URL: https://doi.org/10.1149/1945-7111/abda57.

[15] Buveco Gasdetection BV. *Personal communication with research & development department of BUVECO Gasdetection BV*. Delft, 2021.

[16] Alejandro N Colli, Hubert H Girault, and Alberto Battistel. “Non-Precious Electrodes for Practical Alkaline Water Electrolysis”. In: *Materials* 12.8 (2019). ISSN: 1996-1944. DOI: 10.3390/ma12081336. URL: https://www.mdpi.com/1996-1944/12/8/1336.

[17] Mark Cook. “Trends in global energy supply and demand”. In: *Developments in Petroleum Science*. Vol. 71. Elsevier B.V., Jan. 2021, pp. 15–42. DOI: 10.1016/B978-0-12-821190-8.00002-2.

[18] Ilias Daniil. *Transient modeling and control of a small-scale and self-pressurized electrolysis system*. Tech. rep. 2021. URL: http://repository.tudelft.nl/..

[19] Martín David et al. “Dynamic modelling of alkaline self-pressurized electrolyzers: a phenomenological-based semiphysical approach”. In: *International Journal of Hydrogen Energy* 45.43 (Sept. 2020), pp. 22394–22407. ISSN: 03603199. DOI: 10.1016/j.ijhydene.2020.06.038.

[20] Neofytos Dimitrou. *High pressure CO 2 degassing system for high purifying feedwater*. Tech. rep. Delft: Delft University of Technology, 2021.

[21] William J.F. Gannon and Charles W. Dunnill. “Raney Nickel 2.0: Development of a high-performance bifunctional electrocatalyst”. In: *Electrochimica Acta* 322 (Nov. 2019), p. 134687. ISSN: 00134686. DOI: 10.1016/j.electacta.2019.134687.

[22] R. J. Gilliam et al. “A review of specific conductivities of potassium hydroxide solutions for various concentrations and temperatures”. In: *International Journal of Hydrogen Energy* 32.3 (Mar. 2007), pp. 359–364. ISSN: 03603199. DOI: 10.1016/j.ijhydene.2006.10.062.

[23] Green Hydrogen Systems. *HyProvide ™ A-series*. 2021. URL: https://greenhydrogen.dk/wp-content/uploads/2021/02/A-series-brochure-2.pdf.

[24] F. Gutmann and Oliver J. Murphy. “The Electrochemical Splitting of Water”. In: *Modern Aspects of Electrochemistry*. Boston, MA: Springer US, 1983. DOI: 10.1007/978-1-4615-7461-3{_}1.

[25] Philipp Haug, Matthias Koj, and Thomas Turek. “Influence of process conditions on gas purity in alkaline water electrolysis”. In: *International Journal of Hydrogen Energy* 42.15 (Apr. 2017), pp. 9406–9418. ISSN: 03603199. DOI: 10.1016/j.ijhydene.2016.12.111. URL: https://linkinghub.elsevier.com/retrieve/pii/S0360319916336588.

[26] Philipp Haug et al. “Process modelling of an alkaline water electrolyzer”. In: *International Journal of Hydrogen Energy* 42.24 (June 2017), pp. 15689–15707. ISSN: 03603199. DOI: 10.1016/j.ijhydene.2017.05.031.

[27] J. W. Haverkort and H. Rajaei. “Voltage losses in zero-gap alkaline water electrolysis”. In: *Journal of Power Sources* 497 (June 2021), p. 229864. ISSN: 03787753. DOI: 10.1016/j.jpowsour.2021.229864.

[28] Christian Henao et al. *Simulation tool based on a physics model and an electrical analogy for an alkaline electrolyser*. Mar. 2014. DOI: 10.1016/j.jpowsour.2013.10.086.

[29] Michael A Hickner, Andrew M Herring, and E Bryan Coughlin. “Anion exchange membranes: Current status and moving forward”. In: *Journal of Polymer Science Part B: Polymer Physics* 51.24 (2013), pp. 1727–1735. DOI: https://doi.org/10.1002/polb.23395. URL: https://onlinelibrary.wiley.com/doi/abs/10.1002/polb.23395.

[30] Robert Hołyst and Andrzej Poniewierski. *Thermodynamics for Chemists, Physicists and Engineers*. Dordrecht: Springer Netherlands, 2012. ISBN: 978-94-007-2998-8. DOI: 10.1007/978-94-007-2999-5.

[31] IEA. *Hydrogen production costs by production source*. Tech. rep. Paris: International Energy Agency, 2018. URL: https://www.iea.org/data-and-statistics/charts/hydrogen-production-costs-by-production-source-2018.

[32] IEA. *The Future of Hydrogen*. Tech. rep. Paris: International Energy Agency, June 2019. URL: https://www.iea.org/reports/the-future-of-hydrogen.

[33] L. V. Ivanova, T. V. Bukreyeva, and O. V. Smirnova. “Kinetics and mechanism of decay of compounds containing carbonate bonds in alkaline media”. In: *Polymer Science U.S.S.R.* 25.2 (Jan. 1983), pp. 373–379. ISSN: 0032-3950. DOI: 10.1016/0032-3950(83)90214-9.

[34] Liam C Jacobson, Xiaoming Ren, and Valeria Molinero. “Assessing the Effects of Crowding, Pore Size, and Interactions on Electro-Osmotic Drag Coefficients”. In: *The Journal of Physical Chemistry C* 118.4 (Jan. 2014), pp. 2093–2103. ISSN: 1932-7447. DOI: 10.1021/jp410910r. URL: https://doi.org/10.1021/jp410910r.

[35] Dohyung Jang, Hyun Seok Cho, and Sanggyu Kang. “Numerical modeling and analysis of the effect of pressure on the performance of an alkaline water electrolysis system”. In: *Applied Energy* 287 (Apr. 2021), p. 116554. ISSN: 03062619. DOI: 10.1016/j.apenergy.2021.116554.

[36] M. B.I. Janjua and R. L. Le Roy. “Electrocatalyst performance in industrial water electrolysers”. In: *International Journal of Hydrogen Energy* 10.1 (Jan. 1985), pp. 11–19. ISSN: 03603199. DOI: 10.1016/0360-3199(85)90130-2.

[37] H. Janssen et al. “Safety-related studies on hydrogen production in high-pressure electrolysers”. In: *International Journal of Hydrogen Energy* 29.7 (July 2004), pp. 759–770. ISSN: 03603199. DOI: 10.1016/j.ijhydene.2003.08.014.

[38] Wenbo Ju et al. “Lab-Scale Alkaline Water Electrolyzer for Bridging Material Fundamentals with Realistic Operation”. In: *ACS Sustainable Chemistry & Engineering* 6.4 (Apr. 2018), pp. 4829–4837. ISSN: 2168-0485. DOI: 10.1021/acssuschemeng.7b04173. URL: https://pubs.acs.org/doi/10.1021/acssuschemeng.7b04173.

[39] Tom Kleist. “Optimization of internal geometry and electrode surface area of a high pressure electrolyser”. PhD thesis. Delft: Delft University of Technology, 2021.

[40] Daniel H. König et al. “Techno-economic study of the storage of fluctuating renewable energy in liquid hydrocarbons”. In: *Fuel* 159 (Nov. 2015), pp. 289–297. ISSN: 00162361. DOI: 10.1016/j.fuel.2015.06.085.

[41] Mikkel Rykær Kraglund et al. “Ion-solvating membranes as a new approach towards high rate alkaline electrolyzers”. In: *Energy & Environmental Science* 12.11 (2019). ISSN: 1754-5692. DOI: 10.1039/C9EE00832B.

[42] Mikkel Rykær Kraglund et al. “Zero-Gap Alkaline Water Electrolysis Using Ion-Solvating Polymer Electrolyte Membranes at Reduced KOH Concentrations”. In: *Journal of The Electrochemical Society* 163.11 (2016), F3125–F3131. DOI: 10.1149/2.0161611jes. URL: https://doi.org/10.1149/2.0161611jes.

[43] Jan van Kranendonk. *Personal communication and consultation*. Delft, 2021.

[44] W. Kreuter and H. Hofmann. “Electrolysis: the important energy transformer in a world of sustainable energy”. In: *International Journal of Hydrogen Energy* 23.8 (Aug. 1998), pp. 661–666. ISSN: 03603199. DOI: 10.1016/S0360-3199(97)00109-2.

[45] Claude Lamy and Pierre Millet. *A critical review on the definitions used to calculate the energy efficiency coefficients of water electrolysis cells working under near ambient temperature conditions*. Jan. 2020. DOI: 10.1016/j.jpowsour.2019.227350.

[46] Seunghwa Lee et al. “Alkaline CO2 Electrolysis toward Selective and Continuous HCOO– Production over SnO2 Nanocatalysts”. In: *The Journal of Physical Chemistry C* 119.9 (Mar. 2015), pp. 4884–4890. ISSN: 1932-7447. DOI: 10.1021/jp512436w. URL: https://doi.org/10.1021/jp512436w.

[47] R. L. LeRoy. “Industrial water electrolysis: Present and future”. In: *International Journal of Hydrogen Energy* 8.6 (Jan. 1983), pp. 401–417. ISSN: 03603199. DOI: 10.1016/0360-3199(83)90162-3.

[48] Lurgi Schnell-information. *Wasserstoff aus Wasser*. Tech. rep. Frankfurt: Lurgi Apparate-Technik GmbH, Jan. 1972.

[49] A. Manabe et al. “Basic study of alkaline water electrolysis”. In: *Electrochimica Acta* 100 (June 2013), pp. 249–256. ISSN: 00134686. DOI: 10.1016/j.electacta.2012.12.105. URL: https://linkinghub.elsevier.com/retrieve/pii/S0013468612020798.

[50] Hisayoshi Matsushima, Daisuke Kiuchi, and Yasuhiro Fukunaka. “Measurement of dissolved hydrogen supersaturation during water electrolysis in a magnetic field”. In: *Electrochimica Acta* 54.24 (Oct. 2009), pp. 5858–5862. ISSN: 00134686. DOI: 10.1016/j.electacta.2009.05.044.

[51] McPhy. *Produce your hydrogen on - site, on demand, according to your specifications*. 2020.

[52] Anthony F. Mills and Anthony F. Mills. “Convection Fundamentals and Correlations”. In: *Heat and Mass Transfer*. 2nd ed. Peasrson Education Limited, 2018. Chap. 4, pp. 243–370. DOI: 10.4324/9780203752173-4.

[53] Bart Mulder. “Characterization of high pressure alkaline electrolyser: Product gas purity”. PhD thesis. Delft: Delft University of Technology, 2021.

[54] N. Nagai et al. “Existence of optimum space between electrodes on hydrogen production by water electrolysis”. In: *International Journal of Hydrogen Energy* 28.1 (Jan. 2003), pp. 35–41. ISSN: 03603199. DOI: 10.1016/S0360-3199(02)00027-7.

[55] M.M.N. Nauta. “Removal of residual CO2 from feed water to increase the lifetime of KOH electrolyte”. PhD thesis. Delft University of Technology.

[56] NEL. *The World ’ s Most Efficient and Reliable Electrolysers*. 2019.

[57] Nicholson, Carlisle, and Cruickshank. “IV. Experiments in galvanic electricity”. In: *The Philosophical Magazine* 7.28 (Sept. 1800). ISSN: 1941-5796. DOI: 10.1080/14786440008562593. URL: https://www.universiteitleiden.nl/nieuws/2013/03/schonere-brandstof-dichterbij-dankzij-ontdekking-leidse-chemici.

[58] Alka Pareek et al. “Insights into renewable hydrogen energy: Recent advances and prospects”. In: *Materials Science for Energy Technologies* 3 (Jan. 2020), pp. 319–327. ISSN: 25892991. DOI: 10.1016/j.mset.2019.12.002.

[59] Robert Phillips and Charles W. Dunnill. “Zero gap alkaline electrolysis cell design for renewable energy storage as hydrogen gas”. In: *RSC Adv.* 6.102 (2016), pp. 100643–100651. DOI: 10.1039/C6RA22242K. URL: http://dx.doi.org/10.1039/C6RA22242K.

[60] Robert Phillips et al. “Minimising the ohmic resistance of an alkaline electrolysis cell through effective cell design”. In: *International Journal of Hydrogen Energy* 42.38 (Sept. 2017), pp. 23986–23994. ISSN: 03603199. DOI: 10.1016/j.ijhydene.2017.07.184. URL: http://dx.doi.org/10.1016/j.ijhydene.2017.07.184%20https://linkinghub.elsevier.com/retrieve/pii/S0360319917330203.

[61] Su-Il Pyun and Sung-Mo Moon. “Corrosion mechanism of pure aluminium in aqueous alkaline solution”. In: *Journal of Solid State Electrochemistry* 4.5 (2000), pp. 267–272.

[62] Mamoon Rashid et al. “Hydrogen Production by Water Electrolysis: A Review of Alkaline Water Electrolysis, PEM Water Electrolysis and High Temperature Water Electrolysis”. In: *International Journal of Engineering and Advanced Technology* ISSN (Apr. 2015), pp. 2249–8958.

[63] Hannah Ritchie and BP. *Statistical Review of World Energy*. 2020. URL: https://ourworldindata.org/energy-mix.

[64] William N. Rom and Kent E. Pinkerton. “Introduction: Consequences of Global Warming to Planetary and Human Health”. In: *Climate Change and Global Public Health*. Ed. by Kent E Pinkerton and William N Rom. Cham: Springer International Publishing, 2021, pp. 1–33. ISBN: 978-3-030-54746-2. DOI: 10.1007/978-3-030-54746-2{_}1. URL: https://doi.org/10.1007/978-3-030-54746-2_1.

[65] H E G Rommal and P J Moran. “Time-Dependent Energy Efficiency Losses at Nickel Cathodes in Alkaline Water Electrolysis Systems”. In: *Journal of The Electrochemical Society* 132.2 (Feb. 1985), pp. 325–329. DOI: 10.1149/1.2113831. URL: https://doi.org/10.1149/1.2113831.

[66] Mark F Ruth, Ahmad T Mayyas, and Margaret K Mann. *Manufacturing competitiveness analysis for PEM and alkaline water electrolysis systems*. Tech. rep. National Renewable Energy Lab.(NREL), Golden, CO (United States), 2019.

[67] Hiroyuki Sato and Xing L. Yan. “Study of an HTGR and renewable energy hybrid system for grid stability”. In: *Nuclear Engineering and Design* 343 (Mar. 2019), pp. 178–186. ISSN: 00295493. DOI: 10.1016/j.nucengdes.2019.01.010.

[68] Maximilian Schalenbach, Olga Kasian, and Karl J.J. Mayrhofer. “An alkaline water electrolyzer with nickel electrodes enables efficient high current density operation”. In: *International Journal of Hydrogen Energy* 43.27 (July 2018), pp. 11932–11938. ISSN: 03603199. DOI: 10.1016/j.ijhydene.2018.04.219. URL: https://linkinghub.elsevier.com/retrieve/pii/S036031991831440X.

[69] Maximilian Schalenbach, Wiebke Lueke, and Detlef Stolten. “Hydrogen Diffusivity and Electrolyte Permeability of the Zirfon PERL Separator for Alkaline Water Electrolysis”. In: *Journal of The Electrochemical Society* 163.14 (2016), F1480–F1488. ISSN: 0013-4651. DOI: 10.1149/2.1251613jes.

[70] Maximilian Schalenbach et al. “Acidic or Alkaline? Towards a New Perspective on the Efficiency of Water Electrolysis”. In: *Journal of The Electrochemical Society* 163.11 (2016), F3197–F3208. ISSN: 0013-4651. DOI: 10.1149/2.0271611jes.

[71] Jonathan Schillings, Olivier Doche, and Jonathan Deseure. “Modeling of electrochemically generated bubbly flow under buoyancy-driven and forced convection”. In: *International Journal of Heat and Mass Transfer* 85 (June 2015), pp. 292–299. ISSN: 0017-9310. DOI: 10.1016/J.IJHEATMASSTRANSFER.2015.01.121.

[72] *Schonere brandstof dichterbij dankzij ontdekking Leidse chemici*. Leiden, Apr. 2013. URL: https://www.universiteitleiden.nl/nieuws/2013/03/schonere-brandstof-dichterbij-dankzij-ontdekking-leidse-chemici.

[73] Volkmar Schröder et al. “Explosion limits of hydrogen/oxygen mixtures at initial pressures up to 200 bar”. In: *Chemical Engineering & Technology: Industrial Chemistry-Plant Equipment-Process Engineering-Biotechnology* 27.8 (2004), pp. 847–851. URL: https://onlinelibrary-wiley-com.tudelft.idm.oclc.org/doi/epdf/10.1002/ceat.200403174.

[74] C. A. Schug. “Operational characteristics of high-pressure, high-efficiency water-hydrogen-electrolysis”. In: *International Journal of Hydrogen Energy* 23.12 (Dec. 1998), pp. 1113–1120. ISSN: 03603199. DOI: 10.1016/S0360-3199(97)00139-0.

[75] Marc-Alexander Schwarze. “Controlled removal of trace o2 in an h2 environment of a smallscale electrolyser”. PhD thesis. Delft: Delft University of Technology, 2020. URL: http://repository.tudelft.nl/.

[76] Tatsuya Shinagawa, Angel T Garcia-Esparza, and Kazuhiro Takanabe. “Insight on Tafel slopes from a microkinetic analysis of aqueous electrocatalysis for energy conversion”. In: *Scientific Reports* 5.1 (2015), p. 13801. ISSN: 2045-2322. DOI: 10.1038/srep13801. URL: https://doi.org/10.1038/srep13801.

[77] HAM Snelders. “The Amsterdam experiment on the analysis and synthesis of water (1789)”. In: *Ambix* 26 (1979), pp. 116–133.

[78] D M Soares, O Teschke, and I Torriani. “Hydride Effect on the Kinetics of the Hydrogen Evolution Reaction on Nickel Cathodes in Alkaline Media”. In: *Journal of The Electrochemical Society* 139.1 (Jan. 1992), pp. 98–105. DOI: 10.1149/1.2069207. URL: https://doi.org/10.1149/1.2069207.

[79] Ramazan Solmaz et al. “Preparation and characterization of Pd-modified Raney-type NiZn coatings and their application for alkaline water electrolysis”. In: *International Journal of Hydrogen Energy* 42.4 (Jan. 2017), pp. 2464–2475. ISSN: 03603199. DOI: 10.1016/j.ijhydene.2016.07.221.

[80] Robert B. Stone and Kristin L. Wood. “Development of a functional basis for design”. In: *Journal of Mechanical Design, Transactions of the ASME* 122.4 (Dec. 2000), pp. 359–370. ISSN: 10500472. DOI: 10.1115/1.1289637. URL: https://asmedigitalcollection.asme.org/mechanicaldesign/article/122/4/359/476960/Development-of-a-Functional-Basis-for-Design.

[81] K. Svobodova et al. “Complexities and contradictions in the global energy transition: A re-evaluation of country-level factors and dependencies”. In: *Applied Energy* 265 (May 2020), p. 114778. ISSN: 03062619. DOI: 10.1016/j.apenergy.2020.114778.

[82] Junlei Tang et al. “Electrodeposited Pd-Ni-Mo film as a cathode material for hydrogen evolution reaction”. In: *Electrochimica Acta* 174 (July 2015), pp. 1041–1049. ISSN: 00134686. DOI: 10.1016/j.electacta.2015.06.134.

[83] Min J Tham, Robert Dixon Walker Jr, and Keith E Gubbins. “Diffusion of oxygen and hydrogen in aqueous potassium hydroxide solutions”. In: *The Journal of Physical Chemistry* 74.8 (1970), pp. 1747–1751.

[84] D. Thomas. *State of play and developments of power-to-hydrogen technologies*. 2019. URL: https://etipwind.eu/wp-content/uploads/A2-Hydrogenics_v2.pdf.

[85] ThyssenKrupp. *Large-scale water electrolysis for green hydrogen production*. 2020.

[86] P. Trinke et al. “Hydrogen Crossover in PEM and Alkaline Water Electrolysis: Mechanisms, Direct Comparison and Mitigation Strategies”. In: *Journal of The Electrochemical Society* 165.7 (May 2018), F502–F513. ISSN: 0013-4651. DOI: 10.1149/2.0541807jes. URL: https://iopscience.iop.org/article/10.1149/2.0541807jes.

[87] Thijs Van de Graaf et al. “The new oil? The geopolitics and international governance of hydrogen”. In: *Energy Research and Social Science* 70 (Dec. 2020), p. 101667. ISSN: 22146296. DOI: 10.1016/j.erss.2020.101667.

[88] John R Varcoe et al. “Anion-exchange membranes in electrochemical energy systems”. In: *Energy Environ. Sci.* 7.10 (2014), pp. 3135–3191. DOI: 10.1039/C4EE01303D. URL: http://dx.doi.org/10.1039/C4EE01303D.

[89] Verantis Environmental Solutions Group. *Cleanable High Efficiency Aerosol Filtration Systems (CHEAF)*. URL: https://www.verantis.com/products/aerosol-removal-systems/cleanable-high-efficiency-aerosol-filtration-systems-cheaf.

[90] Ph Vermeiren, W. Adriansens, and R. Leysen. “Zirfon®: A new separator for Ni-H2 batteries and alkaline fuel cells”. In: *International Journal of Hydrogen Energy* 21.8 (Aug. 1996), pp. 679–684. ISSN: 03603199. DOI: 10.1016/0360-3199(95)00132-8.

[91] H. Vogt. “The actual current density of gas-evolving electrodes - Notes on the bubble coverage”. In: *Electrochimica Acta* 78 (Sept. 2012), pp. 183–187. ISSN: 00134686. DOI: 10.1016/j.electacta.2012.05.124.

[92] H. Vogt and R. J. Balzer. “The bubble coverage of gas-evolving electrodes in stagnant electrolytes”. In: *Electrochimica Acta* 50.10 (Mar. 2005), pp. 2073–2079. ISSN: 00134686. DOI: 10.1016/j.electacta.2004.09.025.

[93] P.S.M. Vroegindeweij. “Modelling, Experimental Validation and Characterization of a novel small scale Methanol Synthesis Reactor”. PhD thesis. Technische Universiteit Delft, 2020, p. 142.

[94] Mingyong Wang et al. *The intensification technologies to water electrolysis for hydrogen production - A review*. Jan. 2014. DOI: 10.1016/j.rser.2013.08.090.

[95] T Weier and S Landgraf. “THE EUROPEAN PHYSICAL JOURNAL SPECIAL TOPICS The two-phase flow at gas-evolving electrodes: Bubble-driven and Lorentz-force-driven convection”. In: *Eur. Phys. J. Special Topics* 220 (2013), pp. 313–322. DOI: 10.1140/epjst/e2013-01816-1.

[96] Herbert Wittel et al. *Roloff/Matek*.

[97] Xiaohe Yan et al. “Power to gas: addressing renewable curtailment by converting to hydrogen”. In: *Frontiers in Energy* 12.4 (Dec. 2018), pp. 560–568. ISSN: 20951698. DOI: 10.1007/s11708-018-0588-5.

[98] Guiyan Zang et al. “Performance and cost analysis of liquid fuel production from H2and CO2based on the Fischer-Tropsch process”. In: *Journal of CO2 Utilization* 46 (Apr. 2021), p. 101459. ISSN: 22129820. DOI: 10.1016/j.jcou.2021.101459.

[99] Kai Zeng and Dongke Zhang. “Recent progress in alkaline water electrolysis for hydrogen production and applications”. In: *Progress in Energy and Combustion ScienceZeng, K., & Zhang, D. (2010). Recent progress in alkaline water electrolysis for hydrogen production and applications. Progress in Energy and Combustion Science, 36(3), 307–326. https://doi.org/https://doi.org/10.1* 36.3 (2010), pp. 307–326. ISSN: 0360-1285. DOI: https://doi.org/10.1016/j.pecs.2009.11.002. URL: http://www.sciencedirect.com/science/article/pii/S0360128509000598.

[100] Jinsuo Zhang, Marc Klasky, and Bruce C. Letellier. “The aluminum chemistry and corrosion in alkaline solutions”. In: *Journal of Nuclear Materials* 384.2 (Feb. 2009), pp. 175–189. ISSN: 0022-3115. DOI: 10.1016/J.JNUCMAT.2008.11.009.

[101] Avital Zhegur et al. “Changes of Anion Exchange Membrane Properties During Chemical Degradation”. In: *ACS Applied Polymer Materials* 2.2 (Feb. 2020), pp. 360–367. DOI: 10.1021/acsapm.9b00838. URL: https://doi.org/10.1021/acsapm.9b00838.